U.PORTO
FACULDADE DE CIÊNCIAS
UNIVERSIDADE DO PORTO

PhD

PhD

3.º CICLO

FCUP
ANO

U.PORTO

A Theoretical Study of H2 Diffusion and Adsorption into Carbon Nanotubes Using MonteCarlo Simulations

Marco Lerario

FC

U.PORTO
FACULDADE DE CIÊNCIAS
UNIVERSIDADE DO PORTO

A Theoretical Study of H2 Diffusion and Adsorption into Carbon Nanotubes Using MonteCarlo Simulations

Marco Lerario

Tese de Doutoramento apresentada à
Faculdade de Ciências da Universidade do Porto
Química

2017

PhD

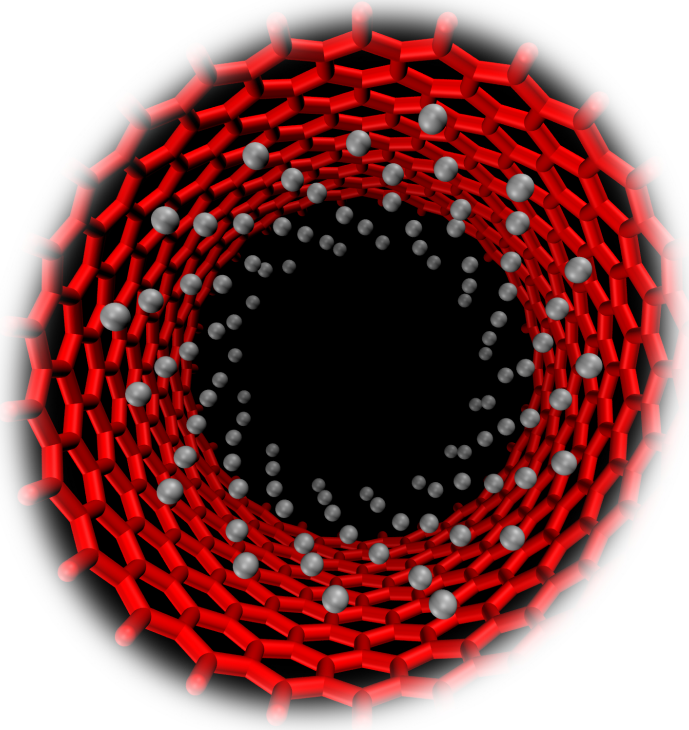

A Theoretical Study of H_2 Diffusion and Adsorption into Carbon Nanotubes Using MonteCarlo Simulations

Marco Lerario
Doutoramento em Química
Departamento de Química e Bioquímica

2017

Orientador
Alexandre Lopes de Magalhães, Professor Auxiliar, Faculdade de Ciências

Acknowledgements

As we all live intertwined, you never know how such small things as a smile, a word, or even just listening, can really make a difference an mean great things for other people. Hence, there are so many I would like to thank, and even more that I should, but I'll never be able to remember all. Let's just put in this terms, since we are actually dealing with science and statistics, consider this like a small but representative sample, part of a greater universe, where lots of people, like the ones mentioned here, continuously do their best to support each other and promote others development like their own.

I'm certainly grateful to professor Alexandre Magalhães for the patient work done together and the countless challenges we passed through. I'm glad to remember also professor Maria João Ramos for the brilliant conversation where the first ideas of the new algorithm were born.

I thank Elizabeth, Francisca, Kris and Iwona for the gorgeous moments we shared, I'm so grateful for the events that brought us together and I will always feel honoured to be your friend. Henrique, Juliana and Carla, thank you for keeping room 3.26 a warm place to work, meaning that good company matters more than temperature! I thank you Ana for your exceptional support, your kind listening and bright solutions. I would like to thank all my colleagues, in particular Eduardo, Rui and Diana, for your solicitous help and fruitful conversations during all these years.

A special thanks goes to my father and brother, as well as my uncle and aunt and my dearest cousins: even if time and distance divide us, I know you are always at my side (who more lucky than I, and who more supported?). I also thank you Sara, for your kind attention, for your laughs, for your delicious ideas, which offered me some wonderful moments.

I also want to thank Carlos, Luis, Zé Manel, Zé Alberto and all my brothers, for the patience and comprehension as well as your support in the last few months. I cannot forget to thank my "personal trainers" Kika and Virgínia, without your faith and your

encouragement I would have never gone through all this; in the end, my only fear was that I could disappoint you. Thank you Carla, Francisco, Tiago and Sofia for the precious help that I didn't even dare to ask; your constant presence made me feel like nothing was impossible! To Margarida, Andreia, Daniela, Zé Pedro, Catarina, and all the friends of the SMC, thank you for your advice, your words, prayers, and specially for the cheerful and refreshing moments we lived in Viseu.

Finally, I thank FCT - Fundação para a Ciência e Tecnologia for the grant SFRH / BD / 90502 / 2012, as well as REQUIMTE - Rede de Química e Tecnologia which offered me the necessary conditions to develop this work.

Abstract

The interest of this work on Carbon Nano Tubes lies mainly in their shape (cylindrical symmetrical, combined with extreme length) which keeps intertwined opposite characteristics like symmetry and randomness. The way they aggregate in real samples, with the formation of bundles, as well as the insurgence of defects creates an extreme variety of pores and different environments which can behave very differently. The affinity for hydrogen, together with its small size, make it the perfect probe molecule for investigating such structures.

The studies found in literature, which are mainly focused on maximising adsorption, *e.g.* for automotive application, not always produce reproduccible results or, at least, their range is extremely wide. This happens not only on the experimental side, but also in theoretical works, thus proving that this subject is very far from being exhausted and that there are still many aspects to be enlightened.

This investigation therefore wants to explore alternative paths, including and combining new effects; the Monte Carlo method offers both the versatility and the capability to adapt to variable environments. We approach the subject of hydrogen interaction in several ways. From a topological point of view we construct potential energy surfaces of the different pores and environments: potential data are gathered from literature and their effect is also object of investigation. Through GC simulations, we found adsorption being very sensitive to such parameters, and explained how the pore size influence the uptake / storage mechanism. The other interesting aspect was accessibility, which has been studied by means of Kinetic Monte Carlo in simulations of diffusion dynamics. Finally, the aim of phase transition studies was to explore the existence of alternative ordered conformations, related to the symmetry of the system.

All the code used in this work was written on purpose, with the goal of, in the future, being linked together so that all the aspects can be investigated at once.

Resumo

O interesse deste trabalho sobre os Nano Tubos de Carbono reside principalmente na sua forma (simétria cilíndrica, combinada com comprimento extremo) que mantém características opostas e entrelaçadas como simetria e aleatoriedade. A forma como se agregam nas amostras reais, com a formação de feixes, bem como a existência de defeitos, cria uma extrema variedade de poros e ambientes diferentes que demonstram comportamentos muito diferentes. A afinidade pelo hidrogénio, juntamente com seu pequeno tamanho, tornam esta molécula uma sonda perfeita para investigar tais estruturas.

Estudos anteriores, destinados principalmente a maximizar a adsorção, *e.g.* para aplicação na indústria automóvel, nem sempre produzem resultados reprodutíveis ou, pelo menos, a sua dispersão é extremamente elevada. Isto acontece não só em trabalho experimental, mas também em trabalho teórico demonstrando que este assunto está muito longe de ser esgotado e que existe um grande número de aspetos que necessitam ser clarificados.

A presente investigação portanto pretende explorar caminhos alternativos que incluem e combinam novos efeitos. O método Monte Carlo oferece tanto a versatilidade como a capacidade de adaptação a ambientes variáveis. Abordamos o assunto da interação do hidrogénio de várias formas. Do ponto de vista topológico, construímos superfícies de energia potencial dos diferentes poros e ambientes: dados potenciais são coletados da literatura e seu efeito é, também, objeto de investigação. Através de simulações do ensemble grande canónico concluimos que a adsorção é muito sensível a esses parâmetros e explicamos como o tamnho dos poros influencia o mecanismo de captação/armazenamento. O outro aspecto interessante foi a acessibilidade, que tem sido estudada por meio de Monte Carlo Cinético em simulações de dinâmica de difusão. Finalmente, os estudos de transição de fase pretendem explorar a existência de conformações ordenadas alternativas, relacionadas com a simetria do sistema.

Todo o código utilizado neste trabalho foi escrito com o objetivo de, no futuro, poder ser interligado para que todos os aspectos possam ser investigados simultaneamente.

Contents

List of Figures

List of Tables

List of Abbreviations

ASH	Amount of Stored Hydrogen
AVB	Aggregation Volume Bias
BET	Brunauer–Emmett–Teller
CB	Configurational Bias
CNF	Carbon Nano Fibers
CNT	Carbon nanotube
CVD	Chemical Vapour Deposition
D_s	Self-diffusion coefficient
DFT	Density Functional Theory
DOS	Density of States
DWNT	Double-walled carbon nanotube
FH	Feynman Hibbs
GC	Grand Canonical
GCMC	Grand Canonical Monte Carlo
GE	Gibbs Ensemble
GEMC	Gibbs Ensemble Monte Carlo
KMC	Kinetic Monte Carlo
LJ	Lennard-Jones
MC	Monte Carlo
MCCCS	Monte Carlo for Complex Chemical Systems
MD	Molecular Dynamics
MWNT	Multi-walled Nano Tube
PEP	Potential Energy Profile
PES	Potential Energy Surface
PI	Path Integral
PSD	Pore Size Distribution
QENS	Quasielastic Neutron Scattering
SWNT	Single-walled carbon nanotube

TEM	Transmission Electron Microscopy
TM	Transition Matrix
TMMC	Transition Matrix Monte Carlo
TPD	Temperature Programmed Desorption

Chapter 1

Introduction

Nanotubes were first synthesized in 1991 and, since then, they have been the focus of multiple studies due to their great potential in many fields [46, 21]. They have unique and specific characteristics, such as their nanometric scale size, hollow and cylindrical shape [41]. These characteristics make them potential materials to be used in catalysis [93], separation and purification processes [49, 11], and also in gas storage and transport[22, 116, 55]. In particular, the storage and transport of fuels like hydrogen and methane - which are renewable energy sources - inside single-walled carbon nanotubes (SWNTs) is of prominent importance because of the increasing necessity to find cleaner alternatives to fossil fuels [37]. In fact, this is a subject of current investigation in the area of automotive applications [21]. There are already some studies about the two main properties that influence the storage and mobility of gases inside SWNTs: their adsorption capacity[16, 39] and the diffusion of gases inside them [9, 73, 72]. However, a consensus has not been established yet about the influence of these parameters on the autonomy and efficiency of those physical processes. Therefore, it is important to understand and clarify the structure-property relationships since it is established that the diffusion depends on the structural parameters of the pores[2].

In this thesis the topic is approached by three points of view: one, strictly quantitative, involve Monte Carlo (MC) simulations of the loading limit capacity of some Carbon Nanotubes (CNTs), different for size and geometry. A more qualitative analysis aims to investigate the accessibility of deeper zones of CNT structures through kinetic Monte Carlo (KMC) simulations. Finally a more specific study focus on hydrogen molecules and their aggregations states, when confined into carbon nano structures.

1.1 Carbon Nano Tubes

CNTs can be visualized as a single graphene sheet wrapped into a cylindrical tube; according on how many sheets are concentrically wrapped, they can be Single-Walled Nano Tubes (SWNT), Double-Walled Nano Tubes (DWNT) or Multi-Walled Nano Tubes (MWNT).

Moreover, there is not just one way to wrap the sheet, but a virtually infinite variety of CNTs is available.

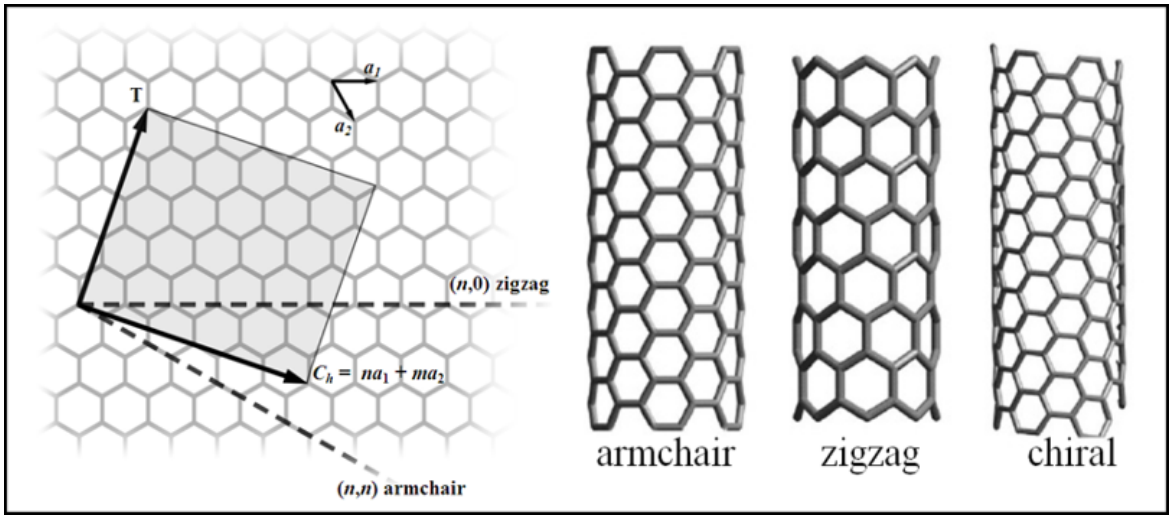

Figure 1.1: *Wrapping of CNTs.*

A graphene planar unit cell is defined by two vectors $\overline{a}_1$ and $\overline{a}_2$ (see figure 1.1): any displacement along the plane of a combination of these two vector $n\overline{a}_1 + m\overline{a}_2$ with $n, m \in N$ positive integers, generates a point which is indistinguishable from the previous one. In order to ideally wrap the plane, it is of course necessary to overlap indistinguishable points, so that the coefficients n and m are sufficient to uniquely identify a wrapping. The only exception is the *chiral* wrapping, which happens for $m \neq n \neq 0$, because it produces a nanotube not superimposable to its mirror image. Therefore any chiral CNT can have two possible orientations. Other ways to wrap generates respectively *zig-zag* CNTs ($m = 0$) or *armchair* ($m = n$).

From the geometric point of view, since they are made of hexagons wrapped around, CNT section (perpendicular to the wrapping axis T) is more like a polygon than a circle. A common way to define CNT's size, nevertheless, is to calculate the perimeter of the CNT using the index n and m. Knowing in fact that $|a_1| = |a_2| = l_b\sqrt{3}$, where l_b is the bond length of the carbon framework, it is possible to deduce the perimeter.

Now, assuming that value as it were a circle, it is possible to estimate a radius

$$R = \frac{l_b\sqrt{3}}{2\pi}\sqrt{n^2 + nm + m^2}\,. \tag{1.1}$$

Finally, for the sake of completeness, it should be said that the periodicity along the Z axis varies a lot according to the CNT type. In fact, a *zig-zag* $(n, 0)$ type CNT is periodic after just $2n$ atom, *i.e.* the next atom in the Z direction is indistinguishable from the first. In the *armchair* type we have a similar behavior but after 4 distinguishable atoms. The *chiral* case instead, is much more complicated. For example, in figure 1.1 (left inset) is represented a *chiral* wrapping with $n = 4$ and $m = 2$: it is clear that the axis T only founds an equivalent atom at $4\overline{a}_1 - 5\overline{a}_2$, so the total unit cell comprises 60 atoms.

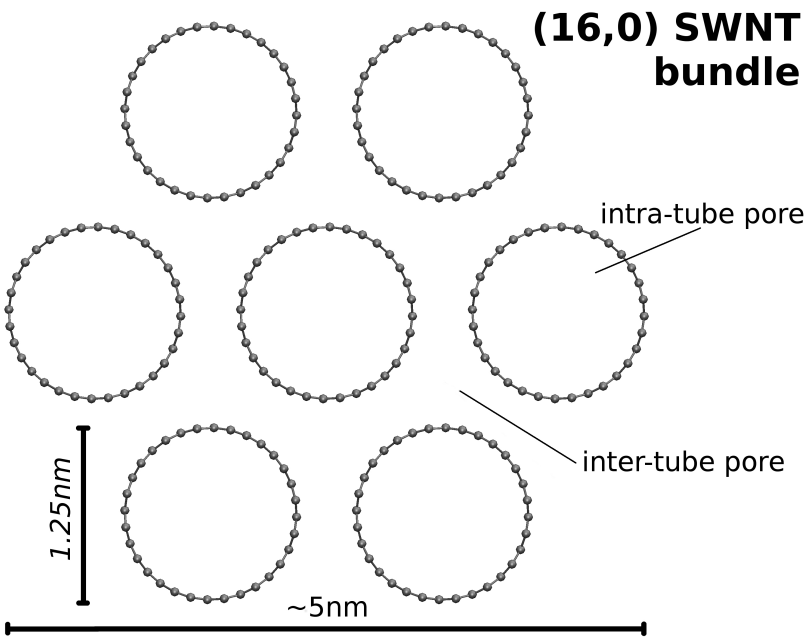

Figure 1.2: *SWNTs forming bundles.*

Nanotubes tends to aggregate forming bundles in a triangular lattice. Figure 1.2 represents a typical structure which enlighten several different environments. Very hollow pores are situated in the inter-tube spacing. In the case of $(16, 0)$ SWNT bundles, such pores' size is about 0.2-0.3nm, just enough to host a small hydrogen molecule[94]. On the other hand, according to equation 1.1, their diameter should be 1.25nm, as shown in the picture, so that the available pore size for H_2 is about 0.7nm. The accessibility of these pores in real sample is not obvious, due to the length of CNTs and also to the possibility of their ends being closed by a fullerene-like surface.

On the outside of the bundle two different surfaces are also identifiable: the convex one around the external CNTs and the groove between two adjacent.

Bundle size can grow up to 20nm as more SWNT are joined together. The extremely high aspect ratio ($Length/diameter \sim 1000$) supports the simulation of CNT in periodic limit conditions along their axis (*i.e.* infinitely long CNTs).

1.2 State of the art

1.2.1 Experimental data

Since their discovery by Iijima *et al.* [47] CNTs have been investigated as a potential way for hydrogen storage due to their high surface area and the innate inclination of carbon to adsorb gas molecules.

Dillon *et al.* [22] were the first to publish experimental data on hydrogen adsorption in nano tubes. They developed Temperature programmed Desorption (TPD) techniques in order to exactly measure, by means of a mass spectrometer, the hydrogen amount desorbed by the sample during a heating run. Their sample was firstly heated under vacuum, then exposed to hydrogen at 300 $Torr$ ($\sim 40Pa$) and finally cooled to $133K$. The chamber was then evacuated with concurrent cooling of the sample to $90K$. The TPD then consists in plotting the hydrogen mass signal while continuously heating up to $450K$. The authors reported a gravimetric storage density of 5-10%wt at room temperature. These values however, are extrapolated from measure of a soot sample containing $0,1$-$0,2\%$ of as-prepared SWNT. Liu C. and Cheng H.-M. in a recent review [61] underlined that, although TPD could possibly have some discrepancies with respect to volumetric or gravimetric analysis because of the small time between the removal of the pressure used for charging the sample and the start of the measures, its advantage is that it detects precisely the presence of hydrogen.

Based on these results, Ye *et al.* [114] measured hydrogen adsorption on SWNT which they had prepared and purified. To cut the SWNTs and disrupt the rope structure, nanotubes were sonicated for $10h$ in dimethyl formamide until the sample was completely suspended in the solvent and finally they were extracted by means of vacuum filtration. Volumetric measures, performed with a Sieverts apparatus and after $10h$ degassing at 220°C, are reported only for $80K$: $8,2\%wt$ under $12MPa$. The authors found adsorption values, compared to Saran carbon, being proportional to the

BET surface ratio ($285m^2g^{-1}$ and $1600m^2g^{-1}$ respectively). Transmission Electron Microscopy (TEM) images show $1,3$nm diameter SWNT packed in triangular lattice bundles of 6-12nm diameter. From these information the authors argue that only external surface is measured by BET method with nitrogen gas. Data show that Saran carbon have higher capacity at pressures below $30bar$ probably due to the higher accessibility of adsorption sites that saturate rapidly, while SWNT storage increase linearly with increasing pressure. Sonication appeared to increase CNTs' adsorption by a factor of two at pressures below $60bar$. This behaviour has been attributed to the reduction of cohesive energy of the rope structure by means of defect generation.

When SWNT aggregates form bundles it is possible to identify 2 different kinds of pores. One is the inner cavity of the CNT (usually not available in as-synthesized CNT which are closed by semi-sphere shaped fullerene molecules), the other is the interstitial pore inter CNT. DWNT and MWNT have also one or more inter-layer pores respectively. Surface of the bundles is also capable of adsorption: the curved external surface and the groove between two adjacent CNTs. Moreover CNT bundles aggregate creating a broad distribution of meso pores. Such diversity, even in adsorption energies, makes difficult to match the measure of the available surface area with the predicted data. Large diameter SWNT (mean value $= 1,85 \pm 0,05$nm), synthesized by a semi-continuous hydrogen arc discharge method, were tested for hydrogen adsorption by Liu C. *et al.* [62]. Their measures consist in monitoring the hydrogen pressure (10-12MPa) in a constant-volume cell containing the sample: the difference between the initial and equilibrium values corresponds to the adsorbed amount. The authors compared as-prepared SWNT adsorption, a sample treated with hydrochloric acid (37%) for 48h and another one that, after having received this HCl treatment, was also heated under vacuum at $773K$ for 2h. The HCl soak should remove the residual catalysts while the heating should evaporate organic compounds formed on the surface. The latter cause a relevant increase of adsorption: $2\%wt$, $2,5\%wt$ and $4,2\%wt$ are respectively the hydrogen uptake of the three samples which had a purity of 50-60%. It is also reported that almost 80% of hydrogen was adsorbed reversibly, while for desorbing the rest heating at 473K was necessary. However Darkrim *et al.*[20] argued that two thermal effects should have been taken into account: the gas compression up to the target filling pressure and the gas adsorption during this filling. Both could cause an overestimate of the hydrogen uptake.

It is undoubted that the morphological properties of the adsorbent exert relevant influence on capacity. Still, we can only speculate about their effect. Tarasov *et al.* [106] carried out sorption measures on SWNT synthesized by the arc discharge method

using respectively Co and Ni powder or YNi_2 powder as catalyst. They managed to purify samples up to 75% and characterised them by TEM. SWNT prepared with Co and Ni powder seemed to be slightly narrower ($1,2$nm diameter versus $1,4$nm). The authors reported a $2,4\%wt$ sorption capacity at $25bar$ and $77K$ in conditions of no saturation: application of $35bar$ nearly doubles such amount. Larger nanotubes have shown 15% higher capacity, it could be nevertheless due to the presence of hydride forming metal, residue of the catalyst. TPD measures have also shown that about 2/3 of the amount is stored in reversible condition and thus desorbed at low temperature while the rest only desorbs at 470°C as it should be for chemisorbed hydrogen. At room temperatures, storage capacities dramatically fall: $0,2$-$0,4\%wt$ under 10-30bar of H_2 pressure. Besides, at pressure below $25bar$, SWNT show even less adsorption capacity than AX21 activated carbon. This trend is then inverted at cryogenic temperature and high pressure: the authors argued it could be due to an increase in inter-tube distance caused by pressure as it was earlier suggested by Ye *et al.* [114].

Bacsa *et al.* [3] studied the effect of purification on CNT synthesized by catalytic chemical vapour deposition (CVD). The purification methods they use (oxidative acid treatments or by heating in inert gas) decrease the hydrogen storage. They also argued that decreasing the residual catalyst content does not necessarily lead to an increase in Amount of Stored Hydrogen (ASH) and that increasing the specific surface area does not necessarily increase the hydrogen storage capacity, but other factors are probably involved. One of this could be the volume of the pores whose diameter is shorter than 3nm.

An interesting research published by Shiraishi *et al.* [94], compares adsorption data at room temperature, respectively from SWNTs and from the so called "peapods" that is C_{60} encapsulated SWNTs. The authors mean to study the adsorption mechanism at room temperature and calculate its potential in CNTs. SWNTs were synthesized by Nd:YAG laser ablation using Ni/Co catalysts. High purification yield was obtained by refluxing samples in aqueous solution of H_2O_2 for 3h, treating with HCl overnight and finally ultrasonication in aqueous $NaOH$ (pH = 10-11) for 2h. Then, part of the SWNT was used to synthesize peapods (about 85% filling rate) and finally both samples were heated under vacuum at 973K, $10^{-2}Pa$ for 1h. Assuming a Langmuir model and the calculated theoretical adsorption potential of an individual and isolated SWNT being about 0,09eV (1082K) [102], hydrogen adsorption on the outer surface and the intra-tube pores can occur only at low temperature. However comparative TPD results show that hydrogen could adsorb in the interstitial pore of nanotube bundles. SWNT bundles usually aggregate in a triangular lattice, and according to

this model, authors calculate an interstitial pore diameter of about $0,2$-$0,3$nm for the $1,4$nm diameter SWNT used in this experiment. Since calculated intra-CNT pore size is 1nm, they expected adsorption potential in the interstitial to be higher. It has been estimated by means of Kissinger's plot to be $0,21eV$: a value nevertheless small enough to prove the occurrence of physiorption. They conclude that adsorption capacity at room temperature seems to be enhanced by the presence of small pores of $0,2$-$0,3$nm. Adsorption in such small interstitial pores could explain the discrepancy between measured potential and theoretical values.

What can be argued about such kind of small pores is their low accessibility especially in structures with a high aspect ratio as nanotubes usually are. Holt *et al.* [45] have proved nevertheless that mass transport through CNTs with diameters smaller than 2nm could be faster than predicted by Knudsen model. According to Molecular Dynamics (MD) simulations, they attribute this behaviour to the smoothness of the CNT which cause the emergency of a combined flux resulting from both specular and diffusive collisions, being the Knudsen model purely diffusive and thus slower. Another significant data reported in this work is that hydrocarbons exhibit higher selectivities due to their preferential interaction with the CNT sidewalls. However the authors prepared membranes of straight nanotubes with 2-3μm thickness which result in a smaller aspect ratio than CNTs usually have. Therefore, it is not proven yet that such behavior could occur with free and longer CNTs.

More recently, much effort is being made to understand how adsorption is affected by both morphological (*e.g.* specific surface area, diameter) and chemical factors (*e.g.* purification methods). Studies of such kind have also been carried out in the past, but now they seem to explore a wider range of possibilities and not only attempting to maximize adsorption. Raman spectroscopy is often used for characterizing CNTs identified by radial breathing vibrational modes. Information about nanotube diameter distribution as well as the ratio between ordered CNT and amorphous carbon are available from spectrum analysis.

Ioannatos and Verykios synthesized SWNTs and MWNTs by CVD and characterized them by Raman spectra, Scanning Electron Microscopy and BET surface (N_2 at $77K$) [48]. Adsorption measures were then analysed in terms of hydrogen adsorbed amount on a per unit mass or per unit surface area basis. The latter is very important for comparing MWNT adsorption capacities since not all layers take part in the adsorption process. Since MWNT showed a higher capacity per unit surface area than SWNT, but lower one with respect to the unit mass, the authors argued that nitrogen, used for measuring surface, and hydrogen are not adsorbed in the same way in such

systems. They also formulate the hypothesis of the existence of specific adsorption sites. This is consistent with the results obtained at $298K$ since the measured capacity is significantly lower than the calculated value for a complete monolayer adsorption. TPD analysis have nevertheless shown that the adsorption sites on the CNTs surface are relatively uniform and that there are no sites which form very weak or very strong adsorption bonds. At $77K$ high adsorption capacities exceed the theoretical value for monolayer coverage.

Karatepe and Yuca [50] analysed three ways (HCl, HNO_3 , H_2SO_4; all $3M$) of removing the metal catalysts from the synthesized SWNT and one (30% $H_2O_2 : 3M$ HCl) which removes amorphous carbon as well, in order to investigate their possible effects. ThermoGravimetric analysis and Raman spectroscopy produced information on purity and integrity of nanotubes before and after treatment. For each sample as well as for the as-grown CNTs it was measured adsorption capacity at $77K$ and pressures up to $100bar$. Purification enhanced adsorption and shortened SWNT in all cases. This could be important because it opens the ends, making inner adsorption possible. Although the sample with the highest purity was the one treated by HNO_3, the best storage performance ($4.86\%wt$) has been achieved after purification with $H_2O_2 : HCl$, probably due to the removal of amorphous carbon.

1.2.2 Theoretical studies

Many efforts have been made in theoretical investigation to achieve the maximum storage capacity of SWNT. MC simulations according to the Grand Canonical (GC) ensemble have been widely used to reproduce experimental results and explain storage capacities of various carbon based structures (*e.g.* SWNTs, MWNTs, CNFs). In fact, GCMC simulation technique, since it is able to generate and remove molecules from the system until reaching equilibrium at a fixed chemical potential, is very suitable for adsorption studies. It can be imagined as a constant temperature and pressure system in equilibrium with an ideal infinite thermal bath which has fixed chemical potential.

After Chambers *et al.* [12] reported spectacular experimental hydrogen storage of $67\%wt$ into CNFs this kind of studies spread very quickly. Rzepka *et al.* [91] investigated by GCMC simulations the storage capacities of carbon slit pores (constituted by two graphitic layers separated by a certain distance) and CNTs as a function of layer distance and nanotube diameter respectively. Non bond interactions were handled by a 12-6 Lennard Jones (LJ) potential whose parameters for hydrogen-hydrogen were adapted from literature ($\sigma = 0,297$nm and $\mu = 33,3K$) and for hydrogen-

carbon were calculated by Lorentz-Berthelot combining rules. They concluded that, unless at low pressures, CNTs have lower storage capacity than slit pores which achieved maximum capacity of $1,3\%wt$ at $10MPa$ for an inter-layer distance of $0,7$nm. Darkrim and Levesque [19] explored adsorption storage in a wide range of temperature and pressure for different structures and geometries of CNTs. GCMC simulations take into account quantum effects through the Feynman-Hibbs (FH) perturbative approach[32] on LJ potentials. H_2–H_2 quadrupole interactions were computed apart, being negligible in the h^2 calculation. Results pointed out that, at room temperature or low pressures, more compact systems show higher adsorption efficiency. The opposite happens instead at 77K and high pressure, conditions in which two layers formation is observed and thus systems with more space available are preferred. The authors therefore reported (at $77K$ and $10MPa$) maximum adsorption of $11.24\%wt$ for SWNT of $0,22$nm diameter and $0,11$nm spaced.

MD studies reported the analysis of adsorbed hydrogen molecules in the SWNT bundles enlightening the presence of preferential adsorption sites which could be more or less available according to the geometric properties of the CNTs. At very low temperature simulations it has been also observed the formation of multiple adsorbed layers. Topological defect has been analysed as well, in order to check whether they increase or not the adsorption. DFT and ab initio calculation have also been used to investigate whether physiorption or chemisorption should be the preferred mechanism [57].

Theoretical works have also been developing many ideal systems, optimising them for maximum hydrogen uptake. Minami *et al.* [71] worked on SWNT searching for the best geometric properties in terms of size and packaging. Singh *et al.* [99] performed GCMC using carbon foams under different potentials, one from fitting experimental data and the other from *ab initio* calculations: they reported that storage parameters depend greatly on that choice. They also emphasized that at very low temperature quantum effects are significant and should be taken into account in order to make realistic predictions. Moreover, CNTs and carbon structures are able to be modified (*e.g.* doping, functionalizations) in order, for instance, to modulate adsorption energy, packing structure or size and thus find the optimal properties for high hydrogen storage. Roussel *et al.* [90] simulated Li-doping on carbon replica of zeolites and reported an increase in storage capacity.

1.3 Confined spaces investigation

The study of confined spaces starts with the question: what happens if molecules have very little space available? This can be the result of two very different situations. It can be a consequence of a crowded system or, for instance, a very small one. In both cases molecules are pushed together, but what constrains them is the element that makes the difference. In the former, molecules space is limited by interactions with other molecules (at least similar in size and mobility), whereas in the other, the interactions with the system's wall are responsible for the confinement. We can imagine such walls as bigger molecules which mobility can be neglected if compared with the smaller ones. Gas molecules into a carbon framework (such as CNTs) is a good example. For the sake of simplicity we shall call fluid and substrate respectively the small high-mobility molecules and the big ones which constrain the system.

Before even thinking about the nature of such interactions that are confining the available space, there is a characteristic that should be considered. That is symmetry. In a crowded system, *i.e.* a system overwhelmingly filled with small molecules, the forces that squeeze the available space are essentially isotropic, that is, in average, they are uniform with respect to any direction of the space. The anisotropic confinement, such as the one produced by big molecular framework, will instead imprint its own symmetry to any isotropic mean (fluid or gas) in its proximity. This effect decays with the distance so, in open or large spaces, it affects only a small or negligible fraction of the fluid. Hence, speaking about regular structures, such as graphite, CNTs or general carbon frameworks, the shape is more relevant than the exact position of a single atom. In these cases the effective interaction is then composed by two main characteristics, the symmetry and the interatomic potential. While the former is only defined by geometric parameters of both substrate and fluid, the second depends substantially on the type of atoms involved.

In conclusion the combination of the two factors, in these conditions, generates an ensemble of lots of possibilities, due to the fact that similar environments are present. At the same time, the interactions between fluid molecules are significant and could resemble the symmetry of the substrate.

1.3.1 Methodological approach

Generally speaking, the goal of an investigation is to calculate the physical properties of the system and understand how they can possibly vary, affected by one another or by an external perturbation. The starting point would be, of course, to define the equation of motion which means, in a broad sense, the differential equations of the variables which describe the system (*e.g.* the forces).

Here a substantial choice arise about which technique would be the most suitable to find a solution for all equations. A deterministic approach would involve the analytic or numeric solution of all of them. This has two main drawbacks: the first, more obvious, concerns the effort (computational or not) needed to solve them for all variables of a system with lots of degrees of freedom. In practice this limits the rigorous approach just to small systems or involve the use of very fast computers, as well as lots of computational time. Nevertheless, techniques exist where only some equations are solved and the others are approximated, in order to keep the degrees of freedom as low as possible. The second disadvantage actually apply only to numerical methods, but in these conditions analytic methods are even less feasible. It regards to the general algorithms used to seek the solutions of equations. Since the method usually proceeds stepwise from an initial guess or from some initial conditions, what can happen, if such guess is not close enough to the solution, is that the algorithm cannot find a solution in short times, or it finds the solution closest to the starting point. For instance, in a process of minimisation of energy (*i.e.* differential equation of all forces equal to zero), if the starting point is already close to a local minimum, the search algorithm is unlikely to end up at a differen and lower one. Therefore, this has to be solved through a careful choice of the initial guess as well as a multiple try procedure.

What would we be willing to sacrifice to improve such aspects? The stochastic approach substitutes the exactness of the deterministic one with a broader exploration of the possibilities. The laws of motion become probabilities and the outcome is no more a solution but a distribution. Since the word "stochastic" ($\sigma\tau o\chi\alpha\zeta o\mu\alpha\iota$) already means *to guess* or *to see*, the approach involve the generation of multiple guesses of the system, which distribute according to the laws of the system, meaning that, for instance, the forces make one outcome being more probable than another. Statistic tools can be then applied to the results gathered in this way, producing estimations of the same variables investigated by the deterministic approach. We definitely lost the certainty, because we will never be sure that the outcome is exactly the solution, but we gain lots of information about the outcome distribution. In this way it is possible to

analyse the behaviour of the system not only in one point but also in its surroundings.

As seen so far, both methods have pros and cons: the choice between them is therefore driven by the characteristics of the system under investigation. Deterministic approach would involve, for instance, MD simulations, which are widely used to study CNTs[82, 16]. MC methods are also able to proceed in the same way, but its inherent randomness makes them very suitable for stochastic simulations.

In the case of CNTs, as for graphite or carbon framework, having lots of all equivalent and indistinguishable atoms, the detail level of the deterministic approach seems unnecessary. On the other hand, since the stochastic approach is capable of moving all the degrees of freedom at the same time, we focus especially on the effect that atoms exert together. In other words we simulate the interaction fluid-substrate without having to study each atom separately.

1.3.2 Modelling the system

Carbon nano-structures have been considered very promising materials for hydrogen fuel cell applications due to their adsorption capability. Such structures exhibit a large variety of shapes, and the further possibility of modifying their geometrical properties has made them widely studied materials, in order to achieve the most efficient storage. Nevertheless, sufficiently high capacities have not yet been obtained either experimentally or theoretically and there are still many discrepancies between results produced by the two approaches[37].

Synthesised for the first time in 1991 by Iijima[47], CNTs were only proved to have reasonable adsorption properties in 1997[22]. Since then, experimental works have been trying to develop efficient synthesis as well as new purification methods in order to remove residual metallic catalysts[50]. Such proceedings however have the drawback of increasing the percentage of amorphous carbon, but are also able to open the end cap of the tubes, making the inner surface available[50]. Even the most simple SWNTs, in real samples, have a non mono-disperse dimensional distribution and furthermore they present higher levels of superstructures which generates a broad variety of pores with very different adsorption properties[61]. Characterisation techniques and theoretical models have been proposed in order to get information about the microscopic structure and the Pore Size Distribution[48][51] (PSD).

On the theoretical side, one of the big issues is the formulation of a pair potential which effectively simulates carbon hydrogen interactions[75]. Pair interactions between

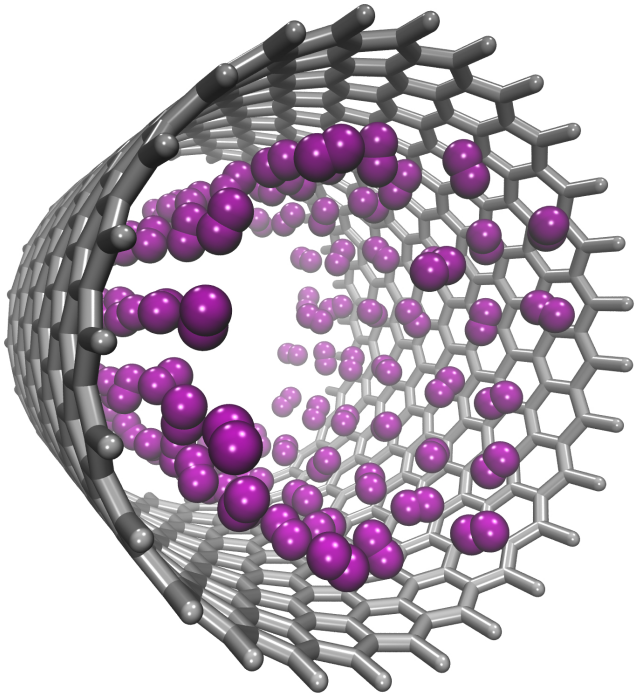

Figure 1.3: *Emergence of ordered conformations in adsorbed layers.*

identical molecules can be optimised comparing simulations with the experimental bulk properties; this is the case of hydrogen, about which well known potentials are easily found in literature[98][8]. The same principle is valid for carbon, although Nguyen *et al.*[75] suggest that CNT should exert a stronger attraction than graphite[104]. Nevertheless, Lorentz-Berthelot rules are still useful way to obtain the mixed potential parameters easily. Alternatively, theoretical calculations can try to fit experimental results, studying some highly symmetric and regular systems (*i.e.* CNT lattice or flawless graphite), providing information about the best interaction parameters[109] [34]. For some simplified systems *ab initio* calculations are also feasible[28].

Dubbeldam *et al.* managed potential parametrization by fitting inflection point of experimental adsorption isotherms inside Silicalite-1[23]. For CNT systems such approach is not straightforward because of the broad PSD and the lack of structural detail of real samples.

Due to the microscopic variety, it is difficult to address proper cause-effect relations to experimental studies. This happens because real samples average the behavior of a broad set of microscopic conditions, so that is not always clear which one should be responsible for which effect. Besides, it is also true that, from the theoretical point of view, results can be very much affected by the set of parameters which defines the equations of the system.

In summary, from one side there is a lack of specific bibliographic references and from the other a large span of possible outcomes, and this study just lies in between. For this reason, a preliminary analysis has to be performed, focusing this two aspect at the same time. From literature, lots of data are available either experimental and theoretical; nevertheless, besides gathering and systematizing them, it is worth to test their influence on the behavior of the system. In other words, check the response of the system to small variations of the parameters, in order to understand how different set are able to change the outcome. We evaluate some common potentials through analytical calculations and MC simulations to provide some important hints that should be taken into account when each one of them is applied to a nanotube system. Furthermore, adsorption analysis investigates the effect of geometrical properties on the loading isotherm plot, towards a more precise comparison with real data from broad PSD samples.

In practice, since this work is about adsorption or, in a broader meaning, hydrogen storage, we focus on the uptake/release of hydrogen molecules, as well as their diffusion within CNT porous systems. The purpose of building up a diffusion scheme is to understand, not only from a thermodynamic point of view, the loading process but hopefully, to get a better insight on the accessibility of a CNT sample as well as the response time of the uptake/release mechanism. As explained above, real samples are very mimic through a single theoretical model, due to the extreme variety of possibilities. For this reason, an approach that takes fluctuations into account should be preferable in this case. On the other hand, MC algorithms do not frequently apply to dynamic studies because of the restrictions that time dependence imply. The strategy adopted here involves keeping constant the average temperature at each MC step, thus relating the mean displacement to the time span through the kinetic theory of gases.

Furthermore, a deeper investigation about physical properties, led to wonder if the symmetry of the system, which is strictly bound to geometrical parameters, was capable of inducing or promoting a phase transition in the adsorbed molecules (as illustrate in figure 1.3, result of MC simulation).

Moreover, an ordered disordered phase transition has been suggested of the molecules adsorbed on graphite systems[109], but CNT systems has different symmetry. In fact any adsorbed layer has, in this case, one degree of freedom less, due to the circular conformation. At least a loss of degeneracy should be considered because, while in graphite the adsorbed layer can expand freely in two directions (planar conformation), inside CNTs only in the direction of the axis, whereas any other expansion would need to change the distance between the layer and the substrate, and, therefore , results in an increasing the energy of the system.

Such context also enlighten some issues about the insertion algorithm used in MC simulations. In these conditions, the estimation of the insertion probability converges very slowly due to the high local density and the above mentioned loss of degeneracy. Therefore, with the purpose of further developing this branch of investigation, a new algorithm has been proposed.

Chapter 2

Monte Carlo method

The question was what are the chances that a Canfield solitaire laid out with 52 cards will come out successfully?

After spending a lot of time trying to estimate them by pure combinatorial calculations, I wondered whether a more practical method than "abstract thinking" might not be to lay it out say one hundred times and simply observe and count the number of successful plays. (S. Ulam, 1946)

2.1 Historical remarks

The name *Monte Carlo* was suggested by Nicholas Metropolis in 1949, with explicit reference to gambling, describing a method which would use random numbers in order to study differential equations[68]. Although statistical sampling methods have long been known, only with the improvement of computational techniques it came to be feasible for complex calculations. On the basis of the law of large number and the new developments in the theory of probabilities, the method was firstly applied on neutron diffusion[107], but was soon clear that the applications would involve various branches of the natural sciences[70].

2.2 Meaning of randomness

Lots of methods and algorithms can be numbered under the category of MC; what they indeed have in common is that they make use of random numbers in order to solve complex problems. The main idea behind this approach lies into transforming a complex calculation (*e.g.* integration) into a matter of probabilities. An early example of such kind of situation is known as *Buffon's needle*, which dates back to the $18th$ century. The experiment consists of tossing a needle randomly on a surface divided into stripes: the probability of the needle being in contact with the edge of a stripe can be related to the value of π. Therefore one can easily get an estimation of π by means of the frequencies. In other words, it is just like calculating the average result of a weighted dice: we could calculate an integral above the mass distribution of the dice, or simply toss it so many times that the frequency of each side is close enough to its probability.

Nevertheless, MC is not just an approximation of what analytical methods cannot easily calculate; one of its advantages is that, as long as the statistical sampling coverage is sufficient, the information gathered is not limited to average values. This means that, many times, data from a single or few simulations can be extrapolated to different conditions and produce results for a large amount of situations. The only limit is indeed the sampling, which need to be large as the extrapolation moves far from the simulation. A compromise is usually found combining multiple simulations in order to maximise the ratio between coverage and time consumed.

2.3 Monte Carlo sampling

The core of a MC simulation is undoubtedly the way how the samples are generated. Since the beginning this has been a non-trivial issue[25].

2.3.1 Uniform random numbers

Real random numbers have been obtained in several ways, measuring physical quantities (*e.g.* radioactive decays) and removing all bias which could arise from the measurement method. For instance, α decay has been used in conjunction with a high sensitive counter; the number of decays within $20ms$ would produce a sequence of bit, storing 0 or 1 according to whether the count was even or odd respectively[36].

Bits were then coupled and discarded if they were 1 1 or 0 0, thus correcting an eventual difference between the probabilities of generating a 0 or a 1. The couples remaining were just 1 0 or 0 1, which produce respectively 0 or 1 in the final bit sequence. Finally the bit sequence can be divided into fragments of the needed size. This way the sequence could be stored and used for calculations.

It is clear that this approach is not feasible for fast calculations, for the access to memory is a very slow process, compared with other processing capabilities. For this reason *pseudo-random* generator has been soon developed, where number are generated through fast and low memory-consuming algorithms, using the previous number as a seed for the next one. Since the method is thus deterministic, the sequence is reproducible, which is essential for debugging codes.

From now on the expression "*random* numbers" will refer to *pseudo-random* numbers generated within the interval $[0, 1[$.

2.3.2 Monte Carlo Integration

Once we have a proper set of random numbers it becomes possible to evaluate integrals using stochastic means.

Having indeed a generic function $f(x)$ integrable within the interval $[a, b]$, with $a < b$, and a uniform function $g(x)$ defined as follows

$$g(x) = \begin{cases} \frac{1}{b-a} & \text{if } a \leq x \leq b, \\ 0 & \text{elsewhere.} \end{cases}$$

the following integral can be considered as an expectation value of $f(x)$ with x random variable distributed according to $g(x)$

$$(b-a)\int_a^b f(x)g(x)dx \tag{2.1}$$

Therefore, according to the *Strong law of large numbers*, the above integral can be estimated as

$$(b-a)\frac{1}{N}\sum_{i=1}^{N} f(x_i)$$

where $\{x_i\}$ are N random numbers in the interval $[a, b]$ generated according to $g(x)$. We can therefore generalise

$$\int_a^b f(x)dx \simeq \frac{1}{N}\sum_{i=1}^{N}\frac{f(x_i)}{g(x_i)} \tag{2.2}$$

where $f(x)$, $g(x)$ and $\{x_i\}$ are the same mentioned above. The symbol $\simeq$ means that the right part of the equation is an estimation of the value of the integral. Such estimation, although it certainly converges for $N \to \infty$, it will be more accurate as N increases.

Indeed if we apply the definition of the *variance* to the estimator we can conclude that

$$\sigma^2 \left[\frac{1}{N} \sum_{i=1}^{N} \frac{f(x_i)}{g(x_i)} \right] = \frac{1}{N} \sigma^2[Y] \tag{2.3}$$

which means that the *standard deviation* is proportional to $1/\sqrt{N}$. In other words, to reduce the error by ten, we need to increase the number of steps by one hundred times. Despite such drawback, MC methods have the advantage that the convergence rate does not depend, or depends very slowly, on the dimensionality of the system. This especial characteristic make this approach very useful for systems with multiple degrees of freedom.

2.3.3 Importance sampling

In many cases, sampling uniformly a multi dimensional domain is not straightforward. Usually in mathematical analysis such spaces need to be normalized, with respect to each one of the variables. It happens almost the same when trying to sample a non-squared space (*i.e.* a space where the domain of one variable depends on the values of any of the others). In these cases we need to correct this effect with a non uniform sampling.

Moreover, as shown in previous section (see eq. 2.3), increasing the number of steps is not an efficient way for reducing the error, although in many cases it is the only path available. A very effective way of achieving such goal is to choose the random distribution $g(x)$ (see eq. 2.2) very similar to $f(x)$, with the requirement that $g(x)$ is non-zero wherever $f(x)$ is non-zero. This improvement is especially needed if $f(x)$ is steep and varies a lot, with zones where the function is significantly greater than in others. Knowing which are these zones would allow to sample them with higher frequency, with obvious benefits for the overall performance. Obviously the random distribution $g(x)$ cannot be equal to $f(x)$ because this would imply that we actually already know the integral of $f(x)$, since it is implicit within the normalization of $g(x)$.

The sampling should be therefore studied very carefully in the light of every possible information which could somehow predict the shape of the function $f(x)$. It should be said, nevertheless, that the choice of the sampling function $g(x)$ does not affect the

value of the integral or of its estimate in the end, it only enhances (or not) the velocity of the convergence. In practice, it is then necessary to apply the chosen distribution to the random generator, *i.e.* to make it generate random numbers according to $g(x)$.

Rejection method

One of the earliest methods was the rejection one[25]. Basically it transforms one distribution into another. Since it does not need any analytical knowledge of the sampling function it is very suitable for empirical functions or, as mentioned above, for correcting geometrical domains. So, if we are able to generate random numbers according to a specific distribution (*e.g.* uniform) $u(x)$, we can convert them into any non singular distribution $\gamma(x)$ with the same domain, be for instance the interval $[a, b]$.

In the first place, it should exist a real value k so that

$$k\ u(x) \geq \gamma(x) \qquad \forall x \in [a, b]$$

In principle k could be any value greater than $\max[\gamma(x)/u(x)]$ however, the greater it is, the less effective the algorithm will be, since its discard rate will also be greater. Therefore k should be as low as possible in order to maximise effectiveness (see picture 2.1).

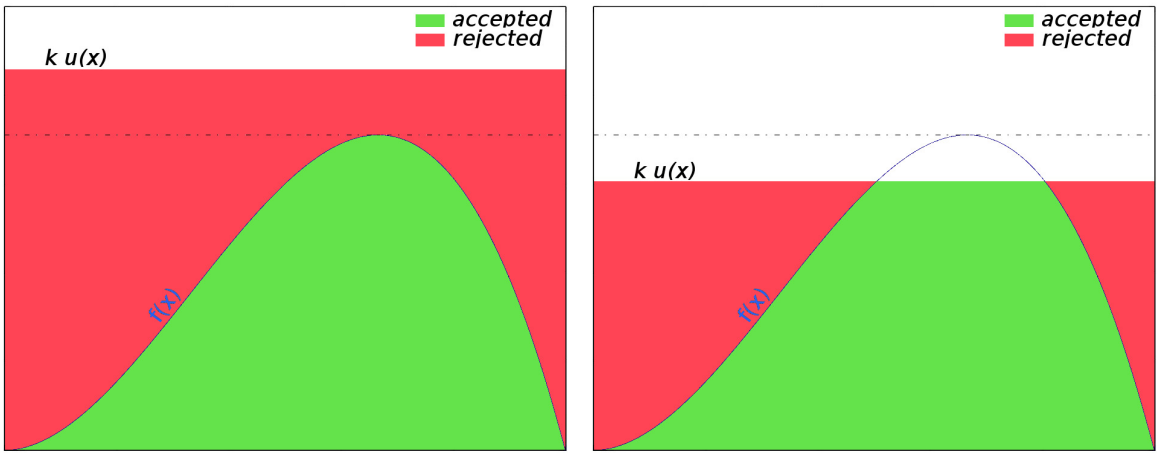

Figure 2.1: *Sampling of a function $f(x)$ with rejection method: if k is greater than the maximum, the number of rejections is increased without any benefit (left inset); if k is not large enough the function $f(x)$ is not sampled properly (right inset).*

In the case of $u(x)$ uniform in $[0, 1[$ the algorithm proceeds as follows; the generalisation is straightforward. A first random number x_i is chosen in the interval $[a, b[$, and then

a second one γ_i is taken between 0 and $k\ u(x_i)$

$$\begin{aligned} x_i &= (b-a)\eta_1 + a \\ \gamma_i &= k\ u(x_i)\eta_2 \end{aligned} \tag{2.4}$$

being η_1 and η_2 two random numbers in the interval $[0, 1[$. The *i-th* sample is then considered if

$$\gamma_i \leq \gamma(x_i) \tag{2.5}$$

otherwise is discarded. In this way the $\{x_i\}$ are generated according to the general distribution $\gamma(x)$. Because of the presence of the k value, $\gamma(x)$ doesn't even need to be normalised, thus making this method extremely useful for empirical distributions.

Since the method actually samples both distributions, the acceptance rate can be used to evaluate the integral of a generic function $f(x)$ (see eq. 2.1). The fraction of accepted samples can be an estimation of the ratio between the integrals of the two distributions, $f(x)$ and $k\ u(x)$ respectively.

Thus, if the number of samples N is sufficiently large,

$$\int_a^b f(x)dx = k \int_a^b u(x)dx\ \frac{N_{acc}}{N} \tag{2.6}$$

the value of the integral is easily obtained by counting the number of accepted samples N_{acc}, since k is known and $u(x)$ is normalised, so its integral is actually 1.

In general the efficiency of the method depends on the acceptance rate so, besides the influence of k in increasing the rejections (see figure 2.1), sampling, for instance, a stiff peaked function with uniform distribution would result in a poor precision, or a very low convergence rate. The solution is therefore to choose a distribution $u(x)$, reasonably easy to sample, but also similar in shape with the function under evaluation.

Inversion method

Another method, which does not suffer from the loss of efficiency of the rejection, consists of directly sampling according to a specific function $f(x)$. The main disadvantage, compared to the previous method, lies in the amount of information needed about $f(x)$. One of the first uses of this sampling was to generate random neutron flights with an exponentially decreasing distribution[25]. Indeed, given two random variables X and Z, distributed according to $u(x)$ and $g(z)$ respectively, and a function

$Z = f(X)$, all those elements are linked together by the relation:

$$g(z) = \int u(x)\ \delta\left(z - f(x)\right) dx. \tag{2.7}$$

The middle term on the right side is the delta function, defined as

$$\delta(x) = \begin{cases} 1 & \text{if} \quad x = 0 \\ 0 & \text{if} \quad x \neq 0. \end{cases}$$

If $f(X)$ is monotonic the integral leads to

$$g(z) = \left|\frac{dz}{dx}\right|^{-1} u\left(x(z)\right) \tag{2.8}$$

where $x(z)$ means the solution of the equation $z = f(x)$ at fixed z. For the sake of completeness, if the function is not monotonic there could be more than one solution for the equation. If N solutions $\{x_i\}$ exist, the equation 2.8 becomes

$$g(z) = \sum_{i=1}^{N} \frac{1}{\left|f'\left(x_i(z)\right)\right|} u\left(x_i(z)\right). \tag{2.9}$$

From 2.8 it is easy to see that the cumulative distribution

$$z = f(x) = \int_{-\infty}^{x} \gamma(t)dt \tag{2.10}$$

is always a uniform random variable in the interval $[0, 1[$ regardless of the distribution $\gamma(t)$. Knowing that it is possible to generate $\{x_i\}$ random numbers with any distribution, as long as we can find, analytically or numerically, the solution of the equation

$$f(x_i) = \eta_i \tag{2.11}$$

for each of the η_i random numbers uniformly generated in $[0, 1[$. However, having to numerically solve an equation for each random number generated will probably lead to even lower efficiency than the rejection method, and the same could happen if the analytical solution is too much complex.

For this reason it is sometimes useful to use both methods. This is possible if the main function can be expressed as $f(x) = g(x)h(x)$ where $h(x)$ is a function which is easy to invert and to implement. In practice random numbers $\{x_i\}$ are generated according to $h(x)$ and then selected through the rejection method if a second, uniform, random number is lower than $g(x_i)$.

2.4 Statistical thermodynamics

Once we have seen how to efficiently integrate complex functions by means of MC techniques, the main goal of this section is to present how such integrals should be, in order to properly describe macroscopic molecular behavior. A simulated system will have as many degrees of freedom as the variables which are free to change during the simulation. A miscrostate is defined as a specific configuration of all the variables of the system. Therefore, a single particle, for instance, would have 6 degrees of freedom: 3 for its position in each one of the xyz axis and the same for its momentum. All possible microstates comprise the phase space.

That said, from a macroscopic point of view, a system is composed by multiple different microstates, so that some thermodynamic properties (*i.e.* mechanical properties) can be calculated as an average value. This means that we can follow a statistical approach by studying microstates distribution, and therefore estimate such properties.

$$\langle E \rangle = \lim_{N \to \infty} \quad \frac{1}{N} \sum_{m=1}^{N} E_m \tag{2.12}$$

Thermal properties (*i.e.* non-mechanical) cannot be determined in such way since they depend on the whole phase space. Some methods exist[110] nevertheless, to approximate them as if they were mechanical ones.

A so called *ensemble* consists of a large number of replicas of the system, each one representing a microstate. They can be grouped according to one of the variables (*e.g.* energy), generating a statistics that shows which energies are more representative and how much.

$$\sum_{E} \frac{n_E}{N} E = \sum_{E} f_E \; E$$

Instead of summing over the microstates we are scanning all possible energies, being n_E and f_E the number of states with a specific energy and its frequency, respectively. It is straightforward that, with N sufficiently large, the frequency approaches the real probability $f_E \to \wp_E$. Of course the key point would be the coverage, because it is unfeasible to explore the entire phase space, even for small systems, but the sample has to be large enough to be a statistically significant representation of the system under investigation (*i.e.* estimations do not vary too much from sample to sample). Besides, some techniques are designed to increase the sampling rate in some areas of the phase space, at the cost, of course, of the sampling in other regions[79][96]. This is usually done when some areas can be *a priori* excluded without being explored[97].

With discrete variables microstates are easy to handle, nevertheless, generally, many studied variables are continuous, thus making the number of microstates infinite. In these cases it is more suitable to apply the concept of density of (micro)states. The sum of 2.12, therefore, becomes an integral

$$\langle E \rangle = \int_{-\infty}^{\infty} \Omega(E) E \; dE \tag{2.13}$$

where E is the energy, but the same treatment could also apply to any variable that can be calculated in the microstate. $\Omega(E)$ is the density of states (DOS), namely the fraction of states whose energies fall between E and $E + dE$; it is also supposed to be normalised so that

$$\int_{-\infty}^{\infty} \Omega(E) dE \; = \; 1.$$

Once Ω is known, all thermodynamic properties can be obtained; however, as it happens in 2.12, we only have access to an estimation, which tends to the real value as the phase space is fully explored.

2.4.1 Ensembles

In an isolated system at equilibrium, with fixed energy, volume and particle number, each microstate is visited an equal number of times. In other words, all states accessible to the system are *a priori* equally probable. Entropy $S(N, V, E)$ can therefore be calculated as a function of the DOS

$$S(N, V, E) = k_B \ln \Omega(N, V, E),$$

being k_B the Boltzmann constant. When $\Omega(E)$ is known, as function of energy, the above can be inverted into $E(N, V, S)$; from there all thermodynamic properties can be calculated through partial derivative

$$T \equiv \left(\frac{\partial E}{\partial S}\right)_{N,V} \quad ; \quad p \equiv -\left(\frac{\partial E}{\partial V}\right)_{N,S} \quad ; \quad \mu \equiv \left(\frac{\partial E}{\partial N}\right)_{V,S},$$

respectively temperature, pressure and chemical potential. Such kind of ensemble is called *microcanonical* but, despite its straightforwardness, is not frequently used, mainly because real isolate systems are not easy to create and even less to maintain.

The *canonical* ensemble, instead, can be visualised as a closed system (constant volume and particle number) in equilibrium with an infinite thermal bath (*i.e.* constant temperature). Such a system certainly resembles experimental conditions much more than the case considered above. It can be shown that the probabilities $\wp_m$ relative

to microstates with different energies, but consistent with a constant temperature, distribute according to an exponential decay

$$\wp_m = \frac{1}{Q} \exp\left(-\frac{E_m}{k_B T}\right)$$

being k_B the Boltzmann constant, T the temperature and E_m the energy of the microstate m. Since the distribution has to be normalised, the proportional constant Q is easily calculated by the sum over all microstates m

$$Q(N,V,T) = \sum_m \exp\left(-\frac{E_m}{k_B T}\right). \tag{2.14}$$

The equation 2.14, known as the *canonical partition function*, is directly correlated to the characteristic thermodynamic function, which is, in this case, the Helmholtz free energy

$$A(N,V,T) = -k_b T \ln(Q) \tag{2.15}$$

Free energy partial derivatives then permit to obtain the other thermodynamic variables.

$$S \equiv \left(\tfrac{\partial A}{\partial T}\right)_{N,V} \quad ; \quad p \equiv -\left(\tfrac{\partial A}{\partial V}\right)_{N,T} \quad ; \quad \mu \equiv \left(\tfrac{\partial A}{\partial N}\right)_{V,T}.$$

Both partition functions $\Omega(N,V,E)$ and $Q(N,V,T)$ are obtained by a sum over all possible microstates: this means scanning the whole domain of all degrees of freedom of the system. Hence, if the energy can be factorised into several independent contributions (in some cases it is possible to divide it into independent groups of correlated variables) this approach greatly reduces the phase space and allows to avoid useless redundancies. Such case frequently happens, for instance, when independent particles are involved: different variables are correlated only if relative to the same particle, otherwise they are considered independent. In the canonical ensemble the energy can so be divided into each particle contribution, therefore is possible to factorise the total partition function into

$$Q(N,V,T) = \prod_{i=1}^{N} q_i$$

where q_i represents each particle contribution. Besides, if N particles are indistinguishable, it means that $N!$ microstates count as a single one, therefore the total partition function becomes $Q = q^N/N!$, where q is the partition function of a single particle. This is also valid for multi component systems, considering each component as a different group of particles.

An open system, in equilibrium with both a thermal bath and a molecule reservoir, is consistent with the *grand canonical* ensemble. In terms of thermodynamic quantities,

temperature (T), volume (V) and chemical potential ($\{\mu_i\} \quad i = 1, \ldots, C$) of all C involved components are fixed; whereas energy (E) and particle number ($\{N_i\}$) are free to fluctuate. By defining a generic open sub-system, immersed in a closed one, and summing over all possible energies and particle numbers (following the same approach described before for the canonical ensemble) we get

$$\Xi(\mu, V, T) = \sum_N \sum_m e^{-\beta(E_m(N)-\mu N)} = \sum_N e^{\beta\mu N} Q(N, V, T) \tag{2.16}$$

where $\beta = (k_b T)^{-1}$ and $E_m(N)$ is the energy of the microstate m with N particles. As in the previous case, the *grand canonical* partition function $\Xi(\mu, V, T)$ is linked with thermodynamic quantities through

$$pV = k_b T \ \ln(\Xi).$$

From 2.16 average particle number is also easily calculated as:

$$\langle N \rangle = k_b T \ \frac{\partial}{\partial \mu}(\ln \Xi).$$

GC simulations can also be used to sample a closed or an isolated system, by considering in the statistics only the samples with a certain particle number or with a certain energy respectively, in practice, it consists of generating a wider phase space and then selecting only the points consistent with the selected conditions. However the simplest and more effective way to exploit such ensemble is to consider a fluid which is in equilibrium with its vapor phase at fixed chemical potential or pressure (the two are easily calculated if the gas phase can be considered ideal). Another example is undoubtedly to load porous materials with adsorbed gas (fluid), in equilibrium with an infinite ideal gas reservoir.

Conditions of constant pressure, volume and particle number are consistent with the *isothermal-isobaric* ensemble. Volume is not constant, but is adjusted in order to compensate an external constant pressure. The system therefore exchanges work and heat, with bariostat and thermostat respectively. Key point of the interpretation of such ensemble lies in the fact that the group made of system and bariostat, constitute a closed system, and therefore obeys to the equation of the canonical ensemble. On the other hand, the whole set (system, bariostat and thermostat) is indeed an isolated system and can be treated as a microcanonical ensemble. The application of such considerations leads to

$$X(N, p, T) = \int_0^\infty Q(N, V, T) \ e^{-\beta p V} \ dV$$

and

$$G(N,p,T) = \mu N = -k_b T \ln X$$

where $Q(N,V,T)$ is the canonical partition function consistent with the volume V, and $G = E - TS + p\langle V\rangle$ is the Gibbs free energy consistent with the ensemble average volume $\langle V\rangle$.

Worth to be mentioned is a special case which involves two boxes able to exchange molecules: it is called Gibbs Ensemble[80] (GE). The system is overall constrained to fixed temperature, total volume and total particle number. To simulate the coexistence of two phases, since temperature is already fixed (just one intensive variable can be set), single box internal equilibrium, equal pressure and chemical potential, are achieved during the simulation. From this definition, the partition function follows

$$Q_G(N,V,T) = \sum_{N_1=0}^{N} \frac{1}{N_1!N_2!} \int_0^V V_1^{N_1} V_2^{N_2}\, dV_1 \sum_{m_1(N_1)} e^{-\beta E_{m_1}} \sum_{m_2(N_2)} e^{-\beta E_{m_2}}$$

with probability density being proportional to

$$\wp(N_1,N,V_1,V,T) \propto \frac{N!}{N_1!N_2!} \exp\Big[N_1 \ln V_1 + N_2 \ln V_2 - \beta\Big(E_1(N_1) + E_2(N_2)\Big)\Big]$$

where $m_i(N_i)$ are all possible microstates of the i-th box consistent with N_i particles, and

$$V = V_1 + V_2$$
$$N = N_1 + N_2$$

being respectively the total volume and particles. In sum, are sampled all the microstates of each box, for each possible division of the volume and particle number between the boxes.

2.4.2 Molecular description

As explained in section 2.4.1, a good way to greatly increases the effectiveness of the method is to isolate the degrees of freedom which belong to the phase space, into small groups of variables. This principle is the basis of the division of the *canonical* partition function into the singular contributions of N indistinguishable molecules

$$Q(N,V,T) = \frac{1}{N!} \prod_{i=1}^{N} q_i = \frac{1}{N!} q^N \tag{2.17}$$

so that we just need to know the partition function q of a single molecule.

In quantum mechanics, the Born-Oppenheimer approximation allow the separation of the electronic and the nuclear wave-functions. This permits the construction of a Potential Energy Surface (PES) as the Schrödinger equation is solved for different values of nuclear coordinates, which are treated like parameters. The assumption is based on the fact that the electrons are thousands times lighter (and therefore faster) than the nuclei, so that their movements can be considered independent. Within a similar approach, the kinetic energy can be divided into translations (E_{transl}), rotations (E_{rot}) and vibrations (E_{vib})

$$E_{total} = E_{electronic} + E_{kinetic} = E_{electronic} + E_{transl} + E_{rot} + E_{vib} \tag{2.18}$$

The reason behind this lies on the fact that each term differs from the others by several orders of magnitude; the only exception is the coupling between vibrations and rotations which sometimes is not negligible.

The molecular partition function of the equation 2.17, can be factorized, according to the relation 2.18

$$q = \sum \exp\left(-\frac{E_{total}}{k_B T}\right) = q_{el} \times q_{transl} \times q_{rot} \times q_{vib} \tag{2.19}$$

where the elements of the right hand side are the partition functions relative to each one of the energy contributions, defined as follows

$$q_{el} = \sum \exp\left(-\frac{E_{electronic}}{k_B T}\right) \tag{2.20}$$

for the electronic conponent and in a similar way for the other ones. It is worth to say that while the sum of the total q (equation 2.19) involves all possible microstates, the factorized elements of the partition function just sum over the states that make changes in the relative energy (*e.g.* equation 2.20 only accounts for electronic energy changes). It is clear that the *canonical* partition function benefits greatly from this proceeding, since the volume dependence can be ascribed entirely to the translation part, and the other just vary with the temperature. For this reason, very often, investigation focus especially on the translation, while keeping the other terms as constant. Comprehensibly, it is also the choice of this work.

From the solution of the electronic Schrödinger equation it is well known that even at high temperature all molecules stay in the fundamental state; if the reference is set so that the $e_0 = 0$, the electronic partition function simplifies to $q_{el} = g_0$ where g_0 represents the degeneracy of the fundamental state. About translations, the eigenvalues of the hamiltonian of a particle of mass m in an element of volume

$V = l_x \times l_y \times l_z$ result from the formula

$$E_{transl} = \frac{h^2}{8m}\left(\frac{n_x^2}{l_x^2}\right) + \frac{h^2}{8m}\left(\frac{n_y^2}{l_y^2}\right) + \frac{h^2}{8m}\left(\frac{n_z^2}{l_z^2}\right) \tag{2.21}$$

with

$$n_x, n_y \text{ and } n_z = 1, 2, 3..., \infty.$$

and h the Plank constant. The calculation of the partition function, in a way analogous to equation 2.20, can also be performed separately for each coordinate. Moreover, if the differences between the energies are small if compared to $k_B T$, the sum can be approximated by an integral, leading to a final result of

$$q_{transl} = \frac{V}{\Lambda^3} \tag{2.22}$$

where

$$\Lambda = \sqrt{\frac{h^2}{2\pi m k_B T}} \tag{2.23}$$

is called the thermal De Broglie wavelength and is related to the expectation value of the linear momentum and defines the condition for a gas to behave as ideal or not, namely if the average space available for each particle is much greater than Λ^3.

The result of 2.22 is of course valid for ideal gases only, however it is especially useful for GC simulations, since it permits to link the chemical potential set in the simulation to the pressure of an ideal gas (see section 3.3 for more detail).

2.5 Markov chains

A Markov chain is a process in which the outcome of a previous trial influence the result of the next one. Thus they are defined as opposed to completely independent events, as well as processes where an outcome depends on all the previous events and not only the last one.

What has been said so far in the previous sections (in particular 2.4.1 and 2.4.2), certainly applies to the former case. The effective sampling of an ensemble, the estimation of an integral through MC methods are all based on the independent, random generation of several points in the function domain (*e.g.* the configurational space). The importance of Markov processes (at least in this context) is the possibility of creating a "random walk", *i.e.* a stepwise route within the phase space made of reasonably small successive displacements chosen randomly at each step. The Markov

criterion grants that, after a sufficient number of iterations, the system visits each possible state with constant probability. In other words such probability becomes independent of the starting point. This property can be used to improve the efficiency of a simulations because the systems under this kind of investigation could count lots of degrees of freedom (*e.g.* at least 3 for each particle involved). Markov property allows to vary just one or few variables at time (that is to take a step) instead of generating a new complete set.

In practice, if we represent, in a vector S, all N possible states s_i of the system, we can define a transformation matrix T

$$\left(\begin{array}{cccc} s_1 & s_2 & \dots & s_N \end{array} \right)_{\mathbf{S}} \times \left(\begin{array}{cccc} p_{1,1} & p_{1,2} & \dots & p_{1,N} \\ p_{2,1} & p_{2,2} & \dots & p_{2,N} \\ \vdots & \vdots & \ddots & \vdots \\ p_{N,1} & p_{N,2} & \dots & p_{N,N} \end{array} \right)_{\mathbf{T}} = \left(\begin{array}{cccc} s'_1 & s'_2 & \dots & s'_N \end{array} \right)_{\mathbf{S'}}$$

which contains all the probabilities $p_{i,j}$ of the system going to the state j from the state i. Both S ans S' are probability vectors, namely their elements are positive and their sum is 1: they represent the probability of the system being in each state.

We can imagine that the starting vector would be all zeros with the exception of an element that is the initial state. The transformation matrix is the change in such probabilities that occur in one step; however it could be applied more times in order to perform multiple changes. So after M steps we have

$$S^{(M)} \quad = \quad S^{(M-1)} \times T \quad = \quad S^{(0)} \times T^{(M)}.$$

The transformation matrix is called *ergodic* if is able to reach all possible states in a limited number of steps, regardless the initial point. That is to say that after m steps the matrix $T^{(m)}$ contains all non-zero elements. Such matrix is called *regular* and one of its properties states that as m tends toward infinity, $T^{(m)}$ tends to a limiting matrix W with all rows equal. Now if we recall the meaning of the elements of the matrix, $p_{i,j}^{(m)}$ is the probability of the system going from state i to state j after m steps. It is straightforward that, if all rows of the matrix are equal, the probability of the system being in any state after $m \to \infty$ steps no longer depends on the initial state i. Moreover, if we call w the common row of the matrix W, we see that such vector is invariant upon the transformation T

$$w \times T = w$$

this implies that after enough steps the probabilities of each state tend to a constant value. It can also be proved that the vector w is unique.

Applying these principles to MC simulations allows therefore to construct an algorithm which pass from one state to another of the configurational space through simple transformations (instead of generating a completely new state each time). Besides, after enough *equilibration* steps, the outcome no longer depends on the initial states. Finally, the frequencies sampled after that, in the so-called *production* stage, estimate probabilities that are a characteristic of the system; increasing the number of steps will enhance such estimation making it more precise.

2.6 Basic simulation algorithm

In a system of N particles, the phase space depends on each particle's position $\{q\}$ and momentum $\{p\}$, having therefore up to $6N$ degrees of freedom. Being $\Gamma(\{q\}, \{p\})$ the overall probability distribution, the estimation of a generic property F is consistent with evaluating the following integral

$$\langle F \rangle = \frac{\int F \cdot \Gamma \; d^{3N}p \; d^{3N}q}{\int \Gamma \; d^{3N}p \; d^{3N}q}. \tag{2.24}$$

At constant temperature, volume and particle number the probability distribution decays exponentially with the increasing of the total energy E (see section 2.4.1),

$$\Gamma = e^{-\beta E(\{q\},\{p\})} \tag{2.25}$$

according the Boltzmann distribution.

Due to the high dimensionality, deterministic methods are not very suitable for such calculation, not as much as MC integration. It should also be said that for most systems, the energy E and therefore the probability distribution Γ depend only on particles positions $\{q\}$, thus reducing the degrees of freedom to just $3N$, because the integral of the kinetic energy term (momenta degrees of freedom) can be solved analytically. This could be a lot anyway, if the system is large.

2.6.1 Metropolis formulation

First developed in the early 50s, the algorithm aims to evaluate thermodynamic state properties of a simulated system[69]. It should be pointed out that the distribution of 2.25 is not known *a priori* since it depends on the energy, which is calculated for each specific microstate. So the method divides the generation of new configurations into

two steps which are the generation of a trial configuration and the acceptance or not of such trial. The probability $P(\mu'|\mu)$ of going from the configuration μ of the system to a specific new one μ' is therefore

$$P(\mu'|\mu) = g(\mu \to \mu')\ a(\mu \to \mu') \tag{2.26}$$

where g and a are, respectively, the generation and acceptance probability of the configuration μ'. In the basic Metropolis implementation the generation distribution is symmetric, which means that all states are generated with the same probability: in practice

$$g(\mu \to \mu') = g(\mu' \to \mu) \tag{2.27}$$

is valid for any two sates a and b of the phase space.

Implicit in the formulation of the algorithm are the detailed balance and the ergodicity, which ensure respectively the existence and uniqueness of the stationary probability distribution of the Markov chain (see section 2.5). Ergodicity means that each possible configuration is reached in a finite number of steps and that the system does not have any tendency to return periodically to some points. The detailed balance, on the other hand, states that the probability of the system going from an old configuration μ to a new configuration μ' should be equal to the reverse one, *i.e.* the probability of going from the old to the new one.

$$\pi(\mu) \cdot P(\mu'|\mu) = \pi(\mu') \cdot P(\mu|\mu') \tag{2.28}$$

It does not include only the transition probabilities of equation 2.26, but also $\pi(\mu)$ and $\pi(\mu')$ which are not known *a priori*. They represent respectively the probability of the system being in μ and μ'. This condition, although it is not necessary, is sufficient for the system to reach a stationary solution, namely a distribution that do not vary significantly with further steps (see section 2.5).

In detail, the algorithm generates new conformations by means of displacement trials. This means that during a single step one or more particles attempt to move to any positions within a cube centred on the old one. For each particle the new coordinates are selected according to the formula:

$$g : \begin{cases} X \to X + \xi_1\ \alpha \\ Y \to Y + \xi_2\ \alpha \\ Z \to Z + \xi_3\ \alpha \end{cases} \tag{2.29}$$

where $\{\xi_i\}$ are three random numbers uniformly distributed between -1 and 1 and α is the edge of the cube. The choice of α is arbitrary, but it shouldn't be made

carelessly. A high value would probably imply low acceptance rate, whereas a too low one means that sampled configurations are very similar and, therefore, more steps will be needed, in order to have significant coverage of the phase space. Since the displacement is uniform, any point of the space is available in a finite number of steps and the ergodicity is granted. The 2.29 is also proven symmetrical, since the probability is the same for any displacement within the α range, and zero otherwise.

Once selected, the total energy of the trial configuration can be calculated according to the chosen interaction potential V

$$E(\{q\}) = \sum_{i=1}^{N-1} \sum_{j=i+1}^{N} V(d_{ij})$$

which depends only on the distance between the particles d_{ij}. Afterwards, the energies of the old and the new configurations (E_{old} and E_{new} respectively) are compared, in order to apply the acceptance criterion. If $E_{new} < E_{old}$ the new configuration is automatically accepted; if $E_{new} > E_{old}$ a random number η is generated in the interval $[0, 1[$, therefore the new configuration is accepted if $\eta < \exp[-\beta(E_{new} - E_{old})]$, otherwise is rejected. When a configuration is rejected means that the old conformation is sampled again. So being $\Delta E = E_{new} - E_{old}$ we can say that for two states μ and μ'

$$a(\mu \to \mu') = \min\left[1, e^{-\beta \Delta E}\right] \tag{2.30}$$

By substituting 2.30 and 2.26 into 2.28, and taking out the generation probability for being symmetric (2.27), if we assume $E_\mu < E_{\mu'}$

$$\pi(\mu) \cdot e^{-\beta \Delta E} = \pi(\mu')$$

wich leads to conclude that the state with higher energy (say μ') is visited $e^{-\beta(E_{\mu'} - E_\mu)}$ less times than the lower energy one (μ). Extending this treatment to all possible states is possible to conclude,

$$\pi(\mu) \propto e^{-\beta(E_\mu - E_{min})} = K \cdot e^{-\beta E_\mu} \tag{2.31}$$

which confirms that the stationary distribution follow the Boltzmann exponential decay from 2.25. The minimum energy E_{min} is not necessarily known, because the 2.31 works as well with local minima.

The integral from 2.24 is estimated as the average of M measures

$$\langle F \rangle = \frac{1}{M} \sum_{i=1}^{M} f_i.$$

The number of measures can be lower or equal ($M \leq N$) to the number of steps, in order to compensate, eventually, the self-correlations of consecutive steps which are not strictly independent of the previous configuration. In this way we sample the most probable energies, corresponding to the highest values of $\Omega(N, V, E)$, and weight them according to the Boltzmann factor $e^{-\beta E}$.

2.6.2 Low rate events

In the previous section it has been explained that the integral 2.24 is calculated over all possible energies E, by taking into account the relative DOS $\Omega(E)$ and the distribution Γ. The first is granted by the sampling algorithm, whereas the other by the acceptance criteria.

As seen in equation 2.3, variance decrease with the increasing of the number of samples. This can be true also locally, meaning that variance of frequently sampled states will be lower than other states. In fact, if the function Γ is high in a zone where the distribution Ω is low, it will result in a slower convergence (*i.e.* higher variance) than the case of both having similar shape. In other words, if high-Γ configurations are not easily generated by the algorithm, the convergence will be poor. Therefore we could find some over-sampled zones, where new data do not significantly improve the information already gathered, and, on the other hand, some high variance zones which, in practice, greatly limit the accuracy of the result.

In order to reduce this variance inherent to the method without increasing the number of samples (which could be computationally expensive), we can either increase the percentage of relevant points or increase the information got at each point of the simulation[25]. In practice, what should be increased is the coverage of such high-Γ low-Ω zones or, more realistically, low-Ω zones which, based on previous information, have presumably high-Γ.

A possible approach is to bias the system towards such rare conditions. In this way the coverage of the most probable microstates is reduced, simultaneously increasing the outcome of a certain type of rare events. The biasing factor is arbitrary but should be chosen carefully; the information gathered is then weighted by the inverse of its value so that the result, in the limit of full coverage, remains the same.

When trying to improve a low rate event of a specific type, it is possible to perform an extra sample of that type at each step and weight the relative information by the acceptance probability. The decision process then proceed according to the common

algorithm. In this way, regardless of the states sampled through the main course, we continuously gather small amounts of information about the event of interest. The computational time is certainly increased since two samples per step are generated, however, being some processes in common for the regular and the extra one, the time is generally lower than with the double of the steps. Moreover, in terms of coverage it is equivalent to spread the points of interest onto a wider area, so that it fits better.

configurational bias

Born as an improvement of Widom insertion[110], the configurational bias[96] (CB) applies the chain growth random-walk developed by Rosenbluth *et al.*[88] to improve the creation of a branched molecule into a high dense system. The original formulation of the method was just about the creation of a molecule, in order to test the capacity of the system to host a new one. Eventually, it has been applied to improve MC simulations[97].

To implement a step-wise procedure, it is possible, for instance, to insert a compressed molecule (which then expands in further steps) or, for branched molecules, insert one fragment at a time and driving the choice of the conformation towards the most favourable, until all pieces are placed together[96]. The latter is the basic concept behind CB, initially developed into a lattice model, so that, at each step, all possible and available sites could be evaluated. In this way the growth automatically tries to avoid overlaps with other occupied sites[88]. Depending on the whereabouts, each insertion has a different number of possibilities (*i.e.* number of non-overlapping conformations): to take this into account, each insertion should be weighted by the number of available sites. In other words, an insertion in which, for instance, 5 sites were available should weight five times more than one with just one possibility. In fact the Rosenbluth weight[88], defined as follows

$$W = \prod_{i=1}^{m} \left(\frac{n_i'}{n_i} \right), \tag{2.32}$$

applies such correction to an m-step growth, where, at each step, n_i' are the available sites, of the n_i total possible ones. The weight, in practice, automatically accounts for the non-available conformations: in this way, instead of counting just 1's and 0's, according to the conformation being or not available, the final estimation comes as an average of small probabilities, clearly enhancing the convergence rate per step. However, the procedure involved is more complex (*i.e.* more operations per step) than a simple random try, therefore its effectiveness drops as the acceptance frequency

increases. As a matter of fact, a high acceptance rate could not increase significantly, and the application of CB could not be worthwhile.

The algorithm so far presented is a self-avoiding random walk, which applies to rigid spheres in a lattice. At each growth step, each available outcome has $1/n_i'$ probability of being selected, compared with $1/n_i$ when unbiased, so the ratio between the two produces the equation 2.32 above. However, if interactions are involved, not all configurations have the same probability within the phase space: the available ones will indeed distribute according to Boltzmann factor. Assuming that the total energy of the insertion u_Γ can be divided into the contributions $\overline{u}_i$ of the m fragments, the total probability can be expressed as the combination of the individual insertion events.

$$P = \prod_{i=1}^{m} P_i = \prod_{i=1}^{m} \exp(-\beta\ \overline{u}_i) \tag{2.33}$$

Moreover, if each fragment i is chosen among n_i available sites, at each step, the probability of being selected becomes

$$P_i{}' = \frac{\exp(-\beta\ \overline{u}_i)}{\sum_{j=1}^{n_i} \exp(-\beta\ u_{ij})} \tag{2.34}$$

where u_{ij} are the energies of the n_i trial sites. It is clear from the above that overlaps or high energy sites will have zero or negligible contribution. Consequently comparing 2.33 and 2.34 it is clear that the total weight will be

$$W = \prod_{i=1}^{m} \left[\sum_{j=1}^{n_i} \exp(-\beta\ u_{ij}) \right]. \tag{2.35}$$

In a lattice model it is easy to account for all possible orientations or positions of each fragment; this allows us to consider an insertion in absolute terms. Nevertheless, when a continuous space is applied, and chains are completely flexible, the total number of possible conformations is infinite[35]. An exhaustive scan is obviously not feasible, so an arbitrary number of trial conformation is considered at each step as a sample of all possibilities. In these conditions, the n_i of equation 2.35 does not depend on the system, but is an arbitrary number, so that an absolute calculation of the weight is meaningless. We can, however, compare two different insertions because the ratio between the weights calculated in that way is still a good estimation of the ratio between the limit values, *i.e.* the weights for n_i tending towards infinite.

Following the Metropolis scheme, the new configuration is then accepted according to the criterion[97]

$$\alpha(\mu \to \mu') = \min\left[1, \frac{W_{\mu'}}{W_\mu}\right]$$

which is analogous to 2.30, but the weight ratio corrects the biasing effect. The overall distribution will therefore follow

$$P = \prod_{i=1}^{m} P_i \times \alpha(\mu \to \mu') = \exp(-\beta\ u_\Gamma)$$

so the detailed balance is also respected.

2.7 Advanced techniques

Here we present some recent techniques which modify the general algorithm in order to adapt to some specific problems. The *kinetic* Monte Carlo, for instance, describe a possible approach to define the variable time during a simulation and, therefore, producing time-dependent trajectories. The other methods considered here are especially useful for dealing with phase transitions, taking real advantage of the information produced by MC method and its fluctuating sampling. They extend the range of a single simulation and allow to extrapolate information about conditions that were not actually simulated (*e.g.* think of the difficulty of simulating an unknown phase transition having to exactly match the conditions of pressure and temperature)

Some of the following were actually implemented during this work, other were used as a reference for developing new methods.

2.7.1 Kinetic Monte Carlo

When trying to foresee the evolution of a system through time, the simplest and relatively accurate method is classic MD. Some interaction potential defines the laws of motion and the method aims then to integrate the equation of motion over the time span being investigated. The interaction potential therefore balance the accuracy and the simplicity of the method. Furthermore, the main difference between MC and MD method is that the former do not involve solving the aforementioned equations. In many cases this means an increase of simplicity (and time efficiency as well) without loosing accuracy, therefore greatly increasing the time span available for investigation.

However, in time dependent problems, it is actually the equations of motion that make the connection between a single state of the system and its possible evolution in the subsequent instants of time. MC method proceeds step-wise, this means that the system has to "jump" from a state to another; the key point for time dependence would be to provide an appropriate time frame to each one of this steps.

Among the many possible ways of doing so, we present the one we have implemented in this work for studying the diffusion of hydrogen molecules inside CNTs[85]. The algorithm starts by generating random samples according to Boltzmann distribution. During a cycle, each particle of the system makes a displacement attempt, which could be accepted or not according to Metropolis criterion (equation 2.30, section 2.6.1). Once a new configuration is obtained, a time of occurrence is assigned to the total displacement based on the Kinetic Theory of Gases.

The Maxwell-Boltzmann's distribution,

$$f(v) = (\frac{m}{2\pi kT})^{3/2} 4\pi v^2 e^{\frac{-mv^2}{2kT}} \tag{2.36}$$

is used to obtain the mean square speed of the H_2 molecule. This mean square speed is the second-order moment of speed of the molecular hydrogen's speed distribution, which is given by:

$$\langle v^2 \rangle = \int_0^{+\infty} f(v) v^2 dv = \frac{3RT}{M} \tag{2.37}$$

where R is the gas constant, T is the temperature and M is the molecular mass. Therefore, by knowing the mean square speed of the hydrogen molecule, $\langle v^2 \rangle$, and the mean square displacement that occurred in each cycle, $\langle \Delta r^2 \rangle$, it is possible to determine the time taken by the cycle to occur:

$$t = \sqrt{\frac{\langle \Delta r^2 \rangle}{\langle v^2 \rangle}} \tag{2.38}$$

By using the mean square speed, $\langle v^2 \rangle$, the average kinetic energy is kept constant during each cycle, making the ocurrence of different microstates only dependent on the potential energy of the system. Moreover, since in equilibrium conditions the average potential energy of the system does not change, the average total energy of the system is conserved. Consequently, in this work, we are working in a framework where the average total energy of the system is constant and there is no exchange between kinetic and potential energy. Hence, the further reported self-diffusion coefficients (D_s) correspond to Brownian motion in equilibrium situations.

2.7.2 Expanded ensembles

The Expanded ensemble, basically, tries to overtake the sampling distribution of the Metropolis algorithm, with the plain advantage of exploring the improbable zones of the phase space. Due to this characteristic, it belongs to the flat-histogram techniques, because it tends to sample all states with the same frequency. It does not suffer of the so-called defect of clumping, *i.e.* the tendency of the results keeping grouped, in a small, favorable zone. The main drawback is that, in Metropolis algorithm, the new points are only needed to weight that "zone" with respect to its probability, but they do not add more information about chemical or physical properties. For the same reason, improbable zones of the configuration space are often under-sampled or no sampled at all. More problems can also arise, for instance, when the sampling needs to overtake energy barriers, as could be the case of phase transitions.

Lyubartsev *et al.* proposed a procedure that can increase the coverage and allow the calculation of, for instance, the *canonical* free energy with just one MC run[63]. So the partition function of equation 2.14 (section 2.4.1), can be written in the form

$$Q(N,V,T) = \frac{1}{N!}\int \prod_{i}^{N} e^{-\beta E(q_i)} dq_i \tag{2.39}$$

where the sum has been replaced by an integral over all degrees of freedom q_i of the N indistinguishable particles, being $E(q_i)$ the respective energy and $\beta = 1/k_B T$ the reciprocal temperature. We can now consider a set of M intermediate values for β, from zero up to the temperature under investigation

$$0 = \beta_0 < \beta_1 < \beta_2 < ... < \beta_m < \beta$$

each one of them could constitute a canonical ensemble (at fixed N and V) with its partition function similar to equation 2.39. It starts from $\beta = 0$ because in this case the 2.39 is easily solved

$$Q_0 = V^N/N!$$

without any further knowledge of the system. At this point a random walk could explore an ensemble, say m, and occasionally swap to another one, say n, with probability $P = min[1, exp(-\Delta\beta\ E(q_i))]$, while keeping fixed all the variables q_i; being $\Delta\beta = \beta_n - \beta_m$. The probability of the random walk visiting each ensemble will therefore be proportional to its partition function $p_m \propto Q_m$, or in other words that the relative probability of an ensemble over another will be equal to their partition function ratio. Hence, knowing the relative probabilities, it is possible, at least in

theory, to know the partition function, and therefore the free energy from equation 2.15.

An infinite simulation will certainly work. However, we can see from equation 2.39 that the probability of visiting an ensemble decays exponentially with the increase of β. This means that the procedure presented so far will stay in just a few ensembles, without getting enough samples to properly estimate the probabilities of each ensemble (notice that the ensemble we are actually investigating is the least probable in this scheme). It is crucial to weight each ensemble so that the random walk stays in each ensemble with the same or similar (at least the same order of magnitude) frequency. So the probability of accepting a swap move will be

$$P(m \to n) = \min[1, exp(-(\beta_n - \beta_m)E(q_i)) + \eta_n - \eta_m] \tag{2.40}$$

where η_n and η_m are the weights of the two ensembles involved in the swap. From the previous considerations it is clear that the best values of the weight will be respectively $\ln(Z_m)$ and $\ln(Z_n)$, which is exactly the result that the simulation seeks, so it is initially unknown. However, a few short simulations can easily help finding a value good enough.

In practice, after choosing an arbitrary value, it is only needed to check the frequencies produced and modify the new weight in order to equalize them (*i.e.* increase the weight of the less visited ensemble). Such process can be automated so that the resources spent in this search will be minimized.

An identical scheme can be applied to other ensembles and variables. For example the GC can be considered as a set of canonical ensembles with different particle number (constant β, variable N). This is the basis of the Transition Matrix (TM) algorithm which will be explained in section 2.7.4.

2.7.3 Histogram Reweighting method

The amount of information gathered from a MC simulation could be greatly increased by means of histogram analysis[30]. Such method aims to deduce from a simulation, not only the averages, but the probability distribution itself, so that it could be applied to different conditions within a range of the ones used to run the simulation. The key point would be having a good representation of the whole phase space, otherwise the error affecting extrapolated averages (*i.e.* at different conditions) would

be considerable. Thus the probability of a certain state is

$$P_K(S) = \frac{1}{Z(K)} N(S) \exp[KS] \tag{2.41}$$

where K is a generic simulation parameter and S an operator over the phase space, such that the resultant hamiltonian would be $H = KS$; The canonical partition function of the system is

$$Z(K) = \sum_S N(S) \exp[KS] \tag{2.42}$$

and $N(S)$ is the number of configurations at the point S of the phase space. Obviously that we have very little information about states where $\exp[KS] \ll 1$ even for large variations of $N(S)$. In order to have the best results, all the most representative states should be sampled, so our system cannot be too far from critical points, if involved, otherwise we would be neglecting the contribution of one of the phases. The histogram reweighting procedure also permits to join histograms together and thus broaden the sample. It is nevertheless needed that the histograms would overlap each other and, of course, when performing phase coexistence calculations, both liquid and vapour properties have to be sampled. If the simulation is long enough, the histogram produces an estimation of the probability and therefore of the DOS. Indeed, knowing $N(S)$, from (2.41) is therefore possible to extrapolate an estimation of $P_{K'}(S)$ at $K' \neq K$.

$$N(S) \;=\; Z(K) P_K(S) \exp[-KS] \tag{2.43}$$

We write the equation (2.41) for a parameter K' and substitute the $N(S)$ from (2.43)

$$P_{K'}(S) = \frac{Z(K)}{Z(K')} P_K(S) \exp[(K' - K)S]. \tag{2.44}$$

Then, considering the equation (2.42) at K' and combining with (2.43) we obtain

$$Z(K') = Z(K) \sum_S P_K(S) \exp[(K' - K)S]$$

which could be rearranged as follows

$$\frac{Z(K')}{Z(K)} = \sum_S P_K(S) \exp[(K' - K)S] \tag{2.45}$$

and finally substitute into the (2.44) leading to

$$P_{K'}(S) \;=\; \frac{P_K(S) \exp[(K' - K)S]}{\sum_S P_K(S) \exp[(K' - K)S]} \tag{2.46}$$

which is a general estimation at any K'. Once the probability is known, all the macroscopic properties and their derivatives can be averaged as a function of K. Locating the critical point therefore becomes just a matter of finding the peak of some characteristic properties (*e.g.* specific heat), task that could be easily accomplished, for instance, by a root finding algorithm applied to the first derivative. The main advantage of the technique explained so far is the possibility of calculating critical properties without needing to exactly simulate at critical point but just being reasonably close to. Ferrenberg and Landau explored the validity of the histogram method by analysing critical behaviour of the three dimensional Ising model[29].

Combining multiple histograms

So far we have used a single histogram to deduce the whole DOS, however it is reasonable to argue that one single simulation is very unlikely to cover all the possible states (see figure 2.2).

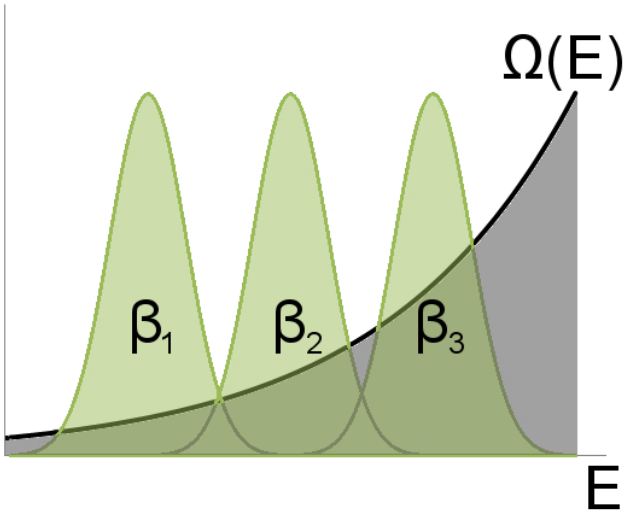

Figure 2.2: *Combination of multiple simulations β_i (with $i = 1, 2, \ldots$) produces an improved estimation of the DOS $\Omega(E)$.*

To combine multiple histograms into the DOS estimation we start from

$$\widetilde{N}(S) = \sum_{n=1}^{R} w_n(S) H_n(S) n_n^{-1} Z(K_n) \exp\left[-K_n S\right] \tag{2.47}$$

where the tilde emphasises the fact of $\widetilde{N}(S)$ being an estimation, the various $H_n(S)$ are the R histograms that we are going to combine and the $w_n(S)$ their relative weight.

The purpose is then to get the best estimation of $N(S)$, *i.e.* with minimum fluctuations depending on the sample $H_n(S)$. Knowing that a single histogram fluctuations are

$$\sigma^2 H_n(S) = \overline{H_n(S)} \tag{2.48}$$

where $\overline{H_n(S)}$ means the expectation value of the histogram which could be related to the probability of eq. (2.41)

$$\overline{H_n(S)} n_n^{-1} = P_{K_n}(S) = \frac{1}{Z(K_n)} N(S) \exp\left[K_n S\right] \tag{2.49}$$

being n_n the length of the simulation. Ferrenberg and Swendsen also report a factor g_n in the (2.48) which depends on the correlation time between successive MC configurations and is equal to 1 if they are independent[31]. Thus the propagation of uncertainty gives us the amplitude of $\widetilde{N}(S)$ fluctuations, and their minimisation with respect of the w_n (upon the restriction of $\sum_{n=1}^{R} w_n = 1$) leads to

$$w_n = \frac{n_n \exp\left[K_n S\right] \frac{1}{Z(K_n)}}{\sum_{m=1}^{R} n_m \exp\left[K_m S\right] \frac{1}{Z(K_m)}} \tag{2.50}$$

$\forall n \subseteq [1, 2, \ldots, R]$.
The estimation of the DOS is therefore

$$\widetilde{N}(S) = \frac{\sum_{n=1}^{R} H_n(S)}{\sum_{m=1}^{R} n_m \exp\left[K_m S\right] \frac{1}{Z(K_m)}}. \tag{2.51}$$

What still needs to be determined in (2.51) is the value of the partition function $Z(K_m)$ corresponding to each one of the R simulations. Moreover, if we put the estimation $\widetilde{N}(S)$ into the equation (2.42)

$$Z(K_m) \simeq \sum_S \widetilde{N}(S) \exp\left[K_m\right] \tag{2.52}$$

we can define $P(S, K) = \widetilde{N}(S) \exp\left[KS\right]$ so that we obtain

$$\begin{cases} P(S,K) = \dfrac{\sum_{n=1}^{R} H_n(S) \exp\left[KS\right]}{\sum_{m=1}^{R} n_m \exp\left[K_m S\right] \frac{1}{Z(K_m)}} \\ \text{where} \\ \sum_S P(S,K) \simeq Z(K). \end{cases} \tag{2.53}$$

The system can be solved by iterative methods in order to have all the $Z(K_m)$, and then it could be extended at any K. Any operator average can therefore be estimated as

$$\begin{cases} \langle A(S)\rangle(K) & = & \sum_S A(S)P(S,K)/z(K) \\ \text{where} & & \\ \sum_S P(S,K) & = & z(K). \end{cases} \tag{2.54}$$

More recently such procedure has been successfully applied to homogeneous mixtures as well[84], with a substantial increase in precision compared with the GE techniques.

2.7.4 Transition Matrix Monte Carlo method

Further improvement based on histogram reweighting arose with the Transition Matrix Monte Carlo method (TMMC)[33]. The general idea is of course to gather as much information as possible from a single simulation in order to improve efficiency. Nevertheless TMMC's main difference from the histogram method is also its main improvement. The latter, in fact, allows to estimate average properties in conditions which are slightly different from the simulation, whereas the data collected from a TMMC run allow the construction of the histogram itself (not only its average value) in such conditions. To achieve this goal the TMMC calculates the probability of observing a system at each state, by means of constructing the so called *transition matrix*. This means that we explore multiple micro-states which are connected with macro-states through a macro-variable, such as energy, particle number, or volume, and we store information about attempted transition between them.

The algorithm we are going to introduce is the one that Errington[27] has implemented into the Metropolis algorithm and successfully applied to liquid-vapour phase equilibria using respectively GC (μVT) or isothermal-isobaric ensemble (NpT). The common Metropolis procedure generates micro-states with a certain probability and then accept for instance the transition from a micro-state s to a micro-state t with the probability

$$P_{acc}(s \to t) = min\left[1, \frac{\pi(t)}{\pi(s)}\right] \tag{2.55}$$

where $\pi(s)$ and $\pi(t)$ are the probabilities of observing the micro-states within the whole phase space[69]. Usually the base value for the ratio $\frac{\pi(t)}{\pi(s)}$ is the factor $\exp[\frac{-\Delta E}{k_B T}]$ where ΔE is the energy difference between the new and the old state, k_B is the Boltzmann constant and T the temperature. Nevertheless every biasing function which

modifies the micro-states generation probability should also be included here in order to guarantee microscopic reversibility.

The probability of observing a certain macro-state is therefore the sum of the probabilities of all micro-states involved

$$\Pi(\mathbf{S}) = \sum_{s \in \mathbf{S}} \pi(s). \tag{2.56}$$

So the method adds another stage in the Metropolis scheme in which a matrix with information about the acceptance rate between the macro-states is collected, namely

$$C(\mathbf{S} \to \mathbf{T}) = C(\mathbf{S} \to \mathbf{T}) + P_{acc}(s \to t) \tag{2.57}$$

and

$$C(\mathbf{S} \to \mathbf{S}) = C(\mathbf{S} \to \mathbf{S}) + 1 - P_{acc}(s \to t) \tag{2.58}$$

for a transition which passes from micro-state $s \in \mathbf{S}$ to $t \in \mathbf{T}$. Probabilities of transitions from a macro-state $\mathbf{S}$ to a macro-state $\mathbf{T}$ are then easily calculated

$$P(\mathbf{S} \to \mathbf{T}) = \frac{C(\mathbf{S} \to \mathbf{T})}{\sum_{\Delta S} C(\mathbf{S} \to \mathbf{S} + \Delta\mathbf{S})}. \tag{2.59}$$

$\mathbf{S} + \Delta\mathbf{S}$ are of course all the possible states which could be reached from $\mathbf{S}$, and $\mathbf{T}$ is one of them. Finally, from the detailed balance we have

$$\Pi(\mathbf{S})P(\mathbf{S} \to \mathbf{T}) = \Pi(\mathbf{T})P(\mathbf{T} \to \mathbf{S}) \tag{2.60}$$

where $\Pi(\mathbf{S})$ and $\Pi(\mathbf{T})$ are the macro-state probabilities we wish to know. In other words we seek a vector $\{\Pi(\mathbf{S}_i) \mid i = 1, N\}$, with N possible states, which is stationary solution of the stochastic matrix $\{P(\mathbf{S}_i \to \mathbf{S}_j) \mid i, j = 1, N\}$. Since the matrix is stochastic, the problem is generally over-specified but, in Errington's scheme, only transitions between adjacent states are permitted, thus producing a three banded matrix which admits a unique solution.

The big difference from the original Metropolis algorithm is that the transition probabilities are not affected by which MC moves are accepted and which are not. For this reason, it is vital to explore the widest phase space possible, though this could mean probabilities which differ by many orders of magnitude. To improve the sampling of unfavourable states, a biasing function is applied in the micro-state generation[6]

$$\eta(\mathbf{S}) = -\ln \Pi(\mathbf{S}). \tag{2.61}$$

Since the observing probability $\Pi(\mathbf{S})$ is not known *a priori*, the biasing function is periodically updated as the simulation runs. The biasing effect is then obtained by modifying the acceptance rate, whereas the values collected into the *transition matrix* remain the unbiased ones. For this reason we do not need to discard previous data when the function is updated.

The specific implementation of the algorithm into GC or isothermal-isobaric ensemble is clearly explained in [27]. Nevertheless the choice of the variable used to define the macro-states need to be referred. GC ensemble allows energy and particle number to fluctuate, whereas isothermal-isobaric does it with energy and volume. According to the variable used for defining the macro-states it is possible to reweight the probability distribution at different conditions, namely temperature if the states are classified by energy, chemical potential if we choose particle number, or pressure if they are classified by the logarithm of the volume.

$$\ln \Pi_{\mu}(N) = \ln \Pi_{\mu_0}(N) + \beta(\mu - \mu_0)N \tag{2.62}$$

$$\ln \Pi_{p}(\ln V) = \ln \Pi_{p_0}(\ln V) - \beta(p - p_0)V \tag{2.63}$$

In order to perform temperature re-weighting two variable classification would be needed, thus it undoubtedly increases the amount of storage data required.

$$\begin{aligned} \ln \Pi_{\mu,\beta}(N, E) &= \ln \Pi_{\mu_0,\beta_0}(N, E) + \ \ldots \\ &\ldots \ -(\beta - \beta_0)E + (\beta\mu - \beta_0\mu_0)N. \end{aligned} \tag{2.64}$$

Moreover the algorithm would need both the biased sampling presented above as well as the visited states approach to properly sample the energies [27].

Chapter 3

Hydrogen molecules interacting with CNTs

A comparative analysis of interaction potentials, classified according to the parametrization method, namely Lorentz-Berthelot rules, semi-empirical or *ab initio* calculations, found their energy depths to scale, respectively, to *ca.*$30K$, *ca.*$40K$, and *ca.*$60K$. We draw the PESs for a hydrogen probe molecule inside a CNT: it is shown that the adsorption energy increases with the hard radius of the interaction potential and decreases as the CNT pore enlarges. This is valid just for low-medium pressures, when hydrogen repulsions are negligible. If not, adsorption is driven by H_2–H_2 hard radius despite all other parameters. MC simulations, following the GE in high density conditions, confirm that the thermodynamic equilibrium of an ordered-disordered phase transition show no changes throughout any of the studied potentials. We also analyse, in the GC ensemble, the geometric and structural characteristics of square lattice bundles of Single Walled Nano Tubes (SWNTs) with regard to their influence on adsorption storage. To do so, we develop a method for independently simulate inner or outer adsorption in infinitely long nanotube lattice systems. Our results suggest a pressure range for convenient H_2 storage and enlighten the influence of CNT size on adsorption performance. In addition, larger CNTs are capable to host further hydrogen layers, but only at very high pressures.

3.1 Adsorption theory

Adsorption means the interaction of fluid molecules (either gas or liquid) with a surface of a solid material. This phenomenon implies that, some of the fluid molecules are not free to flow, but remain close to the surface. It is sometimes classified as chemisorption or physiorption according to whether such interaction involve or not the breaking of bonds and the formation of new ones. In empirical terms it is possible to say that if the binding energy is sufficiently high ($> 0.5eV$) chemisorption is probably the preferred mechanism, while with low interaction energies is should be physiorption the one taking place.

Langmuir, in 1918, proposed a model for mono-layer adsorption on flat surfaces[56], in absence of interactions between adsorbed molecules. Considering a countable number of sites on the surface (so that is possible to define a concentration), he described the process as it was a chemical equilibrium

$$A_{free} \quad + \quad S \quad \rightleftharpoons \quad A_{adsorbed}$$

between free molecules A_{free} and adsorption sites S which obey to a strict proportion 1:1 (*i.e.* one molecule for each site), which produces adsorbed molecules $A_{adsorbed}$. Consequently, at constant temperature, the equilibrium will be

$$K = \frac{[A_{adsorbed}]}{p_A[S]} = \frac{\xi}{p_A(1-\xi)}$$

where ξ is the fraction of occupied adsorption sites and p_A is the partial pressure of the gas A. This leads to the Langmuir isotherm

$$\xi = \frac{Kp_A}{1 + Kp_A}$$

which permits to interpret the progress of the coverage as function of the partial pressure of A.

BET (Brunauer Emmett and Teller[7]) theory applies the Langmuir model to multiple layers. They assumed a constant binding energy for the layers beyond the first. The result isotherm is an S-shaped curve as function of the applied pressure p

$$v = \frac{v_m cp}{(p_0 - p)[1 + (c-1)(p/p_0)]}$$

where v is the volume of gas adsorbed, p_0 the saturation pressure, and the constant

$$c = \exp\left(\frac{E_1 - E_L}{RT}\right)$$

depends on the energy difference between the heat of adsorption of, respectively, the first layer (E_1) and the others (E_L). The maximum volume adsorbed on a complete mono-layer v_m is related to the total area available and therefore is frequently used for experimental estimation of the area of CNT samples.

It should be noticed that in BET formulation all interactions between gas molecules are included into the constant and not considered explicitly.

The simplest way to simulate adsorption with MC is by means of GC ensemble, where the simulated box, containing the substrate, is put in equilibrium with an ideal gas at fixed chemical potential. The algorithm then will try to insert as much molecules as possible until they reach the set chemical potential. More details of such procedure are explained in section 3.3.

3.2 Interaction potentials

In 1980, Wang S. *et al.* used a 12-6 LJ type potential for studying the interaction of a hydrogen molecule with a graphite system[109]. They numerically solved the Schrödinger equation for the bound states of a single *para*-H_2 molecule. Since the study was carried out at low temperature, the hypothesis of hydrogen being in *para* is justified. This means that the interaction potential should be spherically averaged in order to take into account the isotropic behaviour of the spin isomer.

Their potential was expressed as an expansion over a complete set of Legendre polynomials

$$V(R,\theta) = \sum_{l=0}^{\infty} V_{2l}(R) P_{2l}(\cos\theta)$$

which they truncated to the second term assuming a LJ form with empirical anisotropy parameters:

$$\begin{aligned} V(R,\theta) &= V_0(R) + V_2(R) P_2(\cos\theta) \\ &= 4\varepsilon\left[(\sigma/R)^{12} - (\sigma/R)^6\right] + 4\varepsilon\left[0.224(\sigma/R)^{12} - 0.177(\sigma/R)^6\right] P_2(\cos\theta) \end{aligned}$$

By comparing the eigenvalues, calculated according to laterally averaged substrate potential, with energy spectra experiments of H_2 adsorbed on graphite, they obtained parameters $\sigma_{CH} = 0.297$nm and $\varepsilon_{CH} = 42.75K$ which gave a reasonably good agreement. They also identify an ordered-disordered phase transition at 1/3 coverage (0.0641Å^{-2} density) in agreement with experimental works cited. Very interesting is the fact of such transition being observed in both cases whether the potential is

laterally averaged or not. Authors justify this result saying that hydrogen interactions are strong enough to cause the formation of a two dimensional lattice, even without the aid of the substrate. At room temperature however, the presence of *ortho*-hydrogen cannot be neglected but, probably with the purpose of simplicity and computational time spare, most simulations, especially MC, keep using isotropic interactions. More recently, in 2007, Aga R. *et al.* used the isotropic part of Wang potential for the MC part of a combined study of hydrogen adsorbed in graphite which involved *ab initio* calculations as well[1]. From the latter they estimated the adsorption energy of a molecule into a slit pore and found a difference of $\sim 0.02eV$ between that molecule lying in a plane parallel to the graphitic one or in a plane orthogonal to it. Nevertheless, they are dealing with high energy contributions due to the interlayer expansion needed for hosting H_2 molecules, therefore such difference is not so relevant in the overall balance and they actually use isotropic potential in their MC simulations. Path Integral (PI) procedure was also applied in order to take quantum effects into account.

A stronger exp-6 form of the LJ potential was also taken as an upper limit reference

$$V(r) = A\exp(-\alpha r) + C_6 r^{-6}.$$

It was developed by Patchkovskii *et al.* in 2005 by fitting quantum calculations of a hydrogen-coronene system [83]. Since an exponential and a negative r^{-6} function are summed, the potential reach a maximum at low values of r and then tends towards $-\infty$ as r approaches zero. This is not convenient in Grand Canonical Monte Carlo (GCMC) simulations, because it creates small but deep potential wells, close to the atoms involved. It can be easily solved if the minimum interatomic distance (i.e. the distance at which energy is automatically set to infinite) is kept larger than the distance at which corresponds the maximum potential. Of course this method becomes more and more complex as more different species with different potential parameters are involved in the simulation. As demonstrated by the authors, such potential behaves quite well in a H_2-*benzene* system. However the minimum energy distance, and the energy itself, decreases as the system comprises more carbon atoms. Such effect is clearly observed in both potentials used by Aga *er al.*. Their search for the most favourable interlayer distance revealed however some differences between calculated and simulated results which can only be partially explained by the formulation of the potentials. In fact *ab initio* calculation showed an energy minimum at 60-70% expansion of the base distance (3.3Å) while in GCMC simulations both potentials had maximum adsorption at interlayer distance between 75% and 80% expansion[1]. A contribution to such differences can probably arise from the presence of multiple H_2 molecules which in *ab initio* calulations are not taken into account. Such multiple

hydrogen molecules were interpreted through the Silvera-Goldman potential [98], an isotropic semiempirical force field developed by fitting solid state data:

$$\exp(-\alpha-\beta r-\gamma r^2)-\left(\frac{C_6}{r^6}+\frac{C_8}{r^8}+\frac{C_{10}}{r^{10}}\right)f_c(r)+\left(\frac{C_9}{r^9}\right)f_c(r)$$

$$\text{with}\begin{cases} f_c(r)=\exp\left[-\left(\frac{1.28r_m}{r}-1\right)^2\right] & \text{if} \quad r<1.28r_m \\ f_c(r)=1 & \text{if} \quad r>1.28r_m \end{cases}$$

being r_m the position of the minimum of the potential well. It has been widely used for studying hydrogen in particular at low temperature or high pressure[102, 111, 10]. In 2011 Singh *et al.* carried out a GCMC study on carbon foams[99]: the model and the potentials employed were exactly the same of Aga[1] but quantum corrections were included through FH variational treatment[32], in which a quantum particle of mass m is characterized by a Gaussian spread with a thermal quantum width Λ (the termal De Broglie wavelength, see equation 2.23), around the particle center of mass (the application of such correction is explained in section 3.3, equation 3.6).

It is not clear, nevertheless, if they applied this treatment to all potentials or, most probably, to the 12-6 LJ only. Moreover, having good LJ parameters which efficiently simulate carbon or hydrogen properties, it is possible to get an expression for the mixed interactions by means, for example, of the Lorentz-Berthelot mixing rules (arithmetic mean of σ and geometric mean of ε).This imposes a careful choice of the C and H_2 parameters. Common parameters for carbon atoms in graphitic structures are the ones proposed by Steele[103]: $\sigma_{CC}=0.340\text{nm}$ and $\varepsilon_{CC}=28.0K$.

Furthermore they developed the 10-4-3 Steele potential which simulate a wall made of infinite graphitic sheets; its LJ parameters are calculated by the Lorentz-Berthelot mixing rules.

$$V(z)=2\pi\rho_s\varepsilon_{CH}\sigma_{CH}^2\Delta\left[\frac{2}{5}\left(\frac{\sigma_{CH}}{z}\right)^{10}-\left(\frac{\sigma_{CH}}{z}\right)^4-\frac{\sigma_{CH}^4}{3\Delta(0.61\Delta+z)^3}\right]$$

with $\rho_s=114\text{nm}^{-3}$ is the number of carbon atoms per unit volume in graphite and $\Delta=0.335\text{nm}$ is the separation between any two of the infinite stacked graphitic planes.

Nguyen *et al.* argued that curved carbon surface should have a stronger attraction, and calculated an increase factor $X_\varepsilon=1.134$ in order to take this effect into account[76]. Frankland and Brenner, who simulated Raman shift of isolated H_2 inside CNTs, obtained for carbon $\sigma_{CC}=0.335\text{nm}$ and $\varepsilon_{CC}=51.02K$[34], certainly surprising because of the extremely deep potential well, much deeper than the one used by Steele in graphite models[103]. Besides, they calculated parameters for hydrogen, either

in the fundamental vibrational state ($\sigma_{HH} = 0.281$nm; $\varepsilon_{HH} = 15.0K$) and the first excited one ($\sigma_{HH} = 0.284$nm; $\varepsilon_{HH} = 15.6K$). They clearly used a 2-centres model as well as Lorentz-Berthelot mixing rules.

Based on the above data, Nguyen *et al.* proposed a new value for the potential well depth when C and H_2 are involved: $\varepsilon_{CH}^{flat} = 37.01K$ for planar carbon sheets, which it turns to be $\varepsilon_{CH}^{curved} = X_\varepsilon \varepsilon_{CH}^{flat} = 41.97K$ for nanotubes and curved surfaces[75]. Their work, which involved GCMC simulations in either FH or PI approach, aim to predict experimental results using LJ parameters estimated by independent semiempirical works or *ab initio* calculations. Assuming Levesque's parameters for H_2[60], which provide excellent agreement between simulated bulk isotherms and corresponding reference data[52], authors tested LJ potentials found in literature[109, 34] using LB mixing rules for deducing the missing parameters. They explored two slit-like pore models, namely Graphitized carbon black and Molecular Sieve Carbon 3Å (MSC3A), and an Atomistic Model of the Activated Carbon Fiber ACF-15, produced by Hybrid Reverse MC simulation. The importance of the latter is that its PSD is not obtained from isotherm fits (as are the other two systems) and thus it is independent of the potential strength between the carbon and the probing molecule. The adjusted parameters, as well as Frankland[34]'s and Wang[109]'s, reproduced quite well the adsorption reference data and calculated energy minimum, while it has been reported a significative understimation when using Steele[103]'s. The hypothesis of weaker potential is also roughly consistent with the observed overprediction of experimental adsorption isotherms of heavier gases by the slit-pore model using the PSD extracted from the experimental H_2 adsorption isotherm. Authors also claimed that this problem has been overcome using their new H_2 parameters, but maintaining the old ones when calculating mixed potential for heavier gases (*e.g.* CO_2,Ar,CH_4).

Concerning hydrogen potential the situation is more complicated because of the possibility of the molecule to have anisotropic behaviour. Buch V.[8] developed an isotropic LJ potential for *para*-H_2 which was completed by an electric quadrupole-quadrupole pair interaction in order to take anisotropy into account in the case of *ortho*-H_2. The parameters $\sigma_{HH} = 0.296$nm and $\varepsilon_{HH} = 34.2K$ had been previously adjusted to obtain better agreement with the mean potential energies of the H_2-*cluster*, calculated by means of the more accurate Silvera-Goldman potential[98]. Hence, applying LB mixing rules we have: $\sigma_{CH} = 0.318$nm and $\varepsilon_{CH} = 30.945K$. Such parameters are very close to the ones used by Darkrim F. *et al.*[19] $\sigma_{CH} = 0.3179$nm and $\varepsilon_{CH} = 32.056K$ calculated by the same mixing rules. The authors also conclude that, for hydrogen at temperature above $20K$, the PI approach is not needed but FH quantum correction[32]

is sufficient. Moreover, just like other authors previously suggested[8, 74], they only include anisotropy through the application of quadrupole-quadrupole interactions, but this does not affect interactions between hydrogen molecules and carbon atoms which remain one-centre. Despite of these considerations, Cracknell R. *et al.* studied adsorption on graphitic nanofibers, proposing a $12-6$ LJ potential with a 2-centre hydrogen molecular model with fixed bond length[17]. Due to the lack of reference parameters for such kind of approach, they identified some criteria to deduce them from one-centre models: the new hard sphere diameter $\sigma_{HH} = 0.259$nm was assumed to be reduced by the half of the *H*-*H* bond length; the well depth $\varepsilon_{HH} = 12.5K$ has been determined so as the 2-centres model would match the isosteric heat of adsorption on graphite surface at $298K$ of the spherical model. Although they concluded that the 2-centres model makes little difference compared to the spherical one, their LJ parameters are not in a good agreement with Frankland and Brenner's[34] (cited above). It should be noted that the above considerations about the potential strength are not sufficient to explain this mismatch because a significant difference is found in the hard radius as well. Kuchta *et al.* estimated the energy of the fundamental and first excited rotational state of a hydrogen molecule interacting with a graphene sheet[53]. The energy difference between the two lower states, $\sim 175K$ $(1.5kJ/mol)$ is close enough to the theoretical value

$$E_{j=1} = \frac{\hbar^2}{2I} j(j+1) = 177.17K \qquad (1.473kJ/mol)$$

of the rigid rotor H_2 model with 0.074nm bond length. However, what undoubtedly constitutes a novelty is the first excited state loss of degeneracy: one of the three states, which has the same or very similar symmetry as the graphene plane, shows higher energy, namely lower well depth and larger hard radius than the other two. They studied how structural modifications (*e.g.* hole drilling) or chemical substitution (*e.g.* inducing electrostatic interactions between hydrogen and carbon) would affect the adsorption mechanism. They also analysed[54] with MC simulations the influence of the H_2-slit wall interaction strength by testing several models with increasing well depth[105, 67]. Two hypotetical models with enhanced binding energy (up to $15kJ/mol$) were also included. Results have shown that the higher ones, although they actually increase storage, decrease delivery efficiency at lower temperatures ($77K$). Nevertheless, at room temperature, such strong interactions would improve capacity and delivery as well. It should be said that such conclusions imply conditions of multi-layer formation (*i.e.* pore size 0.8nm or larger). The smaller size enhances capacity only at lower pressures but delivery is compromised, and this is even more drastic with stronger potentials. Sun *et al.*[105] emphasized the behaviour of DFT methods

when calculating PES by analysing either the equilibrium distance and the slope of the repulsion part of the potential in comparizon with MP2 calculations with a large basis set (aug-cc-pVTZ)[28]. Local Density Approximations reproduce quite well the slope but significantly underestimate equilibrium distance; on the other hand, functionals with gradient corrections (B3LYP and PW91) fail in reproducing either the distance (overestimated) and the adsorption well which is severely shallow. In order to improve the fitting of the above cited calculations[28], authors proposed two formulas which would produce better agreement than the common 12-6 LJ: an exp-6-8-10 analogous to the Silvera-Goldman potential[98] (see above) but used for H_2–C interactions, and an exp-6 of the type used by Patchkovskii[83]. Both formulas have been optimized to fit Ferre-Vilaplana[28] results on a hydrogen-coronene system. A classic 12-6 LJ formula has been fitted as well proving to be very sensitive to the set of data used for the parametrization: fitting with long range data produces stronger repulsion while using short range ones makes deeper potential well. Neither equilibrium values are sufficient (shallow well) to have a good fit. Despite the need of using a spread set of data to properly fit the potential, LJ classic formula still has the advantage of being simple, easy to handle (a linear combination of 12-6 LJ is still a 12-6 LJ) and not very expensive in terms of computer resources. For these reasons, it is worth taking a deeper look at the fitting. The reported energy $4\varepsilon_{CH} = 0.0221406eV$ is extremely higher than other LJ potentials obtained by matching scattering data[109, 67] or by LB mixing rules[103, 19]. Nevertheless the hard radius $\sigma_{CH} = 0.302463$nm stays in the range of the previously reported works. So far, for spherical hydrogen models, energies ε_{CH} derived from mixing rules are usually $> 30K$,whereas from scattering experiments they are $> 40K$. All these have therefore a weaker adsorption energy than any of the cited *ab initio* interpolations[1, 105] where the well depth of the two body potential is $> 60K$. Sun *et al.* actually reported adsorption energies on graphene ($0.0748eV$)[105] which are slightly higher than reported experimental values[67]; such values however do not take into account the interactions between hydrogens, therefore, in high pressure conditions, overestimation is fully expected.

3.3 Computational model

GCMC simulations are widely used for simulating adsorption because the (μVT) ensemble resembles a porous material in equilibrium with a gas reservoir[78]. Gibbs Ensemble Monte Carlo (GEMC) is also able to study such a system[81], but it simulates both the condensed (or adsorbed) phase as well as the gas one. Since in the latter case

simulations are carried out at constant number of particles, volume and temperature (NVT), such approach registers a pressure decrease in the gas phase due to the occurrence of adsorption. Instead, in GCMC, the reservoir bath is not simulated but assumed ideal at the fixed chemical potential. In both cases density fluctuations are taken into account through the insertion or deletion trial which either creates or removes molecules into the simulation box; in the GEMC the trial consists in swapping a molecule from the box containing the free gas to the other where there is the adsorbent, but the mechanism is exactly the same. The insertion tries to put a new molecule into the box either with uniform probability density or following a bias function, deletion instead randomly selects and removes one of the molecules of the system. Both moves are then accepted or rejected according to the standard MC probability[69]

$$P_{\text{accept}} = \min[1, K \exp(-\beta[U_{\text{new}} - U_{\text{old}}])] \tag{3.1}$$

where $\beta = 1/k_B T$, being T the temperature, k_B the Boltzmann constant, and U_{new} and U_{old} are respectively the energies of the new configuration and of the old one; the factor K takes into account the change in molecule number

$$K(N \to N \pm 1) = \left[\frac{V}{\Lambda^3} e^{\beta\mu}\right]^{\pm 1} \frac{N \pm 1!}{N!}.$$

We simulate infinitely long SWNTs in order not to deal with their loose ends. Accordingly, the box length along the Z axis is made to have exactly the same length of the nanotube, including the space needed to extend the bonds and connect to the next replica. Each simulated nanotube contains 5 base unit cell rings, meaning a total of 380 atoms for the (19,0) and 320 for the (16,0). The box length is therefore equal to 15 times the bond length. Just one SWNT is actually simulated and periodic boundary conditions make it and its replica being organised in square lattice bundles. Spacing the lattice more than the cut off range, fixed at 9.5Å, is a way to simulate an isolated SWNT, because no molecules in the box would therefore sense any of its replica. Since the nanotube is not allowed to move and its energy is fixed, we choose to set it to zero in order to have a clearer view on the energy contribution of hydrogen molecules. All simulations run on *towhee* software for Monte Carlo Complex Chemical Systems (MCCCS)[66].

Besides simulations, classical analytical calculations are performed, in order to plot the PES associated to the CNT system with each one of the studied pair potentials. We first verified that extending the (19,0) SWNT up to 19 unit cell rings (1444 atoms), changes the inner potential only by 1-2%. The probe hydrogen molecule lies in a plane that cuts the CNT almost at the middle of its length, through the centre of carbon

rings. Bond length is set to 1.418Å. The biggest nanotube used in our work, the (19,0) has been chosen because it has exactly the same diameter of the (16,5) and this allowed a flawless comparison which confirmed that the properties under study are not affected by the nanotube chirality (data are not reported).

We study three pair potentials obtained in different ways: by mixing homogeneous potentials through Lorentz-Berthelot mixing rules[8][104]; by fitting experimental spectra[109]; from *ab initio* calculations[105]. The latter comes from a 12-6 LJ fitting of high level *ab initio* results previously obtained by Ferre-Vilaplana [28]. This is just a starting point; the authors in fact developed an empirical, non LJ, form which suits the results even better. Since such differences are still less significant than those between the other potentials of our work, we believe this level of detail is unnecessary. The second potential we use is a semi-empirical one, obtained by fitting experimental spectra[109]. In fact, the authors have numerically solved the Schrödinger equation for a molecule of isotropic *para-*H_2 interacting with a graphite surface through a LJ potential. Thus they found the eigenvalues as a function of σ and ε. Comparing the lowest levels with experimental energies from scattering spectra they calculated the values reported in table 3.1. The individual homogeneous potentials mixed by means of Lorentz-Berthelot rules came as well from semi-empirical fittings of bulk properties. Buch *et al.*[8] approximated with a LJ type the well known Silvera-Goldman potential[98], which successfully matched experimental and calculated bulk properties of both solid and gas hydrogen. On the other side Steele parameters also behave very well on graphitic systems[104]. In addition, other potentials were investigated, but they were quite similar in well depth and hard radius to the reported ones, accordingly to the method they were developed from[19][83]. For this reason those potentials are not reported here. All the three chosen examples belong to the 12-6 LJ (LJ) class:

$$V_{\mathrm{LJ}}(r) = 4\varepsilon_{\mathrm{XY}}[(\sigma_{\mathrm{XY}}/r)^{12} - (\sigma_{\mathrm{XY}}/r)^{6}] \tag{3.2}$$

where X and Y are the interacting particles (C and H in this case) and parameters $\varepsilon_{\mathrm{XY}}$ and σ_{XY} of the three potentials are presented in table 3.1. They imply an isotropic, one centre, hydrogen molecular model and have been paired with the H_2–H_2 potential also reported.

For comparative purposes a potential set for anisotropic interactions has been also developed. As mentioned above, carbon-carbon interactions are set to zero, since they stay fixed along the whole simulation, and hydrogen interactions are taken from literature[17]. The mixed LJ parameters generated by Lorentz-Berthelot rules seem to be too weak, compared with the one centre models, without regard to the orientation of the diatomic molecule. We then choose to optimise the mixed parameters by matching,

Table 3.1: *Isotropic potentials.*

type	σ/Å	ε/K	reference
1 - Lorentz-Berthelot	3.18	30.95	[8][104]
2 - semi-empirical	2.97	42.75	[109]
3 - *ab initio* calculations	3.02	64.23	[105]
H_2–H_2	2.96	34.2	[8]

for the most favourable orientation, the classical PES inside a (16,0) zig-zag SWNT, with the one generated using the isotropic potential from [109] (see table 3.1). The resulted parameters are shown in table 3.2.

Table 3.2: *Anisotropic interaction potentials.*

type	σ/Å	ε/K	reference
C–H	2.93	22.5	[59]
H–H	2.59	12.5	[17]

Both models, isotropic and anisotropic, only consider translational degrees of freedom within the simulation. From statistical thermodynamics we have therefore:

$$\mu = -k_B T \ln\left(\frac{Z}{N}\right) \tag{3.3}$$

where μ is the chemical potential, k_B the Boltzmann constant, T the temperature and Z the microcanonical (NVE) partition function. If only translations are considered, Z can be approximated as follows

$$\frac{Z}{N} \approx \frac{V_m}{\Lambda^3} \tag{3.4}$$

being V_m the molecular volume and Λ the thermal De Broglie wavelength of the considered molecule at the chosen temperature. For ideal gases it will give

$$\mu \approx k_B T \ln\left(\frac{P\Lambda^3}{k_B T}\right) \tag{3.5}$$

which has been used in our simulations to calculate the corresponding pressure to the chosen chemical potential. Without assuming ideality, it could be possible to achieve the same goal by previously drawing a chemical potential vs pressure plot through isothermal-isobaric NPT simulations. We choose not to do so, because we are studying

the effect of small variations in the interaction potentials and it is therefore undesirable to introduce new fluctuations from other simulations.

In some simulations, namely the ones where the purpose was to compare with experimental results, interaction potentials include FH quantum corrections[32]:

$$V_{\text{corrected}}(r) = V_{\text{LJ}}(r) + \frac{\beta\hbar^2}{24m_R}\left(\ddot{V}_{\text{LJ}}(r) + \frac{2}{r}\dot{V}_{\text{LJ}}(r)\right) \tag{3.6}$$

where $V_{\text{LJ}}(r)$ is the standard LJ potential (eq. 3.2), $\dot{V}_{\text{LJ}}(r)$ and $\ddot{V}_{\text{LJ}}(r)$ are the first and the second derivatives with respect to r, $\beta = 1/k_BT$ and m_R is the reduced mass associated to the pair of interacting particles. Since they are kept at fixed position, we calculate m_R as if the carbon atoms had infinite mass; so we have $m_R = m_{H_2}$ for one centre models and $m_R = m_{H_2}/2$ for the explicit ones.

Most simulations equilibrate for 3x10^6 steps, while the production runs for 10^7 steps.

3.4 Results

Mixed pair potentials for theoretical simulation can mainly be obtained in three ways: mixing the parameters of each atom's interactions with its identical ones; fitting experimental spectra which involve the interaction between the two species; or performing *ab initio* calculations. The first is widely used in literature, *e.g.* in the Universal Force Field[87], present in *towhee* package[66], and do not need any further parametrization. Its main strength is the fact that individual parameters are supported by lots of experimental and theoretical data, but it contains a certain degree of arbitrariness because of the choice of the mixing rules. The second method instead, as stated above, cannot rely on such a broad data set, nevertheless it has the advantage of a direct parametrization of the interactions. The *ab initio* parametrization clearly reckons on the strictness of the theoretical approach. The characteristic that stands out from the comparison is undoubtedly the well depth scaling from *ca.*$30K$ in the first type up to more than $60K$ in the latter (see table 3.1). The example potential types 1, 2 and 3 of table 3.1 will be further denoted as LB-30, Wang-40 and Sun-60, respectively.

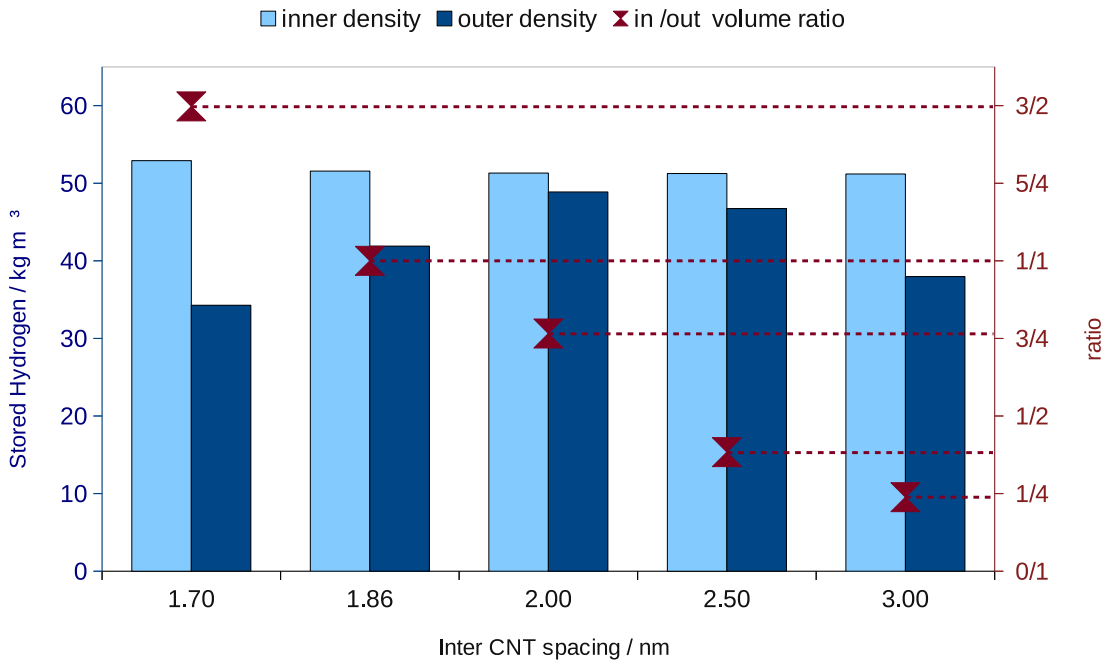

Figure 3.1: *Inner and outer density around (19,0) SWNT square bundles with different spacing, simulated by GCMC at* $62.5atm$ *and* $75K$ *– the in/out volume ratio, also reported for each case, enlighten the increasing of the outer space with the bundle swelling.*

3.4.1 Simulating inside and outside SWNTs independently

The infinitely wide nanotube lattice comprises just two types of pores: the intra-CNT, or inner, which only depends on the nanotube radius and inter-CNT, or outer, which also depends on the lattice parameters. In order to simulate the two environments independently, we seek a way to let molecules be inserted only into the one we chose. This target could be eventually achieved using a complex structure of external force fields simulating hard walls and balls and which actually occupy all the space we are not interested in. However, within the *towhee* package, there is a tool, suitable for porous materials, which maps the potential energy of inserting a certain molecule in order to bias further insertions[66][101]. This task is only computed at the very beginning, and the map is saved and used for the whole simulation. The method we developed consists in setting all the insertion probabilities relative to the forbidden space to zero, namely rising its energy to infinite. After a few test simulations with different resolution maps, the chosen type has been a 20x20x10 map, which means that the whole space is divided into small blocks, namely 20 along the axis X and

Y and 10 along the axis of the nanotube (Z). Since simulation boxes sizes were in the order of *ca.*20-30Å in each dimension, the blocks are *ca.*1Å large in X and Y and *ca.*2-3Å long. Such method has been tested by running a series of simulations at increasing chemical potential (which varies linearly with the logarithm of pressure) and then comparing the obtained adsorption isotherm ($77K$) with the results of the unconfined system. It was observed that the latter is indeed equal to the sum of the inner and outer contribution run separately.

Although larger pores certainly imply more room for hosting hydrogen, the pressure needed for complete filling grows higher. The consequence is that, at fixed pressure, the outer density reaches a maximum at a certain value of inter-CNT spacing, but then, instead of maintaining that limit capacity, it starts to decrease asymptotically to the pure gas density. GCMC simulations of squared lattice nanotubes with different distances confirmed such statement, in conditions of low temperature ($75K$) and high pressure (chemical potential $\mu = -315.6K$ which correspond to *ca.*62.5atm). Results are shown in figure 3.1 which also reports the inner/outer space ratio for each simulation. It can be also perceived how small is the influence on inner adsorption exerted by the bundle structure. Because of this low variance we focus mainly on inner adsorption as a reference value, not having yet enough information about experimental bundle structure and outer pore size[51].

3.4.2 Classical PES calculations

What happens when a molecule is interacting with the inner surface of a SWNT, being such interaction almost independent of external environment factors such as bundle structure or lattice distance? Figure 3.3 represents the radial section of the PES of a probe hydrogen molecule within an infinite SWNT (or at least longer than the cut off range) for the three C–H_2 example potential of table 3.1. Notice the effect of the smaller CNT which deepens the energy well without affecting the repulsive part of the plot. By scaling the energy in ε units, thus making all the plots independent of such parameter, we shall focus on the effect of σ. It can be seen that the potential well depth, unlike the two-body systems, has an explicit dependence on σ_{CH}. This result can be explained invoking the lower slope of the LJ pair potential plot with higher σ, nevertheless such issue does not belong to the purpose of this text. We just mean to emphasise the deviations which occur in the PES even with small variations of σ_{CH}. The position of the minimum is found approximately equal to σ_{CH} for all the potentials, with little differences whether the CNT was (16,0) or (19,0). The latter,

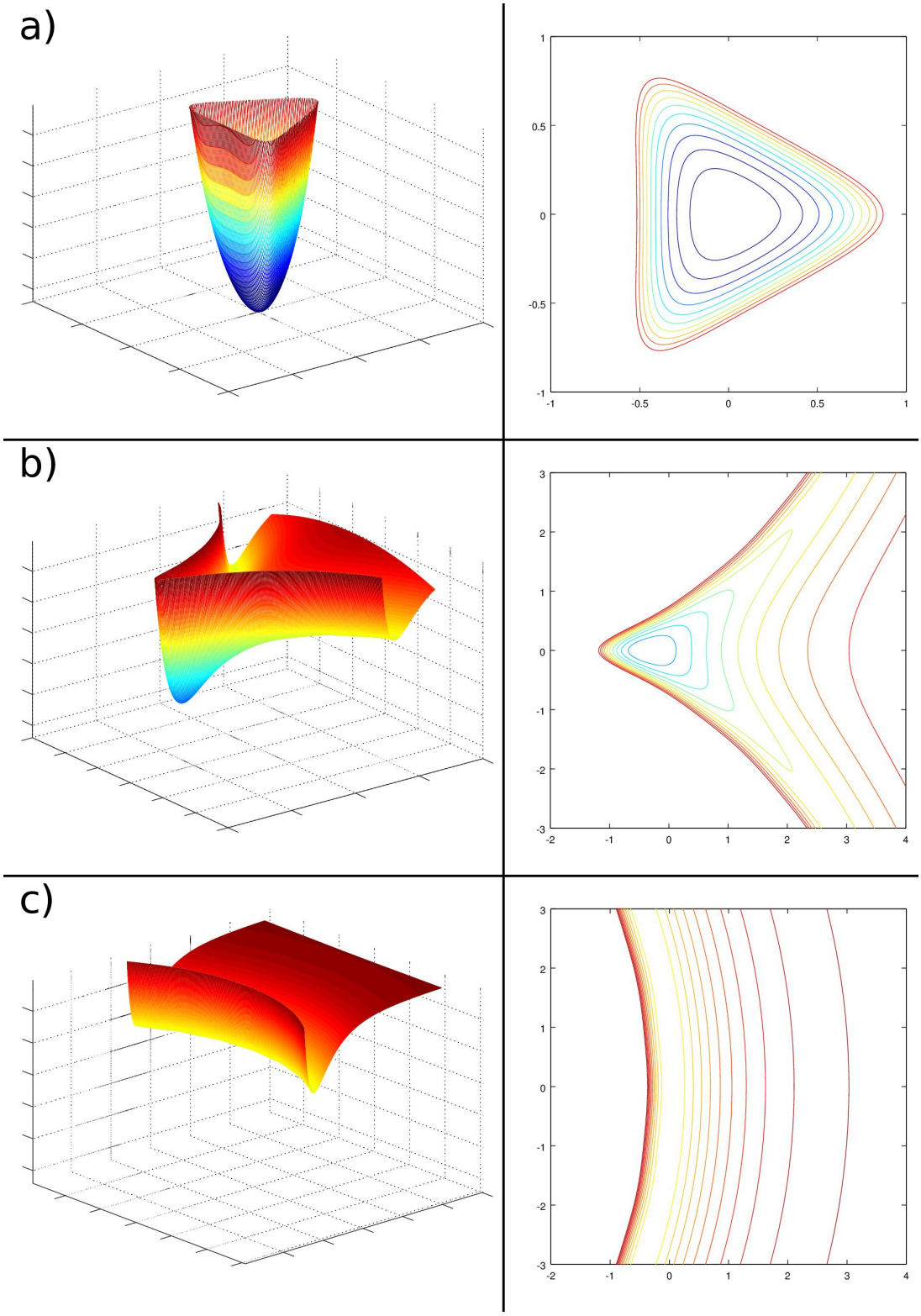

Figure 3.2: *Shape and energy profiles for different surfaces of a* $(16, 0)$ *SWNT bundle: a) inter-tube pore; b) groove pore; c) external bundle surface. Length are in* Å *and the colour scale is about* $\sim 30\varepsilon$.

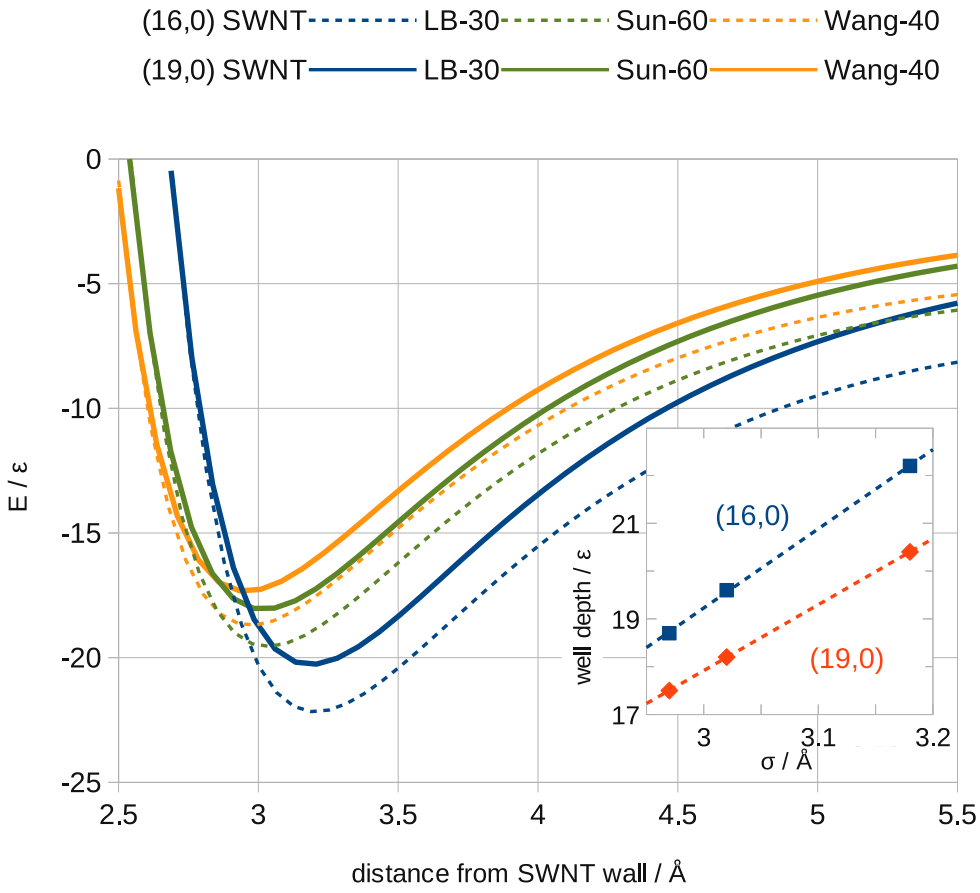

Figure 3.3: *Inside SWNT total energy plot in multiples of $\varepsilon_{\mathrm{CH}}$ of the three C-H potentials of table 3.1 – in the inset: linear correlation between the energy well dept and σ_{CH}.*

actually, seems slightly farther but the difference stays within the error. What emerges from the comparison of the total potential well depth (in units of ε) with the σ_{CH} used for each plot, is that there is perfect linearity ($R^2 > 0.999$) between the two variables (see the inset of figure 3.3). However the larger CNT shows a lower increase per unit of σ. Such deviations do not affect only the small part of the particles which lie in the repulsion region, but also the ones which are in the energy well or seeking it.

PES environment from outside the CNT in bundle structure are presented in figure 3.2.

3.4.3 GCMC adsorption simulations

The value of $\varepsilon_{\mathrm{CH}}$ strongly affects adsorption capability at lower pressure conditions, that is in non repulsive conditions. The, GCMC method enlightens how the simulated adsorption capacity could be severely different according to the interaction potential used. Table 3.3, in fact, compares the H_2 inner storage of a (19,0) SWNT simulated by GCMC using the three example potentials. The $\%wt$ values are calculated as hydrogen-carbon weight ratio

$$\%wt = \frac{\mathbf{m}_{H_2}}{\mathbf{m}_{\mathrm{CNT}}} \langle \mathbf{n}_{H_2} \rangle$$

where $\mathbf{m}_{H_2} = 2.0158\mathrm{u}$ is hydrogen molecular mass and $\mathbf{m}_{\mathrm{CNT}} = 380 \cdot m_C = 4564.18\mathrm{u}$ is the total mass of the simulated SWNT. The confinement method described above is also applied. It is shown that low pressures (simulated at $3.76\mathrm{x}10^{-3}$atm) enhance the difference in uptake capability, so that the ASH of Sun-60 potential [105] ($\varepsilon_{\mathrm{CH}} \approx 60K$) is about 1.50%wt while the others are far lower, and even between them there is a 7:2 ratio. At mid and high pressures (3.77atm and 3770atm respectively) the consequences of different $\varepsilon_{\mathrm{CH}}$ are progressively less visible.

Table 3.3: *Amount of stored hydrogen (%wt.) inside a (19,0) SWNT at* $77K$.

	LB-30	Wang-40	Sun-60
high pressure	3.52%	3.82%	3.98%
mid pressure	1.76%	2.15%	2.84%
low pressure	0.0120%	0.0422%	1.50%

We then plot adsorption isotherms of a (16,0) SWNT inner pore, obtained varying force field parameters one at time. Simulations which we denote as "realistic" use values from table 3.2, relative to the anisotropic H_2 model, and include FH quantum corrections[32]. Keeping all the other parameters fixed, we almost double the well depth (up to *ca.*$45K$) and observed that the pore surface shows significant adsorption even at a chemical potential $500K$ lower than the unmodified case. With the same procedure we raise the hydrogen's repulsion hard radius σ_{HH} from 2.59Å to 2.96Å. From the results shown in figure 3.4, we identify two limit conditions: the "increased $\varepsilon_{\mathrm{CH}}$" and the "increased σ_{HH}". The "realistic" results are, in fact, strictly contained between the two cases which effectively approximate the extreme situations of highest or lowest pressure, respectively. Therefore the $\varepsilon_{\mathrm{CH}}$ does strengthen the hydrogen uptake but, at moderate pressure, it is countered by the H_2 repulsion (driven by the σ_{HH} value) which then becomes predominant. We choose not to modify the σ_{CH}

parameter because, in SWNTs, this would move the adsorption layer farther from the surface and, therefore, implicitly reduce the available space for hosting H_2 molecules.

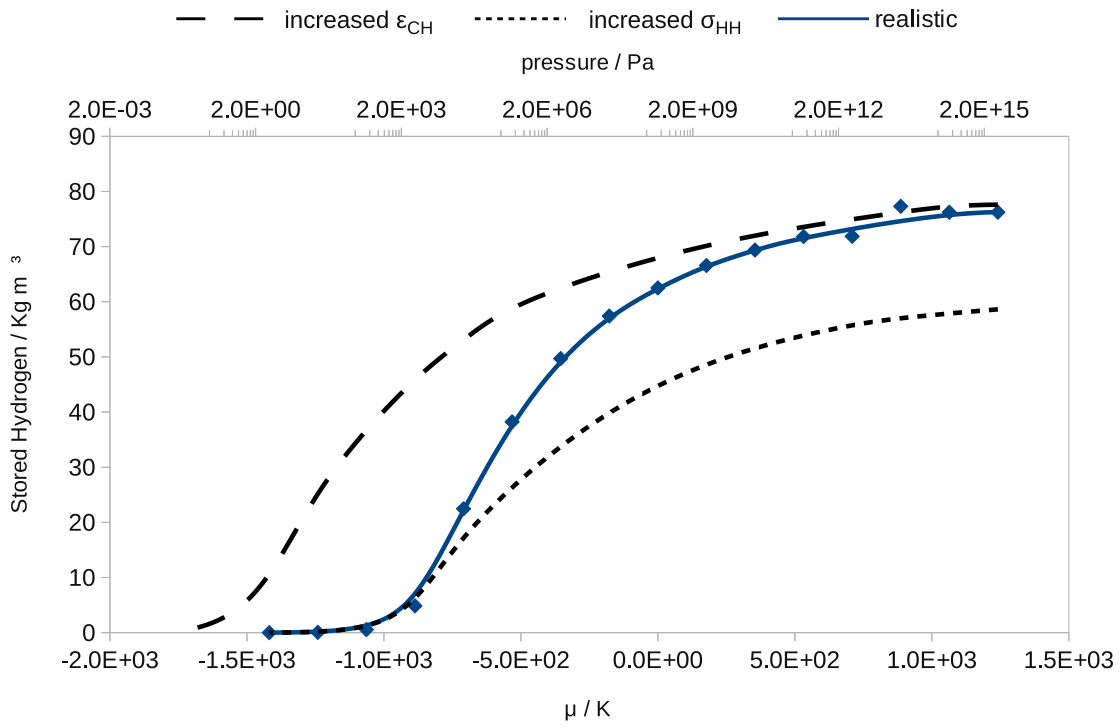

Figure 3.4: *GCMC simulated adsorption isotherm inside a (16,0) SWNT at 77K: the "realistic" plot, whose potential parameters are taken from table 3.2, lies between the limit conditions of "increased* ε_{CH}*". This enhances CNT uptake and "increased* σ_{HH}*" which strengthen the hydrogen repulsion.*

Different sized SWNTs are then simulated, at $77K$ and $300K$, in order to investigate geometry effect on adsorption capability. Size range goes from (11,0) up to (19,0); only zig-zag type has been considered, after having verified that only small changes would occur through armchair, zig-zag or chiral SWNTs of similar diameter. For comparison purposes H_2 free gas simulated density plot vs. pressure is represented as well in figure 3.5. It can be seen that there is a range of pressures where the hydrogen density in nanotubes is higher than the free gas. These simulations however do not take the whole available surface into account but just the inside of the SWNT. Besides, it is well known that other type of nano-pores are available in CNT bundles[61], so the realistic prediction should be slightly higher. The hydrogen densities increase steeply with pressure until molecules fill the whole available space, then the slope decrease significantly, so that much pressure is needed for further density increase.

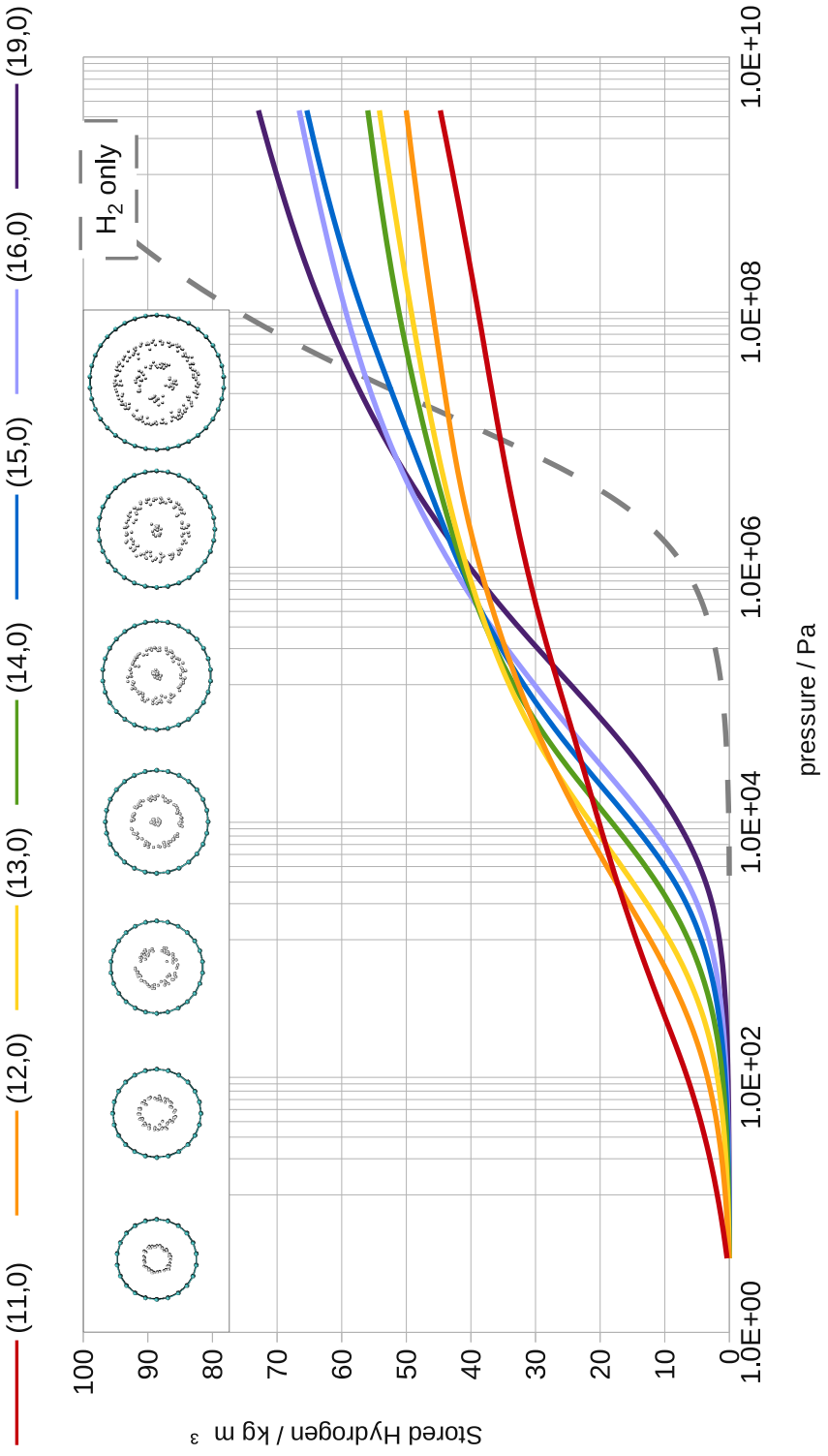

Figure 3.5: *Simulated adsorption isotherm of isolated SWNT of different radius at 77K – in the inset: snapshots of the involved SWNTs, at the end of the simulation.*

In logarithmic scale ($\propto \mu$), as represented in figure 3.5, the isotherm appears like a sigmoid function which becomes more flat as the pore size is reduced. The results at $300K$ (not shown) are in perfect agreement with these ones but the plots are shifted to higher pressure, and the obtained densities are substantially lower. Narrower SWNTs' adsorption is indeed higher than wider ones at lower pressure but their capacity falls when the pressure increases, thus inverting the relative performances. This is due to the emergence of hydrogen repulsion which rise steeper in tiny spaces and actually counters the higher uptake capability. In this context free H_2 can be interpreted as an infinite diameter nanotube where there is no uptake and no confinement at all.

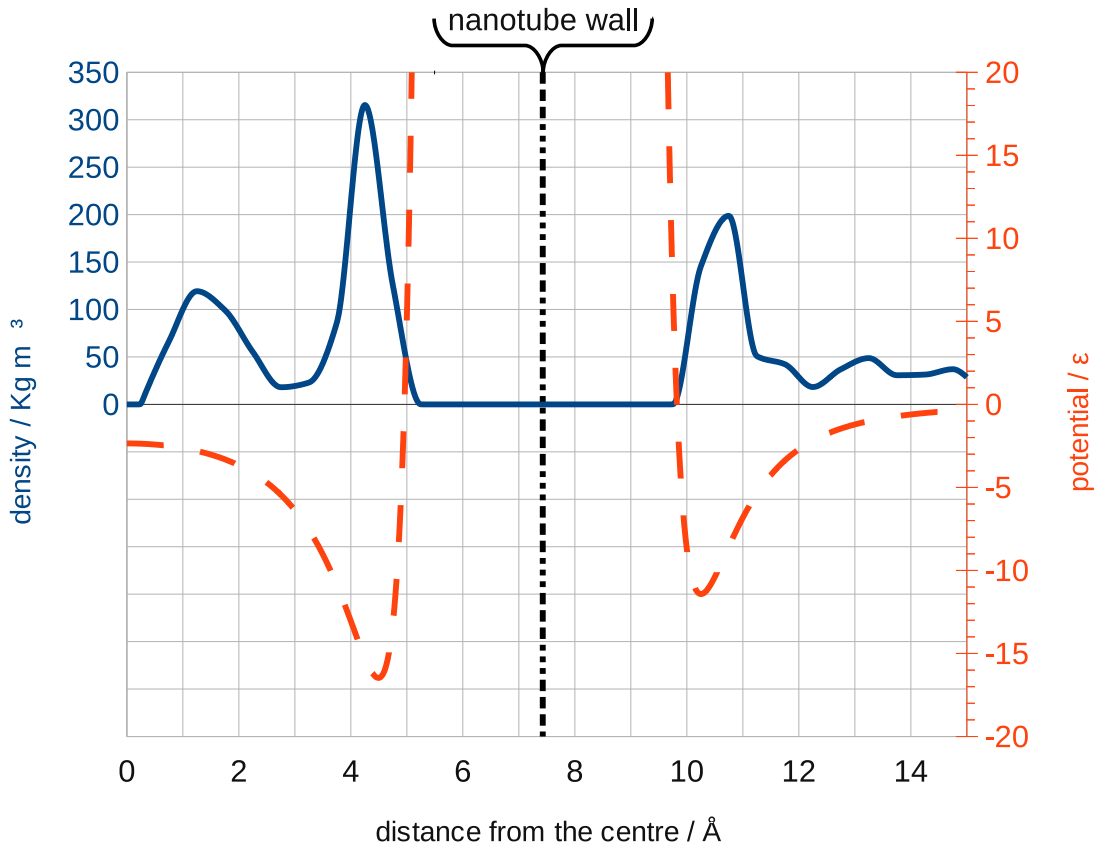

Figure 3.6: *The simulated H_2 radial adsorbed density, at $75K$ and $62.5atm$, inside a (19,0) SWNT and the relative PES radial section: the comparison enlightens the presence of a second H_2 layer inside the CNT, close to the centre, which lies in a region not favoured by the interaction with the nanotube.*

At very high pressures, if the diameter is large enough (see the inset of figure 3.5), multi layer are also formed. Figure 3.6, in fact, shows the calculated H_2 radial density adsorbed around an isolated (19,0) SWNT. These results enlighten, in fact, the

presence of two adsorption regions inside the nanotube after GCMC simulation runs at $\mu = -315.06K$ (*ca.*62.5atm) and $75K$. Further layers adsorbed in the inner space are only explicable by invoking the interactions between hydrogen molecules, since the inner PES shows just one minimum, corresponding to the first adsorbed layer. It is therefore reasonable that the adsorption capacity, at lower pressures, is driven by the potential well depth (which increase as the radius is smaller). Nevertheless, the high pressure behaviour is strictly connected with the interactions between the adsorbed molecules and thus with the hard radius of the relative potential, especially in confined spaces. Therefore, CNT wall's action, when interacting with high H_2 densities, is just to confine the molecules and, in the case of the inner side of a CNT, force their spatial distribution into the characteristic cylindrical shape.

Even at low pressure and temperature, no preferred adsorption sites have been identified within CNT systems. It has been only found an optimum adsorption distance, without any correlation to the roughness of the inner surface, which is indeed quite low due to its curvature. For the sake of comparison we have checked the properties of a completely flat surface as a graphene sheet of 200 atoms with bond lengths of 1.421Å. The energy difference within the classical PES, calculated with parameters from [109] (see table 3.1) at the optimum adsorption distance, is only *ca.*$0.5\varepsilon_{\mathrm{CH}}$ for both (16,0) and (19,0) SWNTs, less than half of the value relative to an open graphene sheet which is *ca.*$1.1\varepsilon_{\mathrm{CH}}$.

3.4.4 Anisotropy effect

Although adsorption results did not show significant difference between one centre or two centres model, we should take into account that hydrogen molecule is also a quantum rotor. The simulation algorithm do not to explicitly consider rotations, but only the displacements of molecules within a certain force field (either external or generated by other molecules). This is a common approximation in quantum mechanics and lies upon the huge difference, in terms of energy, between rotations and translations. In fact, rotations are extremely faster so that they can be considered as completely independent. Therefore, in a two centres model this means to pick up at random a new orientation at least after each displacement. The single centre model, however, assumes that energy difference between the orientations are too small compared with the rest and therefore their contribution can be neglected. This is the case of most of the simulations here presented.

However, in order to get a better insight on the effect, we consider an isolated molecule,

approaching a surface, and focus on how the force field generated by this one affects the orientation. As seen in section 3.2, Kuchta *et al.* studied the interaction with a graphite slit pore[53]. Here we consider the inner surface of a SWNT as well as the typical pores of a nanotube bundle (represented in figure 1.2 and figure 3.2).

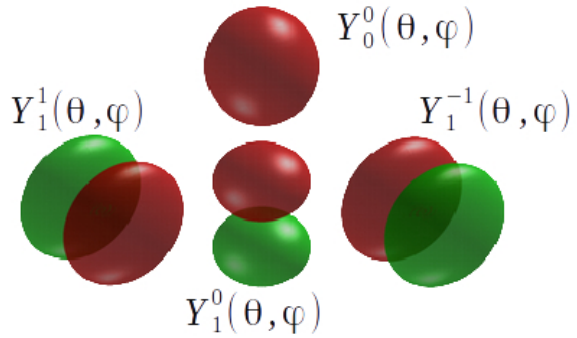

Figure 3.7: *Schematic representation of spherical harmonics.*

Spherical harmonics are solutions of the Schrödinger equation for the rigid rotor.

$$\begin{cases} Y_0^0(\theta,\varphi) &= \frac{1}{2}\sqrt{\frac{1}{\pi}} \\ Y_1^{-1}(\theta,\varphi) &= \frac{1}{2}\sqrt{\frac{3}{2\pi}}e^{-i\varphi}\sin\theta \\ Y_1^0(\theta,\varphi) &= \frac{1}{2}\sqrt{\frac{3}{\pi}}\cos\theta \\ Y_1^1(\theta,\varphi) &= -\frac{1}{2}\sqrt{\frac{3}{2\pi}}e^{i\varphi}\sin\theta \end{cases}$$

The real harmonics are obtained as linear combination of the base functions

$$\begin{cases} S &= Y_0^0 \\ P_x &= \sqrt{\frac{1}{2}}\left(Y_1^{-1} - Y_1^1\right) \\ P_y &= i\sqrt{\frac{1}{2}}\left(Y_1^{-1} + Y_1^1\right) \\ P_z &= Y_1^0 \end{cases}$$

Even at room temperature, most of the molecules occupy the first two levels of the rotational states; when the temperature drops, they become even more relevant. For this reason the quantum rotor model of the H_2 molecule used here takes into account only such states.

The first, fundamental level (as seen in figure 3.7) is totally spherical-symmetric, this also justifies the choice of the one-centre (isotropic) model. On the other hand, the three function of the second level are iso-energetic and their linear combination is also spherical. For an isolated molecule, obviously, all three states will be equally occupied.

The presence of a force-field, not strong enough to cause significant modifications on the functions, is capable of producing a loss of degeneracy. This would be the case of

the physiorption on a surface. We then investigate how the adsorption inside a SWNT can affect the distribution of the levels.

This means solving the integral, over the whole space, as a function of $\mathbf{R}$ the distance between the centre of mass of the molecule and the surface,

$$\Delta E(\mathbf{R}) = \int |Y_l^m(\theta,\phi)|^2 \; V(r,\theta,\phi,\mathbf{R}) \; \delta(r-r_0) \; r^2 \sin\theta \; dr \; d\theta \; d\phi$$

where θ and φ are the spherical coordinates, $V(r,\theta,\varphi,\mathbf{R})$ the interaction potential, and $\delta(r-r_0)$ is Dirac delta function, with $r_0 = 0.37$Å set to a distance half the value of the hard radius used in simulations.

We numerically solve such integral using a MC integration (see section 2.3.2) software, written on purpose, considering a molecule interacting with a graphene (flat) surface or various surfaces of a $(16,0)$ SWNT bundle. The axis orientation makes x the one which contains the direction of the approach of the molecule towards the surface. The results are shown in figure 3.8. Since all energies are expressed in the general terms of ε_{CH}, the plot do not include the base difference of $\sim 175K$ between the first two quantum levels.

The graphite results are comparable with Kuchta *Ket al.*[53], and is is also clear that with all the other surfaces the loss of degeneracy is complete.

3.5 Conclusions

Common interaction potentials have their well depth scaled to *ca.*$30K$, *ca.*$40K$ and *ca.*60 according to their parametrization procedure, respectively through Lorentz-Berthelot mixing rules, fitting scattering experiments[109], or *ab initio* calculations. Considering one LJ example potential for each type we found that the adsorption energy on the inner surface of SWNT decrease with the size of the pore. About the potential parameters, besides the obvious dependence on $\varepsilon_{\mathrm{CH}}$, we also enlightened a linear correlation between the adsorption energy and σ_{CH}. However, even at moderate pressure, the maximisation of the adsorption energy is not the only criterion for enhancing the total amount of H_2 stored. Running GCMC test simulations with hypothetical potentials, with increased adsorption energy (higher $\varepsilon_{\mathrm{CH}}$) or hydrogen repulsion (higher σ_{HH}), we showed the competition between the two effects, proving as well that the theoretical limit capacity depends almost exclusively on the latter. Such competition is even more evident comparing different sized SWNTs: despite the smaller ones have the higher adsorption energy, they offer little space for H_2 molecules

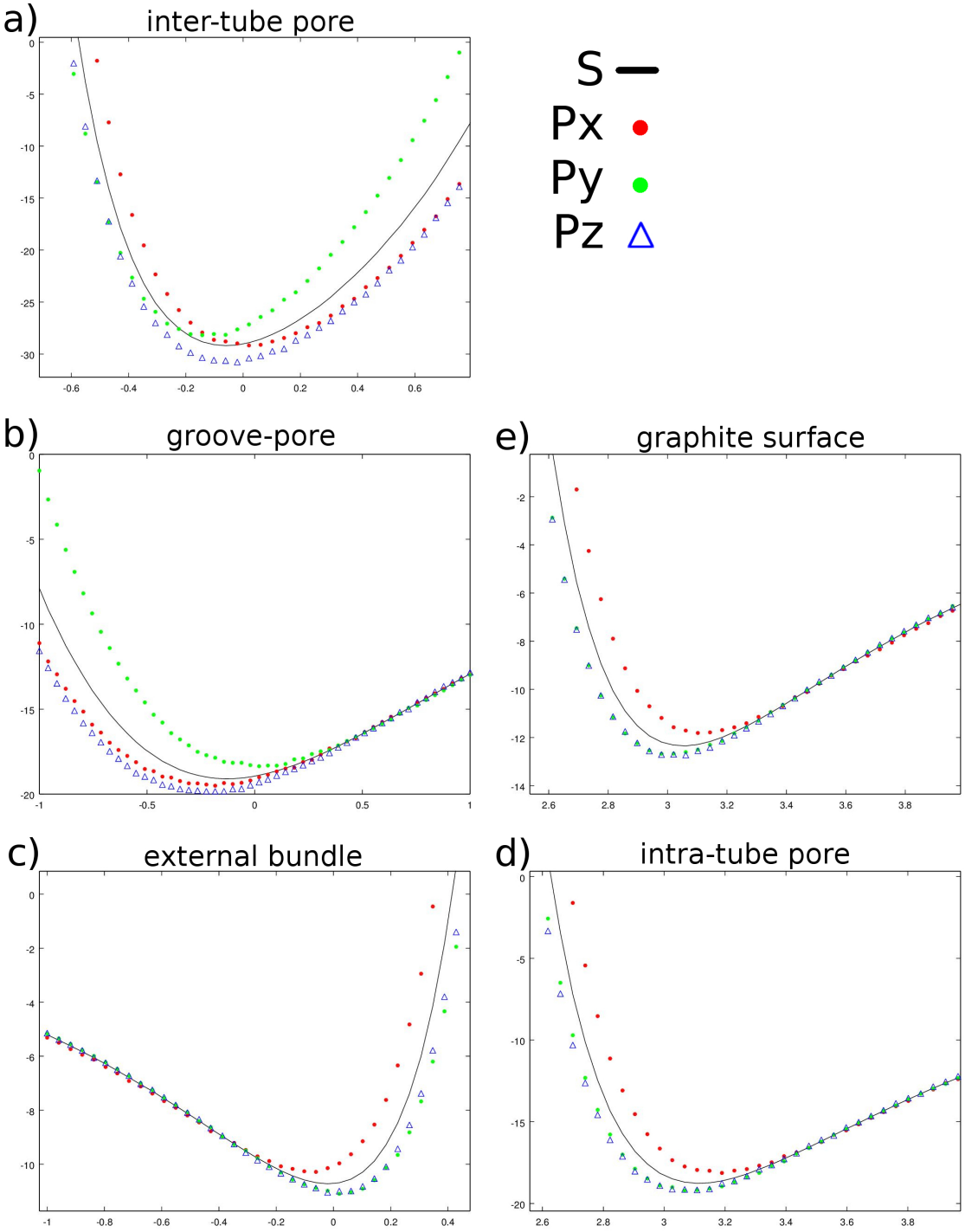

Figure 3.8: *Numerical integration of spherical harmonics interacting with CNT and graphite surface. Energy units are in ε_{CH} and distance is in Å. Insets a) b) and c) use the same axis reference of figure 3.2; data of d) and e) are shown as a function of the distance of the surface of the CNT and graphite respectively.*

to spread and thus the repulsion is also higher. What has been seen is that, smaller SWNTs have higher adsorption at lower pressure but the larger ones improve more steeply as the pressure increase, allowing higher densities to be hosted. Pure hydrogen was also considered as the limit condition of an infinite large pore with no uptake and no confinement at all: this allows to identify the pressure range for convenient storage into a certain SWNT. Simulations of some large radius SWNTs also led to multiple layer adsorption, which also confirms the preponderance of hydrogen interactions at higher pressure.

Chapter 4

Diffusion studies

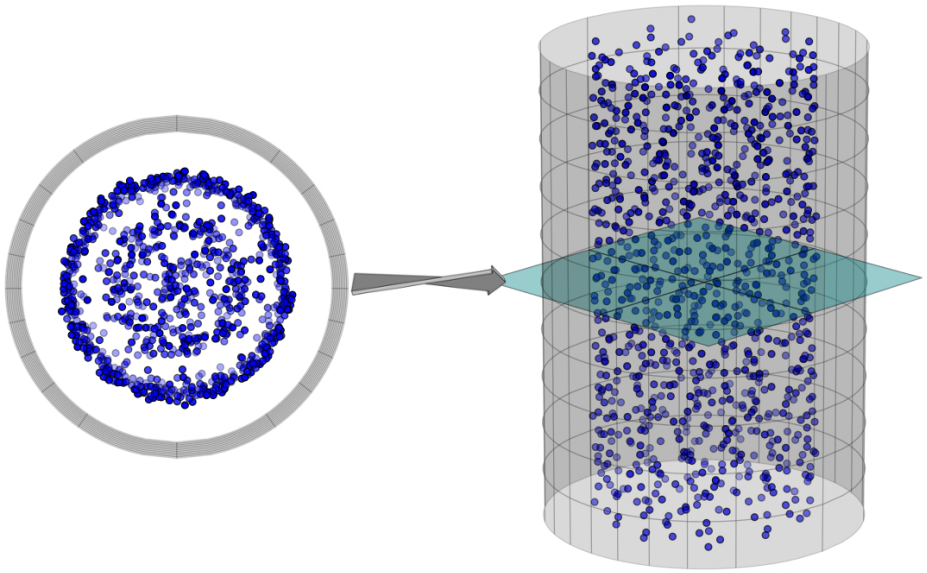

The diffusion and adsorption of gases inside porous structures have already been the focus of some theoretical and experimental studies. For instance, based on classical MD, the self-diffusivity of methane inside SWNTs was studied at different temperatures and pressures [9]. Furthermore, the different diffusion regimes that can occur inside a SWNT were already identified [72]. Other studies focused on molecular diffusion and dynamic flow of various gases (methane, ethane, ethylene) inside CNTs [64, 18]. The attractive point about the diffusion inside CNTs is that, for light gases, such as methane and hydrogen, it is orders of magnitude higher than in other conventional porous materials such as zeolites [100].

Nevertheless, though some studies[100, 15] indicate high rates of transport in nanotubes, the self-diffusion, also known as Brownian motion, has not been as much

investigated. This diffusive regime plays the key role in the description of situations where the potential gradient is zero, the loading of particles is high and the pore diameter is not extremelly small [72]. Therefore, in order to address and facilitate the study of the self-diffusivity of gases inside SWNT, a self-made tool based on the KMC method [68, 5, 85, 113] was developed. This tool estimates D_s and evaluates the dependence of different distribution of gases on system's variables like the number of particles, temperature and geometrical parameters.

Below, as an illustrative application, we study the self-diffusion of hydrogen molecules inside a SWNT and evaluate how it is affected by its concentration and by the geometrical parameters of the SWNT (Sec. 4.3). The simulation model is explained in Sec. 4.2, where an overview of the MC/KMC methods is given, the SWNT and H_2 models are explained (Sec. 4.2.1), and the method used to obtain the D_s is shown (Sec. 4.2.2).

4.1 Brownian motion

The phenomenon takes the name from the observation of pollen grains suspended in water performed by Robert Brown in 1827[108]. The characteristic of such motion is the high frequency of collisions and the consequent very short mean free path. This makes displacements practically isotropic, since after so many collisions the particle no longer "remembers" the previous trajectory. It is worth to notice the affinity of such kind of situation with stochastic methods and MC methods. In such context, for statistical reasons, particles will tend to diffuse from zones with high concentration towards others where it is low. The explanation lies, of course, in the isotropy of displacements and, consequently, each particle diffuses with the same probability, so in absolute terms (*i.e.* number of particles $\times$ probability) the flux will be higher.

Analytically the problem was solved by Einstein in 1905[26] for a one dimensional system where N non-interacting particles, at $t = 0$ are released all in the position $x = 0$ and then left free to diffuse. The density $\rho(x, t)$ is expanded in a Taylor series, so that most of the terms either vanish by symmetry or are neglected. The diffusion coefficient D is then related to the mean square displacement by the equation

$$\frac{\partial \rho}{\partial t} = D \frac{\partial^2 \rho}{\partial x^2}. \tag{4.1}$$

The solution of equation 4.1

$$\rho(x,t) = \frac{N}{\sqrt{4\pi Dt}} \exp\left(-\frac{x^2}{4Dt}\right) \tag{4.2}$$

is a normal distribution with mean $\mu = 0$ and variance $\sigma^2 = 2Dt$. On this basis, it is frequently used in simulations, the mean square displacement $\langle x^2 \rangle$ in order to obtain an estimation of D_s.

4.2 Simulation details

The aim of this work was to develop a simulation tool that allows the determination of D_s of molecular hydrogen, H_2, inside SWNTs. The simulation method developed is based on the MC algorithm. This choice relies on the fact that this kind of algorithm allows a more effective exploration of the possible microstates of a system, a feature that is not possible in deterministic simulation methods like MD that follow the least action path. MC algorithms are really useful when the goal is to produce a large sample of microstates in order to obtain the average thermodynamic properties of a system. Furthermore, in comparison to MD simulations, they have the advantage of being computationally cheap, easy to implement and capable of simulating larger time scales [4, 82].

The designed algorithm accepts as input values of the variables of a canonical ensemble (NVT) - N, number of molecules; V, volume of the cell; T, temperature of the system - and the desired initial distribution of molecules. The code was written from scratch in Python [89] language. A simulation consists of iterations, called cycles, which allow the exploration of the configurational space available to each hydrogen molecule of the system.In every cycle, each particle has the chance to perform a displacement, according to the equation: $d = -\log \eta$. In this distribution, η is a random number sampled from a uniform distribution, with $\eta \in [0, 1[$, and d is the value of the generated displacement. This distribution has the advantage that

$$\begin{cases} \lim_{\eta \to 0} d = +\infty \\ \lim_{\eta \to 1} d = 0 \end{cases}$$

therefore, it maximizes the translational degrees of freedom of the system (in relation to the use of a unitary displacement) because a molecule can have any value of $\mathbb{R}^+$ for its displacement. It should be said that such displacement could then suffer further transformations during a simulation step (*e.g.* due to confinement) but in this context the point is that actually all displacements are possible.

This approach has a huge impact on the number of displacements that are accepted, since some of them are more likely to happen in equilibrium than others: smaller displacements are usually more easily accepted than larger ones. Moreover, whenever a displacement occurs, the system's microstate changes. The displacements can be done in any direction of space. Spherical coordinates θ and ϕ are generated from uniform distributed random numbers, though a correction is needed to ensure that the points picked in this way do not gather with higher probability near the "poles", thus granting the isotropy of the sampling[65]. Therefore, being ξ_1 and ξ_2 two random numbers between 0 and 1, we get

$$\begin{cases} \theta = 2\pi\xi_1 \\ \varphi = \arccos(2\xi_2 - 1) \end{cases} \rightarrow \begin{cases} \hat{x} = \cos\theta \sin\varphi \\ \hat{y} = \sin\theta \sin\varphi \\ \hat{z} = \cos\varphi \end{cases}$$

where $\hat{x}$,$\hat{y}$ and $\hat{z}$ are the component of the unit vector which indicates the direction of the diplacement.

In the code, particles are confined inside the SWNT in two ways: by imposing reflexive conditions on its wall or by making the SWNT's wall a rigid barrier. Reflexive conditions are imposed in order to modulate the collision of a molecule with the SWNT's wall, a description based on the Law of Reflection. Consequently, whenever a H_2 displacement makes the molecule collide with the SWNT's wall, it is reflected with an angle equal to the one of incidence. Hence, this confinement scheme ensures that, after a displacement, the molecules always ends inside the SWNT. On the other hand, the rigid barrier model is based on the idea that outside the SWNT the potential is infinite. In this way, whenever the final position of a molecule after a displacement is outside the SWNT, the displacement is refused. Overall, we must be careful on the choice of the confinement scheme because it definitely influences the number of displacements which are accepted during the simulation and, consequently, they can be important do speed-up the configurational sampling. Furthermore, if interactions with SWNT are included in the simulations, the high repulsive part can be included in either one of the confinement schemes, in order to automatically exclude such kind of displacement and hence decrease the amount of energy calculations performed.

The next step, after the displacement and the confinement are performed, is to calculate the energy of the new configuration. This value is computed taking into account two types of interactions: hydrogen molecules with themselves and with the SWNT's wall. Both interactions are modulated by a 12-6 LJ potential. The details of these interactions are explained in Sec 4.2.1.

Finally, the probability of accepting the new generated configuration is determined by the Metropolis criterion [69], as explained in section 2.6.1 (equation 2.30).

4.2.1 Simulation Models for H_2 and SWNT

The models used to describe the components of the systems - the SWNT and the H_2 gas molecules - will be explained in this section, as well as the potentials used to describe their interactions. Firstly, due to the fact that nanotubes have continuous and smooth walls of uniform composition [41], they were modeled as non-atomistic cylindrical-shaped pores. This simplification saves a lot of computational time mainly because it reduces drastically the number of interactions that have to be calculated, which is the most computationally expensive part of the algorithm. Moreover, this approximation allows the study of a limit situation where the SWNT is static, which means smooth, homogeneous and without vibrations.

On the other hand, H_2 molecules are modeled as one center spherical particles. This choice relies on the fact that an atomistic H_2 model was previously tested and the two models gave identical results in this context.Therefore, the model chosen was the one that is computationally cheaper.

Finally, periodic boundary conditions were applied along the z-axis of the SWNT, which corresponds to the direction of wrapping axis (see section 1.1). These boundary conditions are based on the idea that a real SWNT can be considered as having infinite length due to its very high aspect (*i.e.* length/radius) ratio [24].

The interaction between different hydrogen molecules and between them and the SWNT's wall are modulated by the 12-6 LJ potential. The SWNT internal energy is not supposed to vary in this context and is therefore neglected. In this stage of the developing procedure, it is worth considering as less variables as possible, and leave the non essential ones to further parametrizations. The 12-6 LJ parameters for H_2-H_2 interactions are adapted from literature[8], being $\sigma_{\mathrm{HH}} = 3\text{Å}.$ and $\epsilon_{\mathrm{HH}} = 30K$. Furthermore, a cut-off distance is set at $r_c = 8\text{Å}$.

Since the SWNT is modulated as a cylindrical pore, the value of ϵ in the SWNT-H_2 interaction has a special treatment because it has to take into account the influence of all carbon atoms inside a significant region of a real SWNT wall that contribute to the potential at a certain point. As long as the nanotube radius is kept reasonably larger than the particle hard radius, the atomistic potential well generated by the presence of the SWNT deepens as the pore size shrinks [59]. Nevertheless, since this

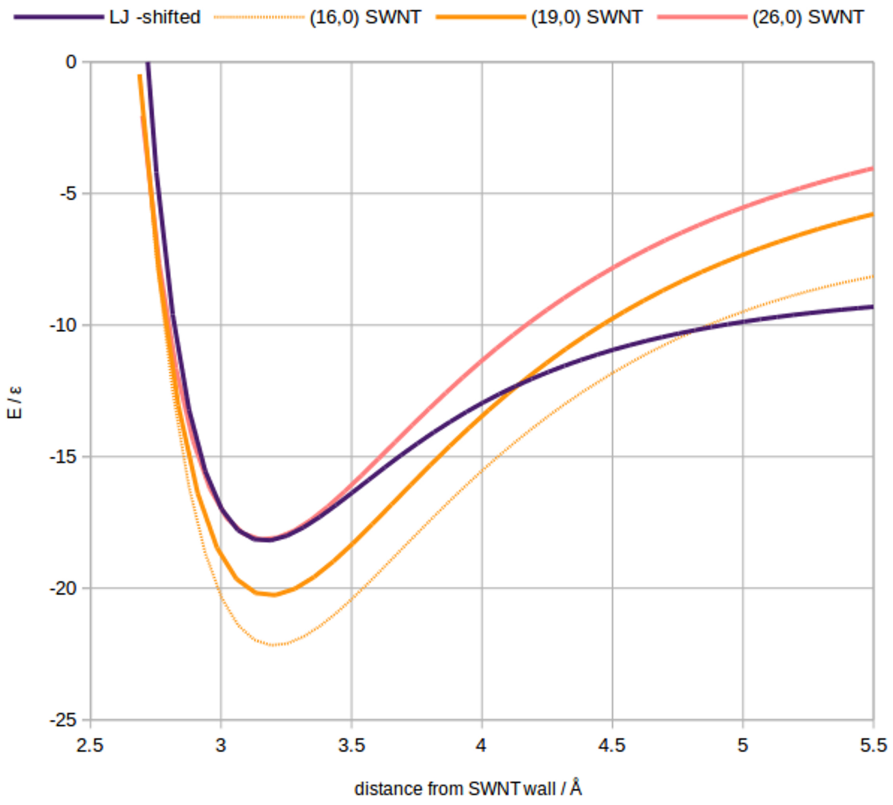

Figure 4.1: *Comparison between atomistic potentials of* $(16,0)$*,*$(19,0)$ *and* $(26,0)$ *SWNT with the non-atomistic potential used in simulation (shifted for comparison purposes).*

work is about comparing SWNT with different radius, we need a potential that does not vary too much within the range of *radii* under investigation. To achieve this goal we fit the shape potential well, generated by atomistic LJ potentials obtained with Lorentz-Berthelot mixing rules [104], and impose that the first derivative beyond $r = 5$Å from CNT surface is equal or lower than 0.05. It results a weaker potential (well depth $\approx 9.7\epsilon_{CH}$ compared with $\approx 18\epsilon_{CH}$ for the atomistic potential), but the energy calculated beyond $r = 5$Å is less than 1% of the value measured within the potential well. It is represented in figure 4.1, together with the atomistic potentials of $(16,0)$,$(19,0)$ and $(26,0)$ SWNT; it has been shifted fo comparizon purposes. In fact, it has been observed that, in terms of GCMC simulated storage capacity, the system at medium and high pressure is only weakly affected by the potential well depth, being repulsions increasingly more relevant [59].

4.2.2 Determination of Diffusion Coefficents

There are multiple transport mechanisms that can occur inside SWNTs but this work will focus only on the motion by diffusion, neglecting any kind of other transport by bulk flow. Diffusion mechanisms depend on the local structure properties inside the SWNT, namely, the strength of the interaction of the molecules with the pore, as well as on the relative ratio of their sizes. The different types of diffusion mechanisms that can occur inside a pore were described by Mutat T. *et al.*[72], who established a correspondence between different regions of the pore, which are associated with typical clusters of particles, and the types of motion that can occur there. Let us consider a pore loaded with molecules and subjected to a pressure at its both ends (these pressures can be equal or not). The outer zone of the pore is usually populated by an outer layer (or adsorbed layer), in which two different types of motion can occur: at low densities, the motion is mostly ballistic and can (or cannot) be hindered by counter diffusion and, at high densities, 2D Brownian motion predominates. In the inner zone of the pore, if layers are formed, the former motion regime is applied. In the case where scatters or agglomerates of particles are formed, the diffusion can occur due to collisions with the potential barrier of the wall, which would correspond to a Knudsen diffusion with effective radius, $r_{effective} = R_{SWNT} - \sigma_{\mathrm{CH}}$. This regime is suitable to describe pores at low loadings. For large pores ($r_{effective} >> 1$) and high loadings, the diffusive regime is a 3D Brownian motion. It is important to note that ballistic diffusivity is dependent on the pore length, whereas 2D Brownian motion is concentration dependent. On the other hand, Knudsen diffusion occurs if the free path of the gas is larger than the pore diameter and molecule-wall collisions predominate over molecule-molecule collisions.

The goal of this work was to study the Brownian motion of H_2 in SWNTs with medium to large radius (5-20Å) and in situations where the density of particles is high and the system is in equilibrium. Furthermore, a SWNT with small radius (3.5 Å) was also considered as a limit situation of single-file diffusion. Unfortunately, due do the high number of collisions, ca. 10^{21} per second, it is impossible to know in detail the behavior of this motion regime. However, if it is assumed that the molecules' trial displacements are isotropic and random, it is possible to simulate the average behavior of the system by using the KMC method described previously. This method can take into account the interactions between elements of the systems and it also enables the study of gas motion within the nanotube. This is possible because the collisions between molecules are isotropic and those with the SWNT's walls are anisotropic, a fact that imposes restrictions to the flux.

The self-diffusivity of H_2 was obtained through the mean square displacement, $\langle \Delta r^2 \rangle$, of the N individual molecules, according to the equation stated by Einstein [26]:

$$D_s = \lim_{\Delta t \to \infty} \frac{1}{\Delta t} \frac{1}{2dN} \sum_{i=1}^{N} (r_i(t + \Delta t) - r_i(t))^2 \tag{4.3}$$

where d is the dimensionality of the studied diffusion process, which is 3 in this study. It is worth to mention that this equation is only valid when $\langle \Delta r^2(t) \rangle$ is a linear function of time [44], which was confirmed to be the case of our simulations, once concluded the equilibration stage. This is strictly related to the fact that in equilibrium the average potential energy of the system is constant and, consequently, the linearity of equation 4.3 is automatically ensured.

4.3 Results

The D_s of H_2 was determined through simulations done at equilibrium conditions, *i.e.* when there is no concentration gradient, the average total energy of the system is kept constant, and there is no internal exchange of energy between kinetic and potential energy. The goal of these simulations was to understand which structural properties of a SWNT - radius (R, Sec 4.3.2), length (L, Sec 4.3.3) and aspect ratio (R/L, Sec 4.3.5) - influence the D_s while keeping the concentration of H_2 constant to a reference value. Furthermore, the influence of the concentration of H_2 (Sec. 4.3.1) was also investigated by using different particle loadings inside the reference SWNT. This reference SWNT, which is represented in figure 4.2, consists in a simulation cell with R=10Å and L=200Å, oriented so that its direction of longitudinal growth is aligned with the z axis and its transversal sections are parallel with the xy plane.

All the simulations were performed using initial random distributions of particles. These distributions were generated with an algorithm that picks up uniformly random positions inside the volume of the SWNT. Moreover, the temperature chosen for the simulations was 77K because it corresponds to the boiling point of liquid nitrogen, which is commonly employed to cool systems to very low temperature. Finally, the number of cycles performed in every simulation was 2×10^5 , which is the value of the displacement attempts for each particle. The estimated values of the D_s were obtained after equlibration of the system.

Table 4.1 shows the D_s obtained using equation 4.3, their respective standard de-

viations, the geometrical parameters of the SWNT, the number of particles used in each simulation, the (m,n) indexes of zig-zag SWNTs which have similar radius to the ones used, and the H_2 percentage of mass fraction, H_2 wt%, which was calculated by $\frac{m_{H_2}}{m_{H_2}+m_{SWNT}} \times 100$

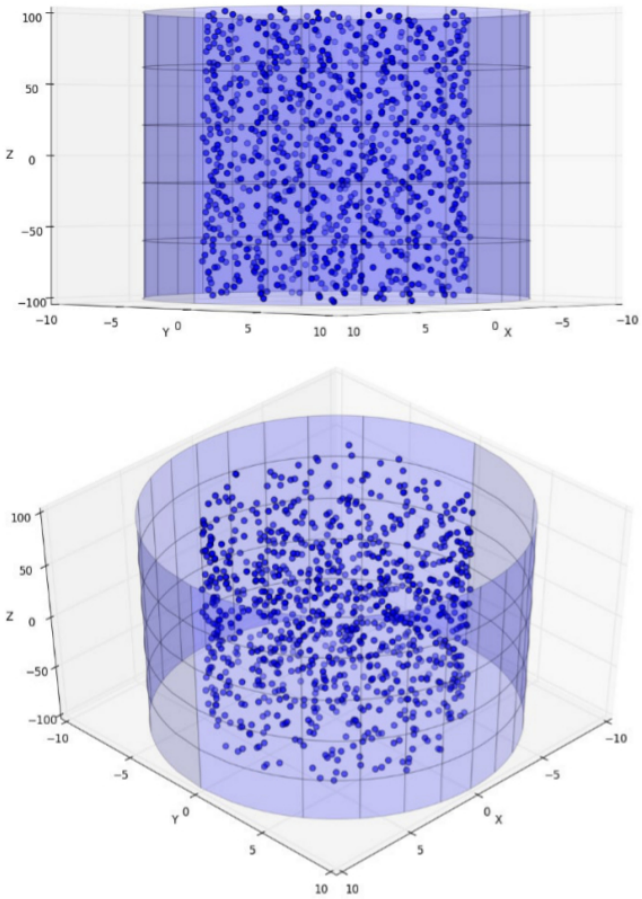

Figure 4.2: *Representation of the reference SWNT cell (*R*=10Å and* L*=200Å), which is modulated as a continuous smooth cylinder. The distribution of 1000 particles after* 2×10^5 *displacement attempts is also shown.*

4.3.1 Influence of Concentration

In order to study the influence of the H_2 concentration inside the reference SWNT (R = 10Å and L = 200Å) on the value of D_s, five simulations were performed with different total number of particles, namely, 250, 500, 750, 1000 and 1500.

Figure 4.3 depicts the distribution of particles on a projection plane perpendicular to the longitudinal axis of the SWNT after 2×10^5 displacement attempts. Through the

Table 4.1: *Summary of the geometrical parameters,* R *and* L*, number of particles used, N, (m,n) indexes of the correspondent zig-zag nanotube, and the H_2 percentage of mass fraction, H_2 wt%. The D_s and the correspondent value of the standard deviation, σ, are also shown. All the simulations performed 2×10^5 cycles.*

N	***R* (Å)**	***L* (Å)**	**Zig-Zag Type**	H_2 ***wt%***	$D_s \times 10^9$ $(m^2 s^{-1})$	$\boldsymbol{\sigma}\times 10^9$ $(m^2 s^{-1})$
Influence of Concentration						
250	10.0	200.0	(25,0)	0.4413	10.073	0.002
500	10.0	200.0	(25,0)	0.8789	9.223	0.001
750	10.0	200.0	(25,0)	1.3126	7.322	0.008
1000	10.0	200.0	(25,0)	1.7425	5.1088	0.0002
1500	10.0	200.0	(25,0)	2.5911	2.2550	0.0009
Influence of *L*						
250	10.0	50.0	(25,0)	4.2453	5.1486	0.0006
500	10.0	100.0	(25,0)	3.2979	5.1238	0.0005
750	10.0	150.0	(25,0)	2.1686	5.1151	0.0003
1000	10.0	200.0	(25,0)	1.7425	5.1088	0.0002
Influence of *R*						
94	5.0	200.0	(13,0)	0.3195	6.211	0.001
426	7.5	200.0	(20,0)	0.9355	5.472	0.002
2871	15.0	200.0	(38/39,0)	3.2003	4.6649	0.0005
5706	20.0	200.0	(51/53,0)	4.6392	4.4612	0.0003
Influence of *R/L*						
1000	3.5	21159.00	(10,0)	0.0418	4.362	0.0006
1000	5.0	2142.00	(13,0)	0.3174	6.082	0.001
1000	7.5	469.00	(20,0)	0.9364	5.4551	0.0005
1000	15.0	70.00	(38/39,0)	3.1694	4.7178	0.0008
1000	20.0	35.05	(51/53,0)	4.6393	4.6881	0.0004

analysis of this figure, it can be seen that for the first two simulations only one distinct layer of particles was formed. The formation of this layer, which is ubiquitous for all the simulations, occurs mainly because of the interaction between particles and the SWNT's wall. Its position - around 3Å from the SWNT's wall - is strictly related to the bottom of the potential well that the LJ potential gives rise to (see Sec. 4.2.1). Furthermore, in the case of 750 particles, apart from the outer layer, an inner scatter emerges. In the SWNT with 1000 particles, the distribution obtained shows an outer and intermediate layers, and a packed agglomerate inside the intermediate layer was formed as well. Finally, with 1500 particles, three distinct layers were formed and there are almost no scattered particles in other regions of the nanotube.

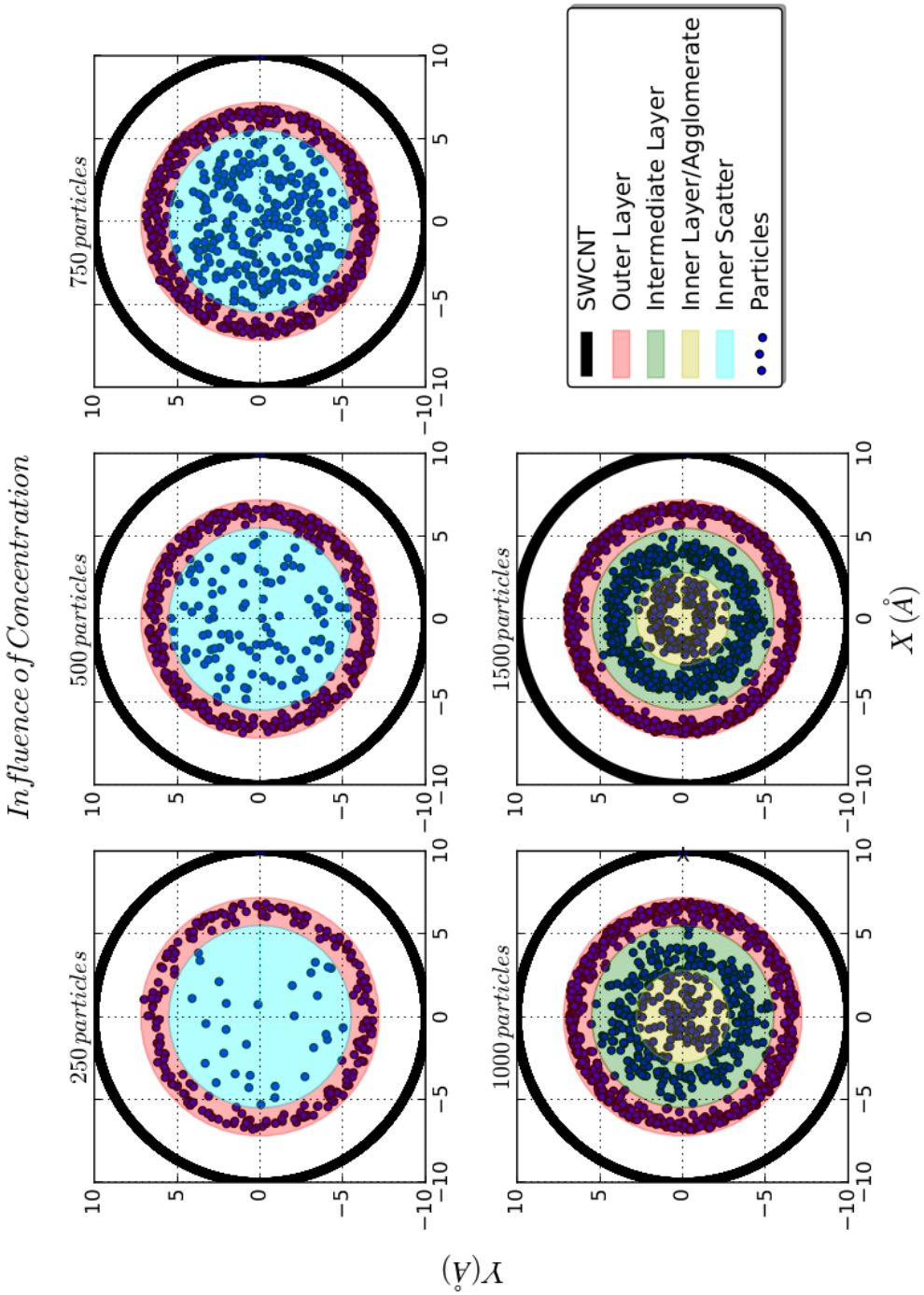

Figure 4.3: *Distribution of particles on a projection plane perpendicular to the longitudinal axis of the SWNT. The simulations were performed at different concentrations - achieved by varying the number of particles in each simulation and by keeping constant the geometrical parameters ($R = 10$Å *and* $L = 200$Å*). Relevant zones are highlighted with different colors.*

Hereupon, it is clear that the number of layers formed is a direct consequence of the concentration, *i.e.* the higher the concentration of particles, the higher the number of layers. These organized structures try to minimize the relative number of repulsive interactions between their particles. This can be seen in figure 4.4, which represents, for each colored area of figure 4.3, the number of interactions where the distance between two particles, r, is less than 3 (the σ_{CH} value of the interaction potential) over the total number of H_2-H_2 interactions that occur in that region. This value can be interpreted as a ratio of unfavorable interactions. This figure shows that, for all simulations, the ratio of unfavorable interactions is lower in layers than in scatters or agglomerates, which is a consequence of the organization inherent to the layers. Furthermore, in distributions where more than one layer is formed (simulations with 1000 and 1500 particles), the ratio of unfavorable interactions increases from the outer to the inner layers. Since more organized layers should have a lower number of relative unfavorable interactions, this observation may be an indication that the inner layers cannot achieve an ordering state as efficient as the outer layer does due to volume constraints. It is necessary to note, however, that the ratios obtained are small.

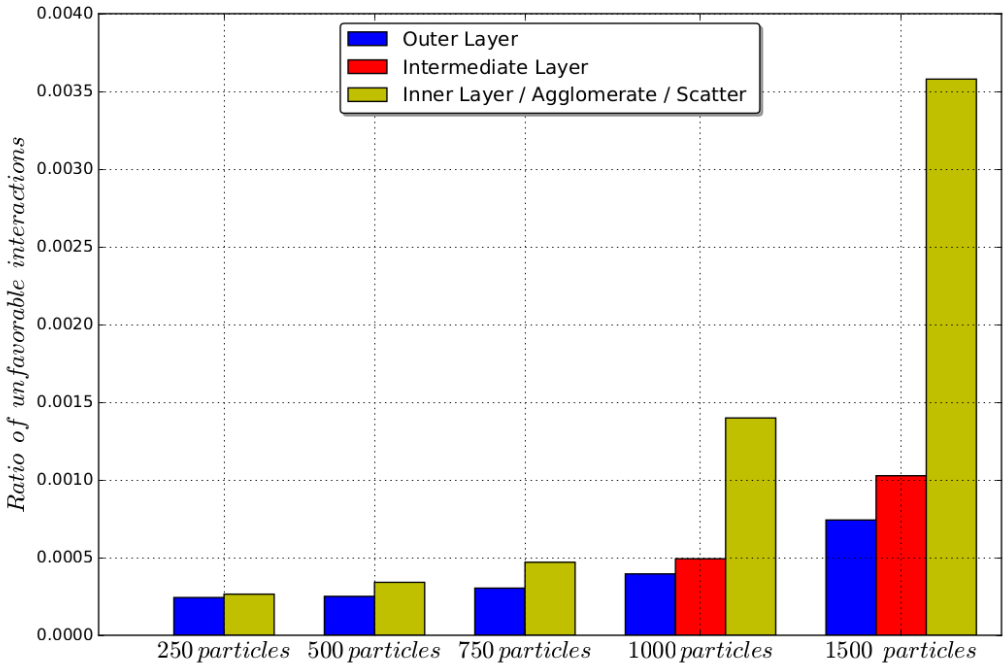

Figure 4.4: *Fraction of H_2-H_2 repulsive interactions with distance less than σ_{HH} in a particular region.*

At this point, it is clear that layers, scatters and agglomerates consist of different

configurations of particles' clusters that occur at different concentrations of particles. But what about the relative positioning of these structures in relation to each other? Why are particles trapped in layers and do not have configurational freedom to fill the free space available inside the SWNT? The answer to these questions is not simple, but we got some insights about it by computing the total potential energy, generated by the combination of the contribution of different structures of the system and of the SWNT, in a probe particle that spans the x axis (the reference frame used has its origin in the center of the SWNT and its z axes is oriented along the SWNT's direction of longitudinal growth). The potential generated by a structure (layer, scatter or agglomerate), expressed in Kelvin, is given by:

$$V_{structure}(r_{Pj}) = \sum_{j}^{N_{particles}} 120[(\frac{3}{r_{Pj}})^{12} - (\frac{3}{r_{Pj}})^{6}] \tag{4.4}$$

where the sum runs over all the particles present in that structure, $N_{particles}$, and the distance, r_{Pj}, is computed using the position of the probe particle P and the position of the particle j, so that $r_{Pj} = ||\vec{r_P} - \vec{r_j}||$, where $\vec{r_P} = (x, 0, 0)$. The same potential cut-off used in the simulations was applied in these calculations. Furthermore, V_{SWNT}, expressed in Kelvin, is given by:

$$V_{SWNT}(r_{Rj}) = 1200[(\frac{3}{r_{Rj}})^{12} - (\frac{3}{r_{Rj}})^{6}] \tag{4.5}$$

where R_j is given by $R_j = R_{SWNT} - r_j$ if $x > 0$ and $R_j = r_j - R_{SWNT}$ if $x < 0$. The distributions used to compute the one-dimensional Potential Energy Profiles (PEP) are represented in figure 4.3. Figure 4.5 represents the PEPs obtained for the simulations where 500, 1000 and 1500 particles were used. With 500 particles, the PEP generated by the $V_{SWNT} + V_{Inner\ Scatter}$ shows that the average position of the outer layer is near the minimum of the PEP. Furthermore, the PEP generated by $V_{SWNT} + V_{Outer\ Layer}$ shows that the potential generated gives rise to a inner region in the SWNT where the well depth is not deep and the function is smooth and negative. This can contribute to the formation of a scatter instead of a layer because although the average position of the inner scatter is placed near the minimum of the profile, its depth well is not deep enough to trap the particles and, therefore, they can disperse and form a scattering. For both PEPs, the small displacements in relation to the equilibrium position can be attributed to fluctuations of the configuration or to the scattered distribution of the inner region of the SWNT. Moreover, for the simulation with 1000 particles, the PEP generated by the $V_{SWNT} + V_{Inner\ Agglomerate} + V_{Intermediate\ Layer}$

shows that average position of the outer layer is near the minimum, and the same is observed for the position of the intermediate layer in the profile generated by $V_{SWNT} + V_{Inner\ Agglomerate} + V_{Outer\ Layer}$. Nevertheless, for the PEP generated by $V_{SWNT} + V_{Outer\ Layer} + V_{Intermediate\ Layer}$, the inner agglomerate is positioned at an unfavorable region of the energy profile, maybe because the zone of the plot where the potential energy is less than zero is very near the center ($|x| < 2$). If a layer were formed in this zone, it would have a very small radius. Consequently, the volume available for each particle would be very small, resulting in a very unfavourable situation. Finally, for the simulation with 1500 particles, the three PEPs generated show that the average positions of the outer, intermediate and inner layer are near the minimum. It is also worth to mention that the slight asymmetry of these PEPs is attributed to fluctuations of the distribution used to generate it. This can be seen in figure 4.3, where the distribution of particles of the inner and intermediate layers is slightly disrupted for $x > 0$.

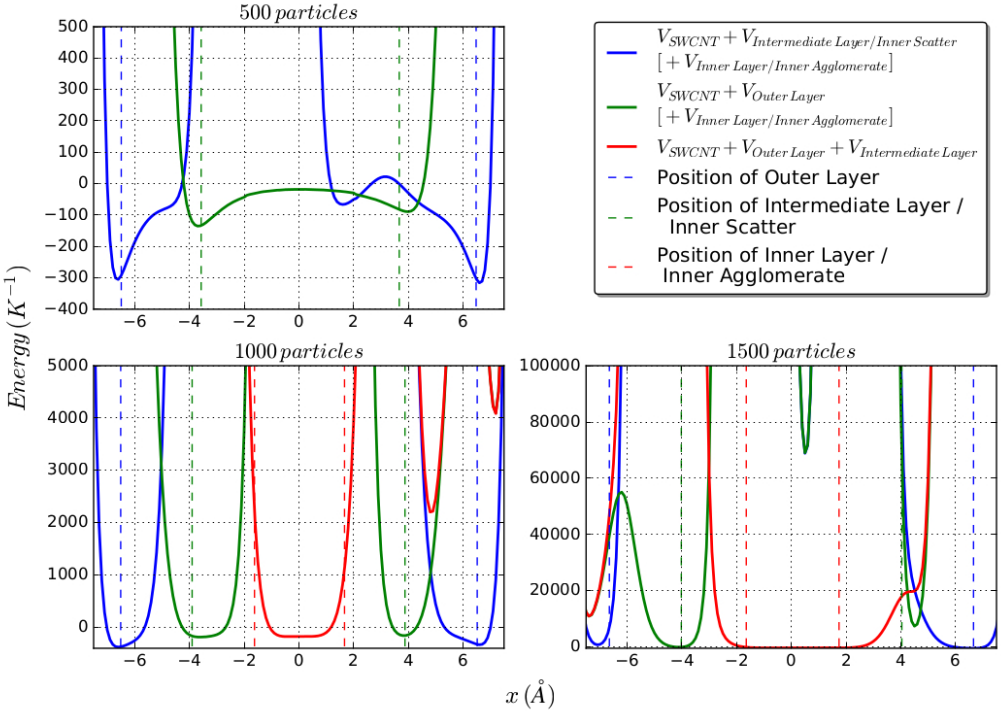

Figure 4.5: *Potential Energy Profiles (PEPs) of the simulations with* 500, 1000 *and* 1500 *particles. The distributions represented in figure 4.3 were used. The energy contributions to the potential energy enclosed in square brackets are only applied to the simulations with* 1000 *and* 1500 *particles. The position of the layers corresponds to the average value of* x, $\langle x \rangle$.

From the results obtained previously, it is possible to conclude that the formation of the outer layer is mainly caused by the interaction between the particles and the SWNT's wall, whereas the inner layers are mainly a consequence of the interaction between the particles themselves. One can think of a layer of particles as a "wall" of hydrogen molecules, just like we considered in a certain sense the SWNT's wall as a layer of carbon atoms (even keeping in mind that, in this work, the SWNT wall is not discretized in their individual atoms). Hence, the formation of layers is a consequence of the positioning of the particles near the minimum of the potential energy function generated by the other structures. It also implies the internal reorganization of particles in order to minimize repulsive interactions. If the formation of layers is not observed, it might mean that the enthalpy gains were not enough to compensate the entropy loss and, therefore, the system prefers to form agglomerates or scatters of particles. In other words, one can consider that the formation of layers happens whenever the enthalpy profit overcomes the entropy loss and that they are associated with large SWNT's loadings of particles.

Finally, the results obtained for the D_s are shown graphically in figure 4.6. There is a linear dependence of the D_s in the range of hydrogen concentrations used. Such dependence is typical of the Brownian motion diffusive regime. In order to better understand these results, a study of the gas molecules' mobility in different sections of the SWNT was done. The results are shown in the next section.

4.3.2 Mobility of Different Zones in the SWNT

In order to study the H_2 mobility in different zones of the SWNT, multiple measurements were done on each colored area represented in figure 4.3. For the simulations with 250, 500 and 750 particles, only two different zones of the SWNT were considered: the outer layer (7.3Å $< r <$ 5.5Å) and the inner scatter ($r <$ 5.5Å). Furthermore, for the simulations with 1000 and 1500 particles, three different zones were considered: the outer layer (7.3Å $< r <$ 5.5Å), the intermediate layer (5.5Å $< r <$ 2.8Å) and the inner scatter/agglomerate ($r <$ 2.8Å). The parameters evaluated for each zone of the SWNT as an arithmetic average over 2×10^4 cycles were the total number of particles (n), the number of accepted displacements ($n_{displacements}$) per cycle, and the total square displacement done by the particles (Δr^2_{total}). By combining these parameters, we obtain the ratio of accepted displacements over the total number of attempted displacements ($n_{displacements}/n$), the square displacement done in each accepted movement ($\Delta r^2_{total}/n_{displacements}$), the average square displacement ($\langle \Delta r^2_{total} \rangle = \Delta r^2_{total}/n$) -

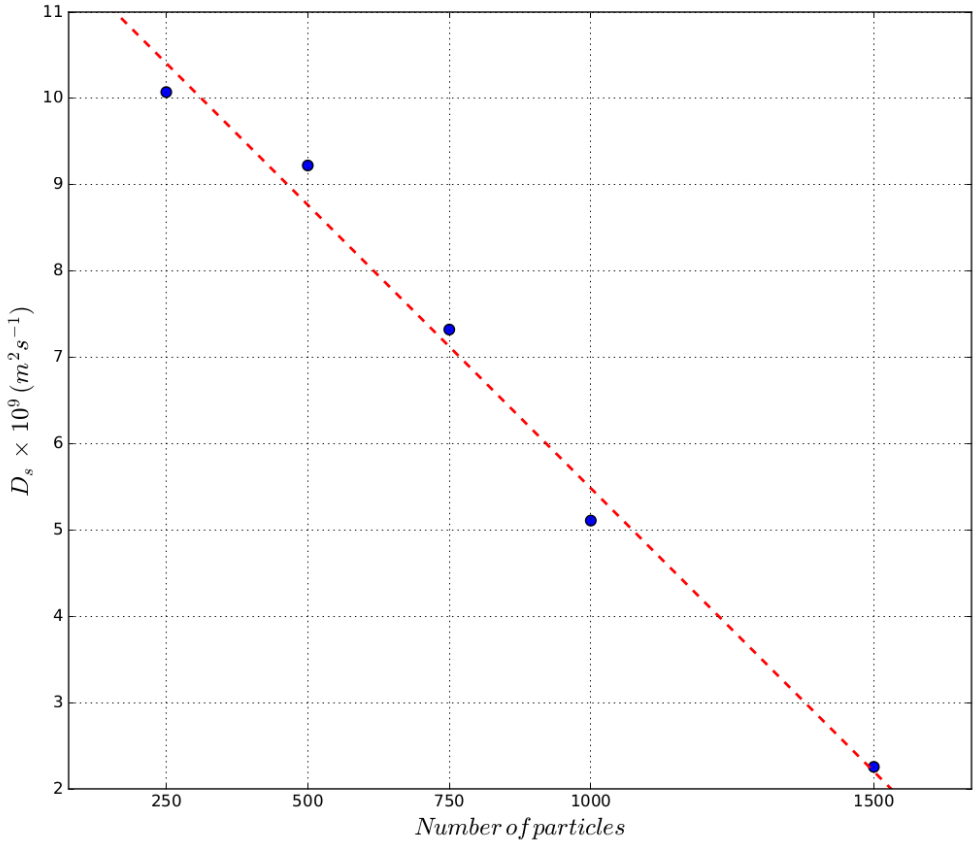

Figure 4.6: *D_s as a function of the number of particles used for simulations where the influence of concentration was studied. The results show that there is a linear dependence of Ds on the concentration of hydrogen: the linear regression is* $D_s(n) = -0.0065652865(n) + 12.0485891892$ *with a* $R^2 = 0.9875$*. The standard deviations are not represented because they are not visible in the scale used.*

which corresponds to an ensemble average - and the density of particles in that zone ($\rho = n/V_{zone}$). The results obtained are shown in table 4.2, where it is possible to identify zones of the SWNT with higher mobility and the reason why this happens. First of all, it is possible to conclude that the outer layer is the zone that retains more particles and has higher density of particles. This layer is positioned in the most outer zone of the SWNT where particles can be placed without feeling the repulsions from the SWNT's wall. This corresponds to the zone where deep potential well generated by the SWNT is placed. Therefore, it is reasonable to say that the adsorption layer is a consequence of the strong and smooth attractive potential felt by the molecules in that

region. Various studies have reported the formation of these structures [22, 42, 38]. Furthermore, it can also be seen that the number of particles at the inner zones of the SWNT (inner scatter, intermediate layer and inner layer/agglomerate) decreases as we approach the axis of the SWNT.

It is of great importance in this work to establish what mobility means in terms of the D_s. There are two main parameters that contribute to the mobility: the number of accepted displacements over the total number of displacements ($n_{displacements}/n$) and the square displacement done in each accepted movement ($\Delta r^2_{total}/n_{displacements}$). These two parameters can be related through the product between them, which gives the ensemble average $\langle \Delta r^2 \rangle$. This value can be used as a real measurement of the mobility in a specific zone, since it is directly related to the D_s, with $1/6t$ being the proportionality constant between them (6 comes from the dimensionality of the system and t is the time). Therefore, one can consider that the higher $\langle \Delta r^2 \rangle$, the higher will be the mobility in a certain zone. In this treatment, the contribution to the mobility of particles which skip from a zone to another was neglected due to the very low probability of acceptance of these displacements.

For the simulations where 200, 500 and 750 particles were used, the inner scatter is a zone with more mobility than the outer adsorbed layer. Moreover, comparing the mobility of same zones in these three simulations, it is clear that the higher the density of particles in a certain region, the lower is the ratio $n_{displacements}/n$ because the probability of a particle being placed near another is higher and, therefore, the acceptance probability of the movements occurring in this region is lower. Concomitantly, $\Delta r^2_{total}/n_{displacements}$ is higher at regions of lower density because there is more free space available. Furthermore, for the simulations where 1000 and 1500 particles were used, it can be concluded that the intermediate layers have higher mobility in relation to the outer layer mainly due to their lower density. It is also interesting to see that if the inner region is a scatter of particles (1000 particles), the density of particles is lower than when an inner layer is formed (1500 particles) and, therefore, the mobility of the latter is lower.

In conclusion, the three main properties of a distribution that explain the D_s obtained are: regions where layers are formed rather than scatterings of particles have higher density and, therefore, lower mobility; the higher the number of layers formed the lower the overall mobility; if multiple layers are formed, inner layers have higher mobility than the outer layer.

Table 4.2: *Mobility in different zones of the SWNT. The measured quantities are the number of particles in each zone (n), the number of accepted displacements per cycle ($n_{displacements}$), the total square displacement done (Δr^2_{total}, Å^2), the ratio of accepted displacements over the total number of displacements ($n_{displacements}/n$),the square displacement done in each accepted movement ($\Delta r^2_{total}/n_{displacements}$, Å$^2 mov^{-1}$), the average square displacemenent ($\langle \Delta r^2 \rangle$, Å^2) and the density of particle (ρ, Å^{-3}).*

Section	n	$n_{displacements}$	Δr^2_{total}	$\frac{n_{displacements}}{n}$	$\frac{\Delta r^2_{total}}{n_{displacements}}$	$\langle \Delta r^2_{total} \rangle$	ρ
250 Particles							
Outer Layer	209.599	101.136	56.290	0.487	0.551	0.268	0.014
Inner Scatter	35.331	27.843	34.504	0.788	1.239	0.976	0.002
500 Particles							
Outer Layer	380.842	165.122	65.459	0.434	0.396	0.172	0.026
Inner Scatter	111.758	75.152	74.018	0.672	0.985	0.662	0.006
750 Particles							
Outer Layer	510.404	194.975	54.373	0.382	0.278	0.106	0.035
Inner Scatter	232.756	126.599	81.582	0.544	0.644	0.350	0.012
1000 Particles							
Outer Layer	626.444	206.469	39.073	0.333	0.189	0.062	0.043
Intermediate Layer	271.742	109.032	31.228	0.401	0.286	0.115	0.019
Inner Agglomerate	89.681	37.353	11.509	0.417	0.308	0.128	0.018
1500 Particles							
Outer Layer	852.917	192.318	14.177	0.225	0.074	0.017	0.059
Intermediate Layer	483.474	118.405	10.322	0.245	0.087	0.021	0.034
Inner Layer	161.833	38.660	3.254	0.239	0.084	0.020	0.033

4.3.3 Influence of Length, L

In order to study the influence of the length of the SWNT on the self-diffusivity coefficient of molecular hydrogen, three simulations were performed with different lengths but keeping constant the radius (R=10Å) and the concentration H_2 (the number of particles was varied proportionally to the length of the cell). The reference concentration, 0.0307 particles per Å^{-3}, corresponds to 1000 particles in a simulation cell with length $L = 200$Å and effective radius $R = 7.2$Å. The effective radius is used to take into account the volume that hydrogen molecules effectively occupy inside the SWNT (figure 4.7).

Accordingly, the number of particles used in the simulations were: 250 ($L = 50$Å), 500 ($L = 100$Å) and 750 ($L = 150$Å). Figure 4.8 depicts the distribution of particles on a projection plane perpendicular to the longitudinal axis of the SWNT, after 2×10^5 displacement attempts, and figure 4.9 represents the respective radial distributions

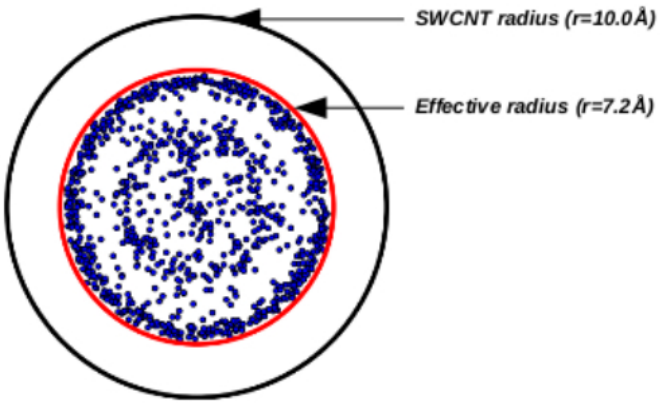

Figure 4.7: *Illustration of the difference between the SWNT's radius and the effective radius.*

functions (RDFs). The profiles of the RDFs show that the simulations were performed at the same concentration as the one defined as reference ($L = 200$Å). Furthermore, it can be seen that they are all formed by an outer layer, an intermediate layer and an inner scattering of particles. Note that the distributions of figure 4.8 are projections of different volumes.

The D_s obtained for these simulations are all very similar (see table 4.1), being their average value $(5.12 \pm 0.01) \times 10^{-9}\ m^2 s^{-1}$. The D_s does not depend on the length of the simulation cell as long as periodic boundary conditions are applied along the z direction (the direction of the growth of the SWNT's length), which means that, in practice, the simulation considered a SWNT with infinite length. This is a confirmation that the diffusivity regime we are studying corresponds to a Brownian motion, since a characteristic of this regime is that its mobility does not depend on the SWNT's length.

4.3.4 Influence of Radius, R

In order to study the influence of the radius of the SWNT on the self-diffusivity of H_2, four simulations were performed with radii 5.0Å , 7.5Å , 15.0Å and 20.0Å. All the simulation cells had the same length, $L = 200$Å, and different numbers of particles were considered to keep constant the concentration. Taking as reference the concentration used in the previous section, the number of particles considered in each simulation was: 94 ($R = 5.0$Å), 426 ($R = 7.5$Å), 2871 ($R = 15.0$Å) and 5706 ($R = 20.0$Å). Figure

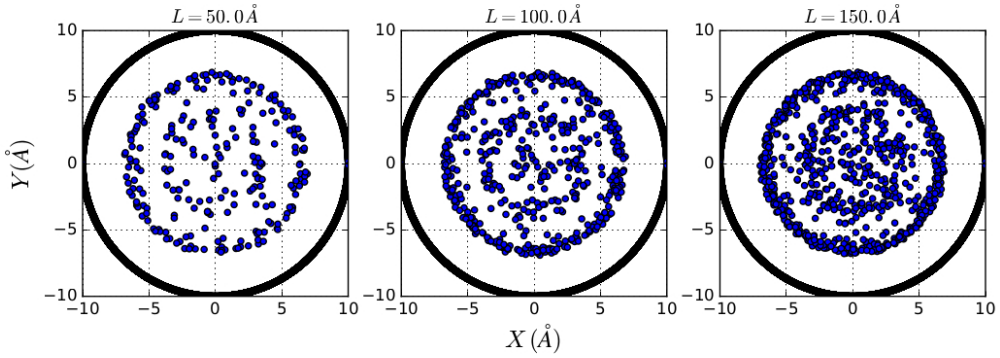

Figure 4.8: *Distribution of particles on projection plane perpendicular to the longitudinal axis of the SWNT. The simulations were performed using always the same radius,* R=*10Å, while varying the number of particles and the length in order to keep the particle concentration constant.*

4.10 represents the distribution of particles on a projection plane perpendicular to the longitudinal axis of the SWNT, where relevant zones are highlighted with different colors.

It is possible to observe that in the narrowest SWNT ($R = 5.0$Å), only a single layer was formed at a distance from the nanotube wall ca. 3Å. In the SWNT $R = 7.5$Å, an outer layer was formed as well along with an inner agglomerate of particles around the perpendicular axis of the SWNT. Finally, for wider nanotubes, $R = 15.0$Å and $R = 20.0$Å, three regions were observed. Besides the outer layer, it is possible to observe an intermediate one is also formed and a uniformly distributed scatter around the SWNT axis.

The results obtained for the D_s are shown in table 4.1. Furthermore, in figure 4.11, the D_s values calculated for different regions of the SWNT are shown, as well as the particle density. These values were obtained after 1×10^4 cycles, using the equilibrated distributions of figure 4.10. It is possible to see that D_s $(Outer\ Layer) < D_s$ $(Intermediate\ Layer) < D_s$ $(Inner\ Scatter))$, which indicates that mobility in different regions decreases with the distance to the axis of the nanotube. There is a good agreement between the conclusions previously stated and the results now obtained; *i.e.* within each simulation, regions where layers are formed, rather than scatterings

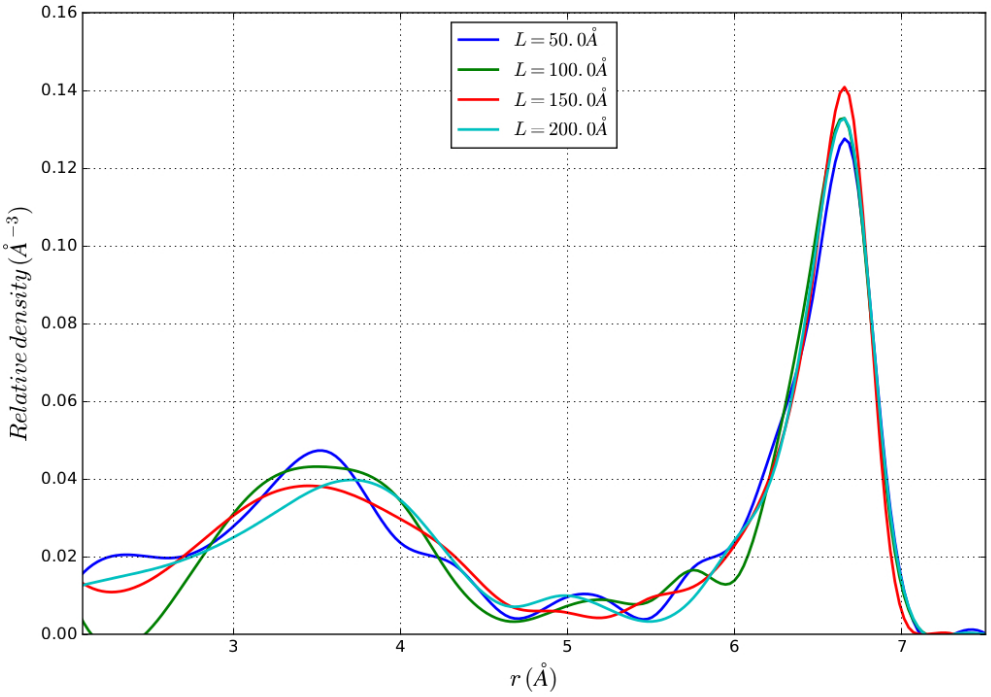

Figure 4.9: *Radial distribution functions for the simulations performed in order to study the influence of the SWNT's length. It can be seen that the relative density is very similar in all cases, which is a confirmation that we are using the same concentration of particles in all simulations.*

of particles, have higher density and, therefore, lower mobility. Furthermore, although the densities of the intermediate layers are larger than those of the inner scatters, the differences are not large enough to justify the discrepancies of the coefficients. A factor that can contribute to the difference in mobilities is the internal organization of each structure that, as it was seen before, gives rise to different percentage of unfavorable interactions. Hence, since such value is higher in scatters than it is in layers, the probability of a large displacement being accepted in a scatter is larger. The reason for this is that in scatters, H_2 molecules with unfavorable interactions have larger free space available where they can be displaced to. On the other hand, since layers are highly organized structures in equilibrium, the particles tend to perform rather short displacements that generally don't shift the configuration far from the previous one.

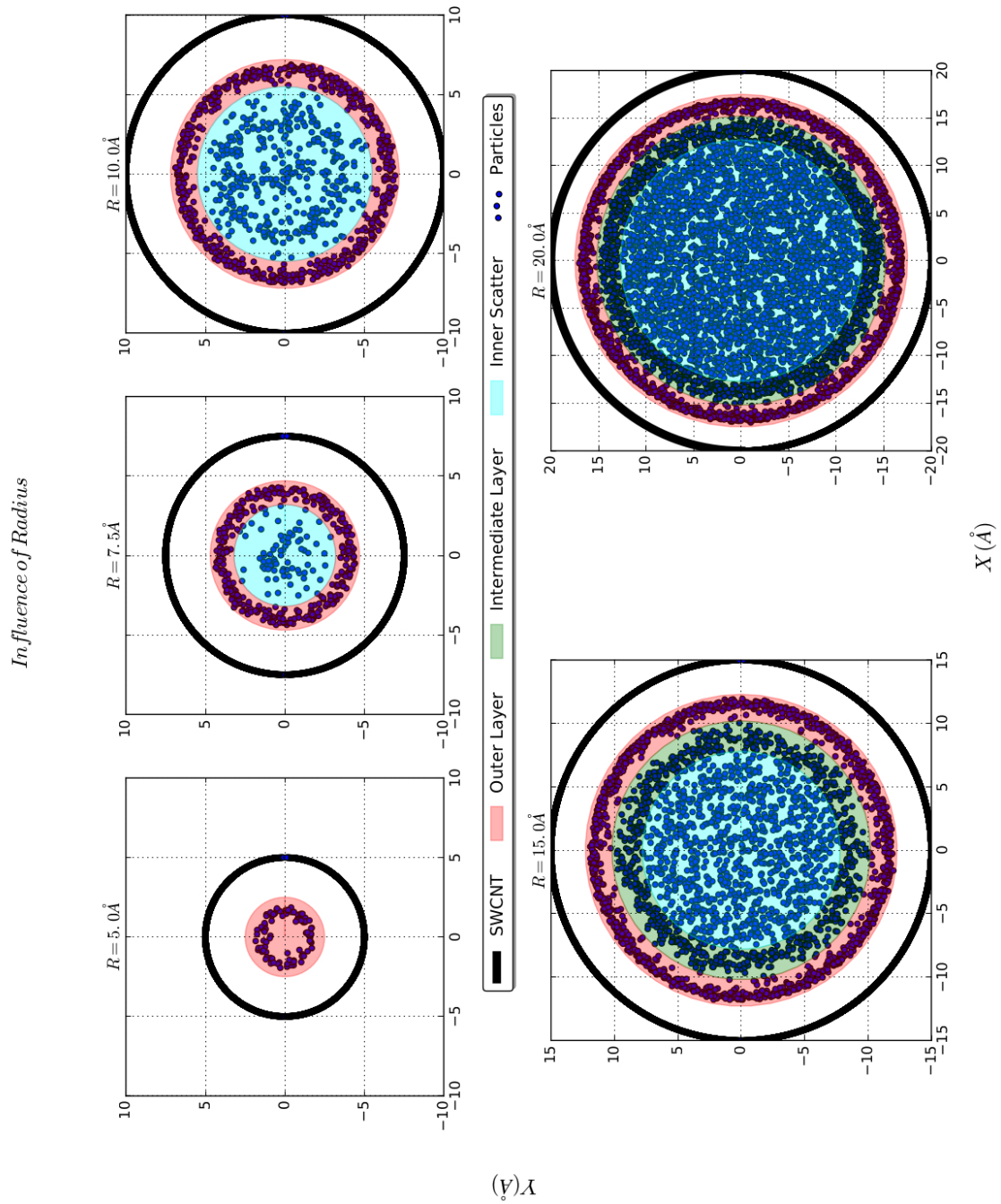

Figure 4.10: *Distribution of particles on a projection plane perpendicular to the longitudinal axis of the SWNT. The simulations were performed using always* $L =$ 200Å*, while varying the number of particles and the radius, in order to keep the particle concentration constant. Relevant zones are highlighted with different colors.*

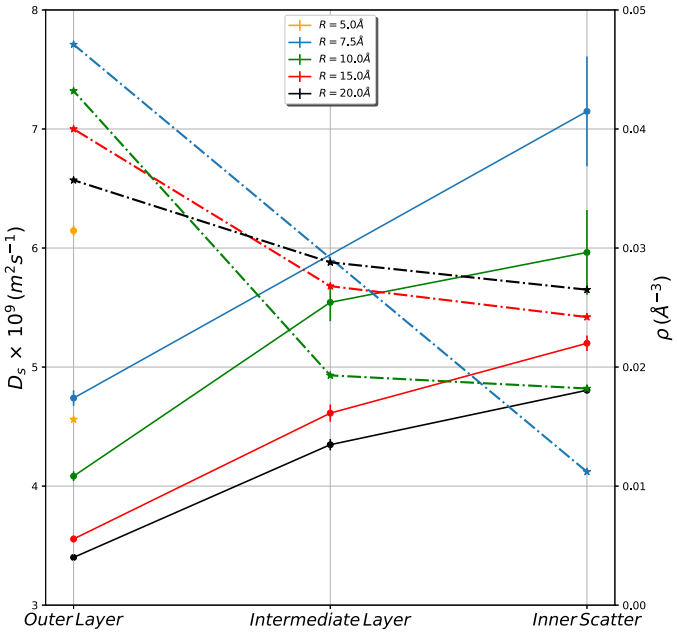

Figure 4.11: *D_s for the highlighted regions of the SWNTs of figure 4.10 (solid lines). The standard deviations are represents as error bars. In some cases, the error bar is smaller than the symbol and, therefore, not visible.The density of particles in each region is represented by dashed lines.*

4.3.5 Influence of Aspect Ratio, R/L

The last set of simulations aimed to study the effect of the R/L ratio on the self-diffusion coefficient, while keeping constant the number of particles. Five simulations were performed where the number of particles was fixed at 1000 and the R/L ratios -, 5.0Å /2142.0Å , 7.5Å /469Å , 15Å /70Å and 20Å /35Å ,- were determined using the reference SWNT concentration.

The results are identical to those of the study of the radius influence, as can be seen in figure 4.12. This happens because the simulations done in Sec. 4.3.3 had already demonstrated that the self-diffusion is independent of the length of the SWNT, whenever periodic boundary conditions are imposed along the direction of its longitudinal growth. Hence, if the value of D_s is independent of the length, the only variable left with impact on it is the SWNT radius. Because of this, these simulations are equivalent to the previous ones and, therefore, the conclusions of the previous section

can be extrapolated for this one.

Finally, in this last set of simulations, a SWNT with an aspect ratio of 3.5Å /21159Å was also considered in order to study the impact of extremely small radius in the self-diffusivity. It is worth to mention that this SWNT was not included in the previous set of simulations because it would consist of a simulation of only 10 particles, a number too small to ensure statistical accuracy. In figure 4.12, it is possible to see that D_s for this SWNT does not follow the trend obtained for the other values. This happens because the small radius imposes single-file diffusion along the z direction (along the length of the SWNT), due to constrains in the other two directions, which strongly limits the mobility of the particles in the nanotube.

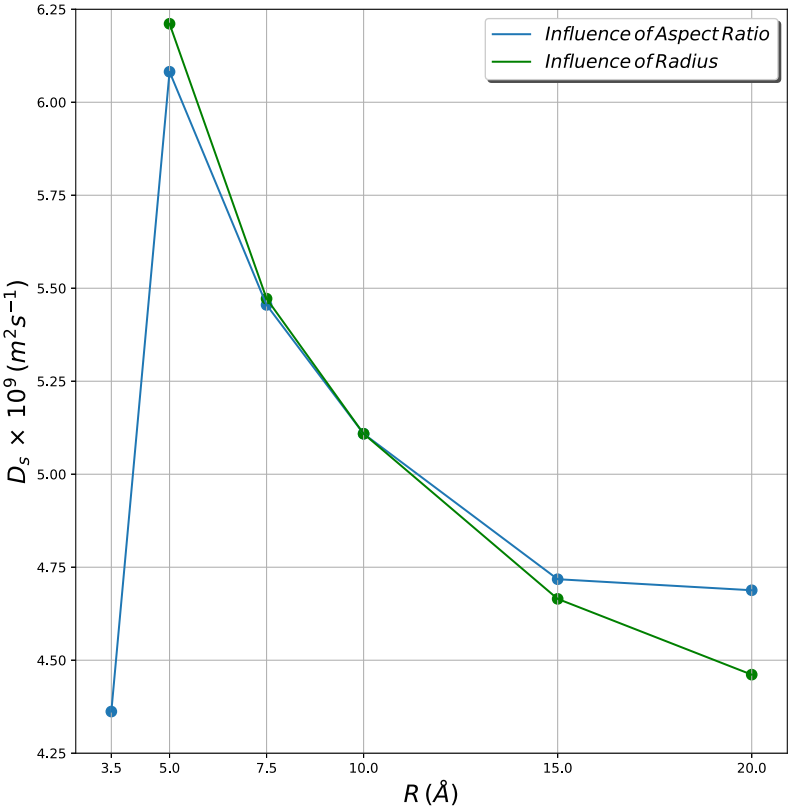

Figure 4.12: *Comparison between the self-diffusion coefficient (D_s) values obtained for the influence of aspect ratio (R/L) and for the influence of the radius.*

4.4 Conclusions

We have implemented a KMC algorithm to investigate self-diffusion of H_2 molecules inside SWNTs with different geometrical parameters and at various tube loadings. Our model takes into account H_2-H_2 and H_2-SWNT interactions. The way the code is written permits to easily include further interactions and also include other type of potentials, *e.g.* intra-molecular potentials, if needed. Furthermore, the code uses idealized models for the SWNT (a continuous cylinder) and a mass point for the H_2 molecule.

The results have shown that the self-diffusion coefficients inside ideal SWNTs are of the order of magnitude of 10^{-8} to 10^{-9} m^2s^{-1}. A typical diffusion coefficient for a molecule in the gas phase is in the range of 10^{-6} to 10^{-5} m^2s^{-1}, whereas diffusion in liquids is far slower, with typical diffusion coefficients within the range of 10^{-9} to 10^{-10} m^2s^{-1}. Finally, the diffusivity in glassy polymers drops to values between 10^{-13} and 10^{-14} m^2s^{-1}. [40, 112, 100]

It is difficult to compare the effective self-diffusivities obtained in simulations with experimental values mainly because experimental techniques and conditions might cause variation in coefficients up to three orders of magnitude [85]. Nevertheless, good agreement was obtained in experimental studies that report simulations at similar conditions: quasielastic neutron scattering (QENS) experiments where the self-diffusion of H_2 and D_2 inside Takeda 3Å carbon molecular sieves was measured gave results with order of magnitude of (10^{-8}-10^{-9}) m^2s^{-1} for the range of temperature 30-140K and with a particle loading of $0.05 mmol/g$[77]. Furthermore, QENS was also used to obtain the self-diffusion coefficient of H_2 in the Carbolex SWNT (tube radius between 6-7.5Å) giving a value of 8.92×10^{-8} m^2s^{-1} at 77 K with an adsorbed H_2 wt % of 0.5 [73]. Furthermore, KMC simulations of CH_4 in SWNTs with 20Å of radius reported values between (6.5-1.5) $\times 10^{-9}$ m^2s^{-1}, using a temperature of 267K and a pressure range of 1 to 8atm. The same author also reports KMC simulations studying the anisotropic diffusion of hydrogen in nanoporous carbons, obtaining self-diffusion coefficients with a order of magnitude of 10^{-8} m^2s^{-1}[86]. Therefore, both experimental and theoretical results seem to indicate that similar order of magnitudes for the self-diffusion coefficient are obtained. It is worth mention that this work only reports self-diffusion coefficients for the Brownian motion, without the inclusion of other diffusivity regimes in motion description. Hence, the fact that we obtain a theoretical value one order of magnitude lower than the experimental values can be an indication that in these experiments other diffusivity regimes were contributing to the diffusion coefficient. Nevertheless,

the agreement is quite good, specially taking into account the simplicity of the model created.

Finally, in view of the results obtained, the following conclusions can be drawn: for the range of loading of particles used, the self-diffusion coefficient has a linear dependence on the concentration of H_2, which can be explained by the lower mobility associated with higher densities of particles; formation of layers occurs whenever the enthalpy gains overcome the entropy penalty and these structures have higher densities in comparison with scatterings and agglomerates of particles; the self-diffusion coefficient does not depend on the length of the SWNT as long as periodic boundary conditions are imposed along the direction of growth of the nanotube, which is a confirmation of the validity of our model; large radii give rise to particle distributions that overall have smaller mobility than the ones obtained with small radii, although very small radius may restrict the diffusion to just one dimension (single-file diffusion), which is unfavourable for the diffusion.

Chapter 5

Phase Transitions

One aspect that is clearly intertwined with both aspects so far investigated (*i.e.* adsorption and diffusion), regards the aggregation states of the hydrogen, when it is confined or adsorbed in such minimal spaces. From the energetic point of view, the existence of an ordered phase implies a low entropy zone in the configurational space, which could exert its influence on molecules by reducing their degrees of freedom. The result could be, for instance, a reduced mobility, or an increase or decrease of the adsorption. Moreover, confined spaces also mean some symmetry restrictions which could possibly promote or destabilize ordered configurations.

We adopt two important tools widely employed for studying phase transitions, namely GE simulations and the recent TM method. The latter has been successfully used for simulating triangle-well fluids into slit pores[92]. Furthermore we investigate different systems, from graphite systems (where an ordered-disordered phase transition has already been object of investigation[109]), to the hydrogen adsorbed layer inside CNTs.

5.1 Simulations details

5.1.1 Gibbs ensemble

The GE scheme comprise two independent simulation boxes, one for each phase, able to exchange molecules with a given probability which, in our case, is 40%. The disordered phase box contain 381 H_2 molecules, while the ordered one has 100 H_2 with sections of, respectively, 23.7x10^{3}Å^2 and 2.9x10^{3}Å^2. In both cases molecules are confined between

a graphite surface and a hard wall which force them within a 3.8Å space above that surface, but leaving them free to spread in the plane.

Graphite systems are well approximated by the 10-4 − 3 Steele potential [103]:

$$V_{Steele}(z) = 2\pi\rho_s\Delta\sigma^2\varepsilon\left[\frac{2}{5}\left(\frac{\sigma}{z}\right)^{10} + \quad \cdots \right.$$
$$\left. \cdots \quad -\left(\frac{\sigma}{z}\right)^4 - \left(\frac{\sigma^4}{3\Delta(z+0.61\Delta)^3}\right)\right] \tag{5.1}$$

which simulate an infinitely wide graphite surface made by infinite homogeneous graphene sheets stacked at distance Δ, being ρ_s the carbon atom density; σ and ε have the same meaning of the LJ potential. Parameters are shown in table 5.1.

For preventing hydrogen aggregation in the disordered phase, the Aggregation Volume Bias (AVB) algorithm[14], already implemented in *towhee* software, has been applied. Because of its enhanced efficiency, we actually choose one of its improved version[13], which attempts to displace a molecule from its position, close to a target molecule (both chosen randomly), to any point of the space outside that region or vice-versa. The two events occur with relative probability of 0.75 and 0.25, respectively and the size of the region assumed as the surroundings of the target molecule was set to 5Å. This mechanism, therefore, generates a tendency to rapidly dissolve every aggregate eventually formed during the simulation, but it also implies that the condensed phase is easily dispersed as soon as the conditions permit.

Hydrogen molecules are interpreted as one-centre particles while the graphite surface is treated using the 10-4-3 Steele wall[103]. We apply the parameters of each one of the three example potentials of table 3.1 looking for any difference in hydrogen behaviour. Both phases of the simulations (equilibration and production) run for 10^4 cycles; a cycle is a number of steps equal to the total molecules in the system.

To properly simulate infinite graphene sheets by means of periodic conditions, the boxes need to follow the symmetry of the graphite lattice unit cell. In other words the axis X and Y should be both orthogonal to Z, the axis along which graphene planes stack, while the angle between them is only 60°. Such level of detail nevertheless is not needled in our simulations, because the interaction potential is not atomistic and therefore could be hypothetically cut in any shape; in future simulations this feature could better adapt to the symmetry of the ordered phase (which could not be exactly the same of the atomistic structure of carbon atoms). The length of the carbon bond in graphite structures is usually 1.421Å, which leads to the average density ascribed in the note of table 5.1.

system	ε / K	σ / Å	eq.	type	ref.
$H_2 \cdots H_2$	34.2	2.96	(5.2)	1-centre	[[8]]
CNT	42.94	3.0	(5.2)	atomistic	[[99]]
graphite	42.75	2.97	(5.2)	atomistic	[[109]]
graphite	42.94	3.0	(5.1)[1]	average	[[99]]

[1] $\rho_s = 0.3817\text{Å}^{-3}$; $\Delta = 3.35\text{Å}$

Table 5.1: *Simulation potential parameters.*

Because of the AVB mechanism, we actually test the stability of the ordered phase. In fact, as soon as the conditions are met, the phase dissolves and no meta-stable situations are permitted. In these context, the equilibrium involve just the two adsorbed phases, without taking into account the unlikely influence of desorbed molecules.

5.1.2 Transition Matrix

Within *towhee* package, used for running our simulations, only the equation (2.63) is implemented in the GC ensemble[66]. Moreover, it is not allowed to use more than one component so, in order to study hydrogen adsorbed in CNTs, we had to generate CNT-hydrogen interactions by means of an external force field. The external potential, added as a new feature in *towhee* code, aims to exactly simulate the non-bonding interactions of a C atom with the simulated particles. We therefore apply one external field for each atom that would constitute the CNT; each one assumes the form of a 12-6 LJ

$$V_{LJ}(r) = 4\varepsilon \left[\left(\frac{\sigma}{r}\right)^{12} - \left(\frac{\sigma}{r}\right)^{6} \right] \tag{5.2}$$

where the values of ε and σ, respectively the well depth and the repulsion range, are shown in table 5.1.

Concerning the setting of the GC-TMMC, we just recall equations 2.61 and 2.60 from section 2.7.4:

$$\begin{cases} \Pi(\mathbf{S})P(\mathbf{S} \to \mathbf{T}) = \Pi(\mathbf{T})P(\mathbf{T} \to \mathbf{S}) & (2.60) \\ \eta(\mathbf{S}) = -\ln \Pi(\mathbf{S}) & (2.61) \end{cases}$$

The biasing function (2.61) used for the sampling is not known *a priori* but is progressively updated during the simulation. Therefore, directly from equation 2.60, and

assuming $\mathbf{S} = \{N-1\}$ and $\mathbf{T} = \{N\}$, we have:

$$\ln \Pi(N) = \ln \Pi(N-1) + \ln \left[\frac{\mathrm{P}(N-1 \to N)}{\mathrm{P}(N \to N-1)} \right] \tag{5.3}$$

where the probabilities $\mathrm{P}(N-1 \to N)$ and $\mathrm{P}(N \to N-1)$ are found in the collection matrix. We just need to assign a positive value to one of the $\Pi(N)$, (*e.g.* $\Pi(N_{\min}) = 1.0$) and, subsequently, calculate all the others. However, the values of the probabilities stored into the collection matrix are obtained from the standard MC acceptance probabilities of the canonical move (see section 2.7.4). It is thus clear that we cannot have any estimation of $\mathrm{P}(N \to N-1)$ without having reached that state at least once. The result is that the very first sampling of any state is actually unbiased, with the consequence that if the chemical potential is not high enough, some of the energy barriers, needed to reach the dense phase, will be impossible to get through.

Within GC-TMMC simulations one is asked to set the temperature T, chemical potential μ, and minimum and maximum particle number, $N_{\min}$ and $N_{\max}$. The first one is fixed, since we are actually simulating a phase coexistence at a certain temperature, but the other three need further information.

Setting $N_{\min}$ to zero allows covering the whole vapour phase and, moreover, if the $\{N = 0\}$ state is sampled, the ideal gas can be used as a reference state[27]. On the other hand, $N_{\max}$ should be as large as possible to ensure the best covering of the dense phase. Nevertheless, since the algorithm makes use of a biasing function to sample even the most unfavourable states with increased probability (as explained in section 2.7.4), the larger the $N_{\max}$ is, the largest number of steps are needed to reach an efficient covering. Usually, $N_{\max}$ is chosen just sufficient to make the ratio of the highest probability in the dense phase, $[\Pi(N)]_{\max}$, to the probability of observing the maximum number of particles, $\Pi(N_{\max})$, be higher than a specified tolerance.

$$\frac{[\Pi(N)]_{\max}}{\Pi(N_{\max})} \geq \text{tolerance} \tag{5.4}$$

Short test simulations are easily run to confirm whether this condition is accomplished or not.

The requirement of equation 5.4 ensures that we are sufficiently far from the peak and we are not discarding relevant parts of the distribution. Thus, $N_{\max}$ and μ cannot be chosen independently because the position of the peak in the particle number distribution actually depends on the chemical potential.

Moreover, at high densities, the system does not easily change its conformation, resulting in a poor sampling. To overcome this problem we executed a 2-stage procedure

(or 3-stage if we also take into account the short simulations needed to select the most suitable chemical potential). In the first one, we run a long simulation over all possible densities, in order to obtain a reasonably good probability estimation. In the second stage, we run for the same total number of simulation steps, but dividing it into multiple consecutive simulations which continue to store data into the *transition matrix*, and starting each time from the zero density. This approach resembles a visited states method, applied to each conformation: the most favourable ones in fact have higher chance to happen during a simulation and thus their contribution is actually higher. We try to split the simulation as much as possible, with the only restriction that each one should have enough steps to sample the entire space. If the probability estimation from stage 1 is good enough, all simulations of stage 2 could run in parallel.

Our work has been developed upon two different systems: a free box containing only hydrogen and a Single Walled carbon Nano Tube (SWNT).

free hydrogen

Free hydrogen simulations were performed in order to either optimise the procedure and provide some reference results. For this reason, we chose a system equivalent to the one previously used[27]. The box is, therefore, cubic and its length is, in units of the hydrogen repulsion range, $L/\sigma_{HH} = 7$. Periodic boundary conditions are, of course, applied to each axis.

carbon nano-tubes

Finally the SWNT system is the inner pore of an isolated (26,0) zig-zag type. The nanotube is considered infinitely long due to periodic conditions along its axis (Z). Particles are then confined into the inner pore by means of a probability map which divides the simulation box into smaller spaces and attribute to each one a probability of molecules being created or moved therein. Since we do not intend to bias our system, but just to forbid some areas to be sampled, we only apply a binary map (1 where the molecule is permitted and 0 where is not), leaving any further decision to the standard Metropolis algorithm[69].

Differently from the previous case, all SWNT atoms are explicitly considered in the simulation. Isolation of the nanotube is produced by pulling the limits of the box away from the CNT surface more than half the value of cutoff range (fixed at 9.5Å): the box dimension in the XY plane is therefore chosen to be 30Å which ensures such

condition.

In this case, carbon bonds are 1.418Å long and five ring units produce a total length of 21.27Å in the axis Z.

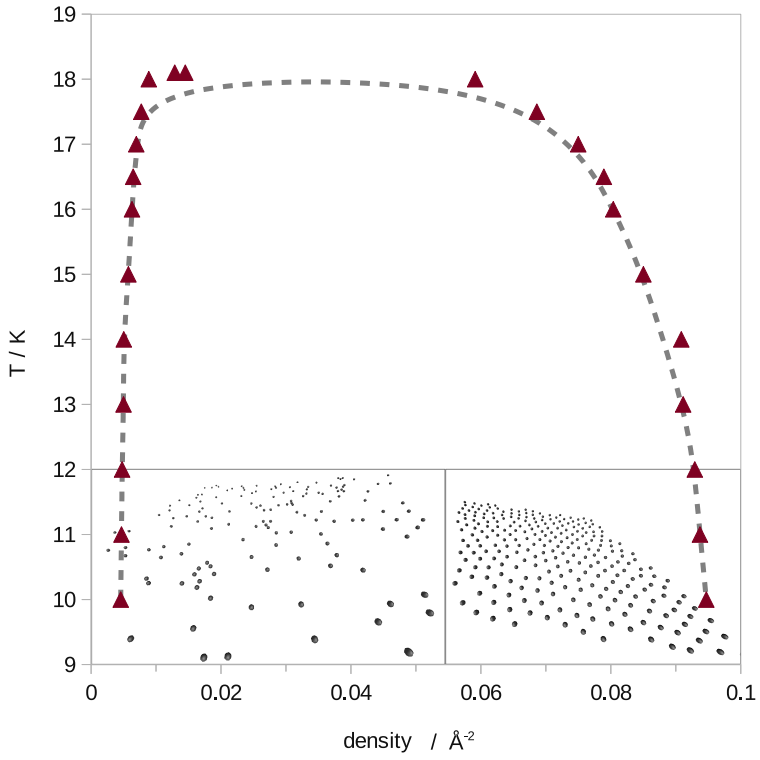

Figure 5.1: *Ordered-disordered phase diagram for H_2 adsorbed on graphite surface from GEMC simulations; snapshots of the two phases are presented in the insets.*

5.2 Results

The first case under investigation was an ordered disordered phase transition occurring between hydrogen particles adsorbed on a graphite surface. Figure 5.1 represents the temperature vs. density phase diagram for the two phases, simulated with the Wang-40 potential: the 2-phase system is found stable up to $18K$ and densities are consistent with the data reported by Wang *et al.*[109]. Beyond $18K$ the ordered phase dissolves and both simulation boxes show the same density. For the sake of completeness, simulations have also been performed with the potentials of table 3.1, which led exactly to the same results. We can conclude that, in this case, the interaction with the surface

acts just as confinement reducing the degrees of freedom of the molecules and thus promoting the phase transition. In any other case we should have seen some kind of consequences when tuning the strength of the potential applied.

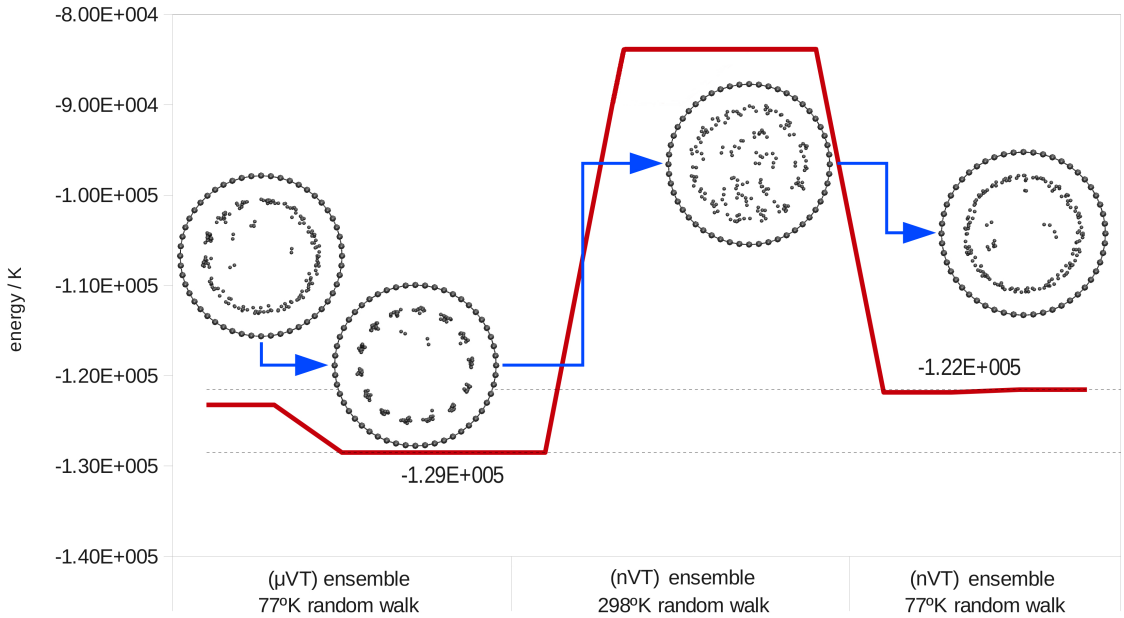

Figure 5.2: *Stability of the different conformations.*

Before calling the TMMC method into action, we were interested in the stability of an ordered phase inside the system we are investigating: a (26,0) SWNT. Hence, a *pseudo-anealing* sequence has been performed and shown in figure 5.2. Previous tests suggested an ordered conformation which occasionally resulted from GC simulations at $77K$. We have first tested the stability of this conformation by merging it with a completely homogeneous one (obtained from $77K$ GC as well): what has been observed was a seed effect so that, in the presence of small ordered zone, inevitably led to the full ordered conformation. We have then run canonical simulations at $298K$ in order to fully dismantle any trace of the ordered structure and then let the system settle back at $77K$. The simulations were run with constant particle number, *i.e.* without the creation-deletion of particles. What has been obtained is a homogeneous layer in the inner side of the CNT, a quite stable state, because in this conditions the canonical simulation only sample states of such kind. An interesting data is the energy difference between such conformation and the ordered one, which clearly shows the higher stability of the latter.

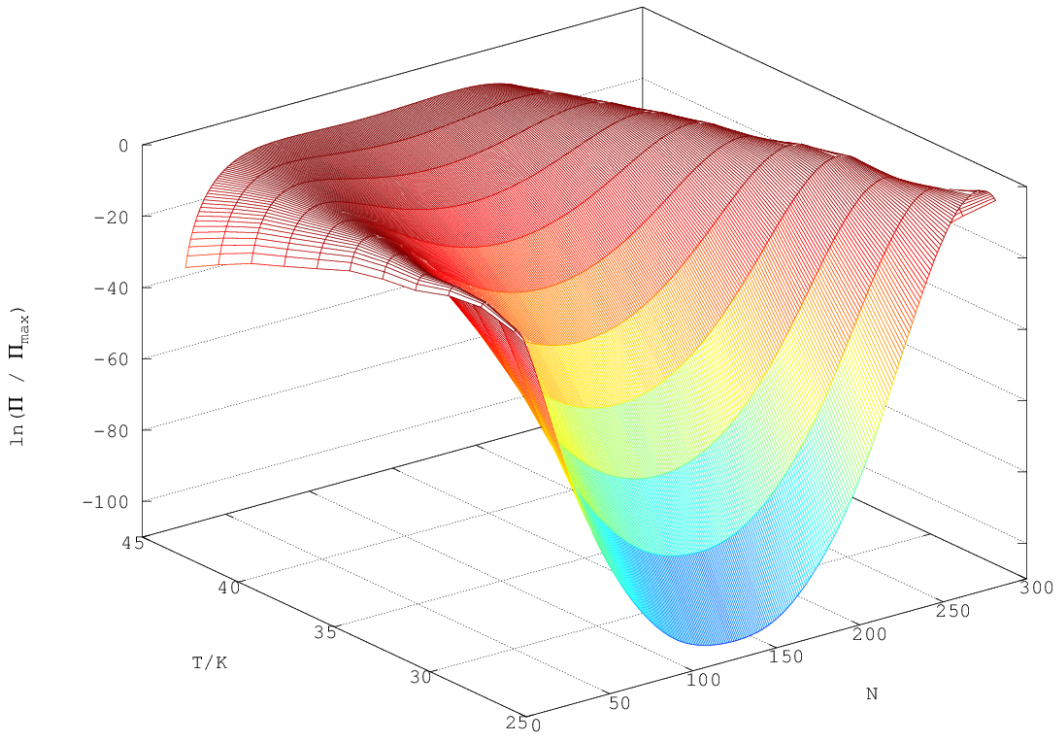

Figure 5.3: *TM results of free hydrogen simulations, 1-centre model. The vertical axis as well as the color represents the relative probability of that state (*i.e. *density or particle number) to happen at that temperature.*

The TM simulations produce the probabilities of the system having each particular density. To test the set up of the method, a first set of simulations was carried out on free hydrogen, about which it is well known the phase diagram as well as the temperature range of the transition. From both experimental and theoretical literature we know the temperature at which the system should present two different phases. Thirteen independent simulations were carried out between $T = 23.94K$ and $T = 44.46K$.

Since our simulations have been done at high chemical potential (needed for good sampling) we re-weight the distribution to the coexisting one, that is, to the potential where both phases are equally probable. According to the simulated temperature, the two peaks can be more or less distant, in terms of density (or particle number), or also resemble a broad beak which cover a large variety of densities. The latter case happens evidently above critical temperature, so that lots of densities are possible (the

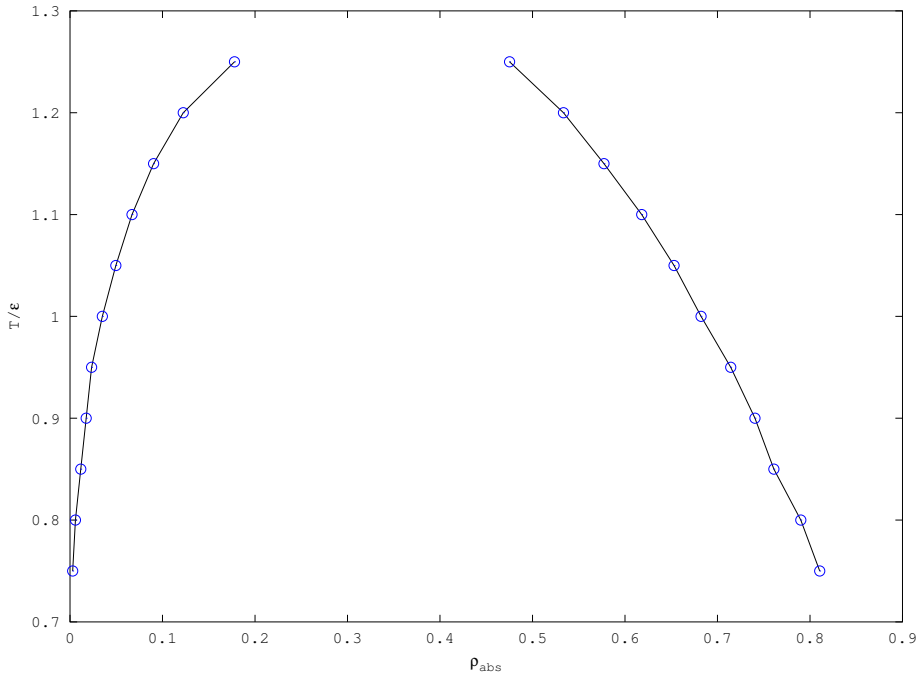

Figure 5.4: *Phase diagram of free hydrogen, 1-centre model. Temperature is in ε and density in σ^{-3}.*

exact value will depend on the chosen or re-weighted chemical potential): the more the system goes towards lower temperatures, the more the peaks start to split and separate.

The obtained joint distribution, presented in figure 5.3, shows the existence of some *improbable* densities, which is consistent with a phase transition occurring at these conditions. Each two peak section of the graph, represent a double point of the hydrogen phase diagram, where at a single temperature correspond two different densities. From the maxima of each distribution is therefore possible to plot the diagram, as presented in figure 5.4. Results appear in perfect agreement with those reported by Errington[27].

Another way to visualize TMMC results of a single temperature simulation, is to extrapolate the peak (*i.e.* probability vs. density graph) at different chemical potentials, obtained by re-weighting with the equation 2.63. The position of the peak means the most probable density corresponding to that conditions of pressure (strictly related to the chemical potential) and temperature. In this way it is possible to show the evolution of the system with pressure: a continuous displacement of the peak imply just the compression of the aggregate (*i.e.* slight increase in density); nevertheless in

presence of a phase transition, a two peak plot is expected so that the slow displacement of the peak suffer an abrupt shift.

Since the data analyzed in figure 5.2 show a coexistence of different conformations at $77K$, we run a series of simulations at that temperature to investigate such phenomenon. A first simulation has been carried out at very high chemical potential, in order to achieve the widest possible scan in terms of particle number (see section 5.1). The temperature is set to $77K$ and simulation box consists of a 30x30x212.7Å cell containing a single $(26, 0)$ CNT perpendicular to the XY plane. The nanotube comprises 5200 atoms but is made infinitely long by the application of periodic boundaries: the cell dimension along axis Z exactly matches the length of the 50 CNT sub-units. As stated in section 5.1, the CNT is actually simulated as an external force field. The density probability $\Pi_{\mu_0}(N)$ is then reweighted for a broad range of chemical potentials far below the superimposed μ_0 using equation (2.63).

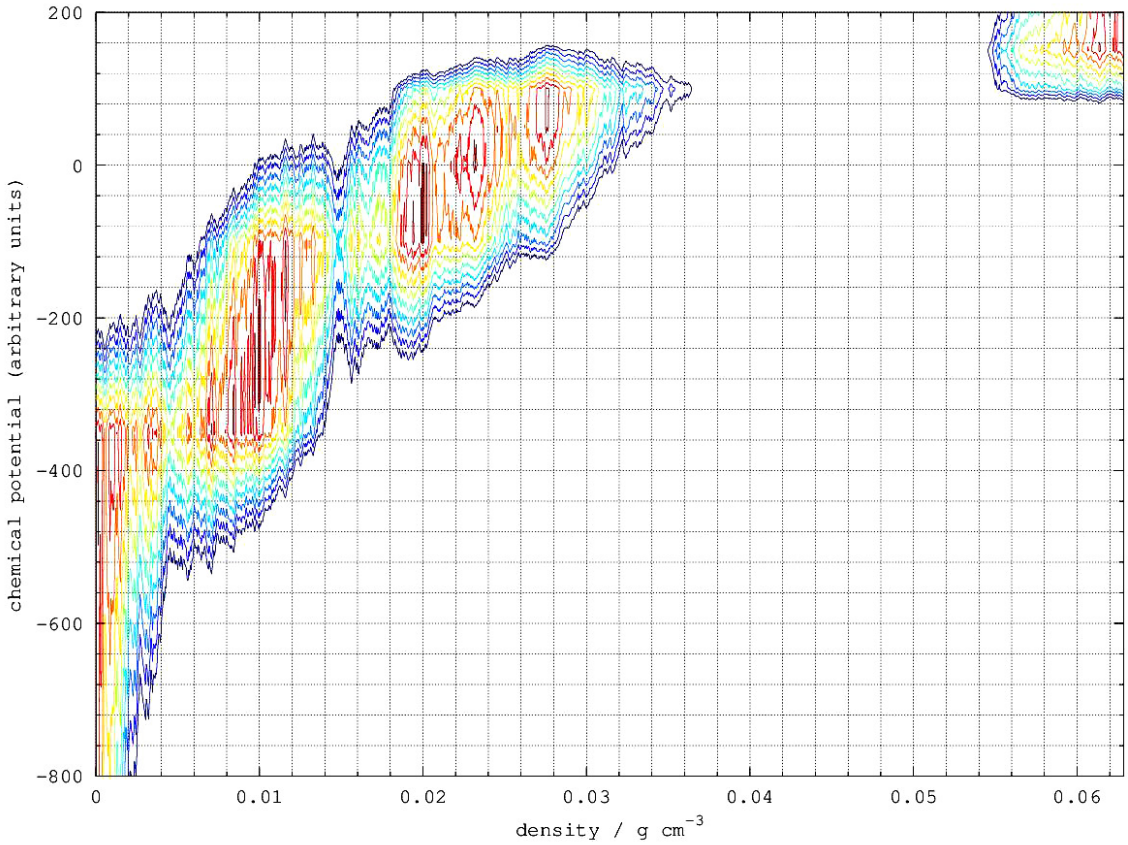

Figure 5.5: *Contour plot of* $\ln[\Pi(\mu, \rho)]$ *Probability of measuring density* ρ *at chemical potential* μ *inside a (26,0) CNT at* $77K$*. Red lines represent highest probability while blue are the lowest.*

The result is shown in figure 5.5, as a 3D contour graph where the red lines represent the highest values of the probability (in logarithmic scale) and the blue the lowest ones. In these conditions, the error associated to the measurement of chemical potential is too high, so the estimation of μ_0 is meaningless. We, thus, present the chemical potential data in arbitrary units.

What emerges from these results is, however, the presence of four well-defined high-probability areas linked by three saddle points. In fact, for each two adjacent zones there is a potential range where the probability distribution is bimodal, thus leading to four possible phases coupled by three transitions. It is known that hysteresis loops in TMMC models are considered as phase transitions [95], so one of the three could be of this type. Therefore, the highest and largest density transition should be the vapour-liquid one, at least considering the densities involved.

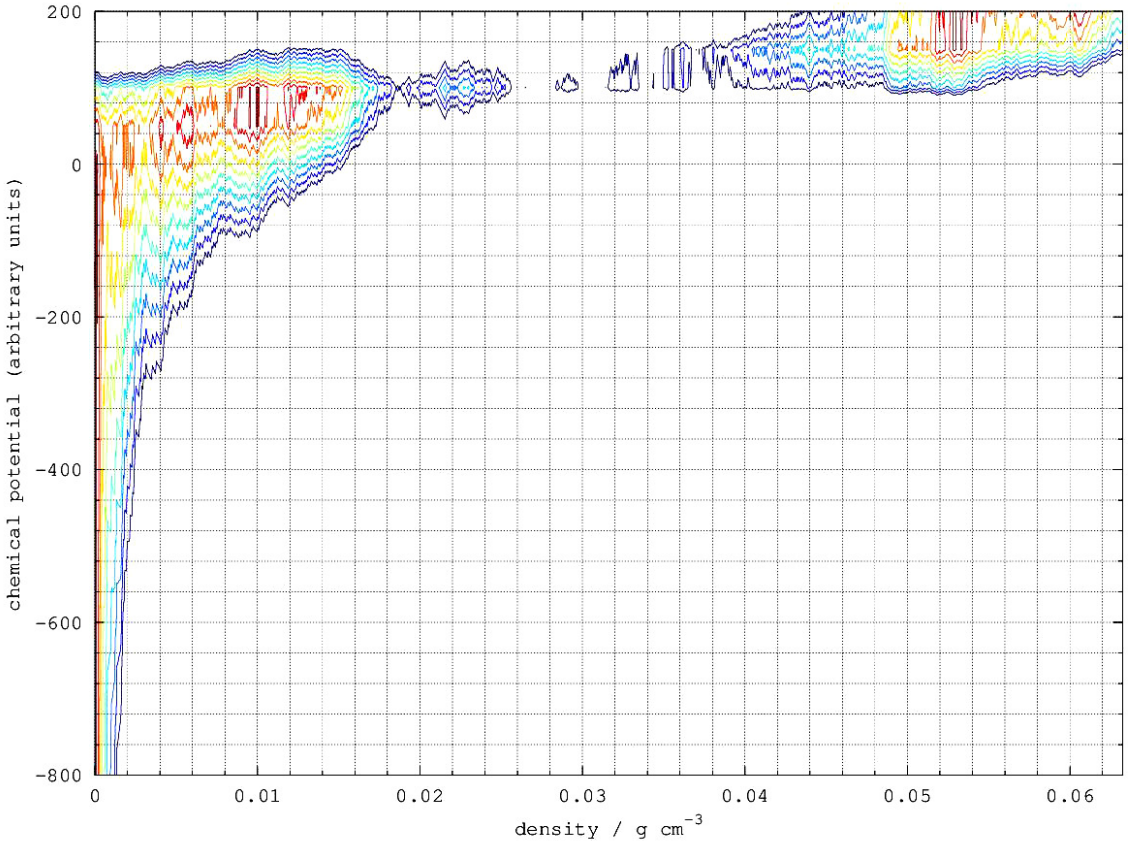

Figure 5.6: *Contour plot of* $\ln[\Pi(\mu,\rho)]$ *Probability of measuring density* ρ *at chemical potential* μ *for free hydrogen at* $77K$*. Red lines represent highest probability while blue are the lowest.*

Figure 5.6 represents an extrapolation of a free hydrogen simulation, for the sake of

comparison, using the same procedure and size as for the CNT system. It shows just one large density gap, whereas the lower density region does not show any significant high-probability zone, as it was observed in the previous case. From these results, we can conclude that, somehow, the CNT is capable of storing hydrogen at higher densities that are not available in free samples.

Moreover the observation of a vapour-liquid transition, in the free hydrogen simulation was certainly unexpected. In fact $77K$ is well above the hydrogen critical temperature. At this point, we should recall that the interpretation of the temperature effect in this context is strictly related to the interaction potential used, in particular the well depth ε of the LJ parameters. Therefore the critical temperature should also be affected. However, the reference TMMC simulation on below-critic temperatures (figure 5.3) is consistent with a vapor-liquid phase transition happening below $45K$. Moreover, the higher densities are also mismatching: $\sim 0.06 g/cm^3$ and $\sim 0.1 g/cm^3$.

A deeper analysis of the histograms of figure 5.5 and 5.6, leads also to some doubt about the efficiency of the sampling. It seems in fact that, although the two peaks are clearly visible in the contour plot (figure 5.6), there is not a value of the chemical potential (*i.e.* an horizontal section of such plot) where the peaks are clearly visible at the same time. What is seen is just a broad distribution with rather low peaks. For this reason, we investigate specifically the TMMC method and how to improve the sampling in high density conditions.

Chapter 6

TMMC improvement

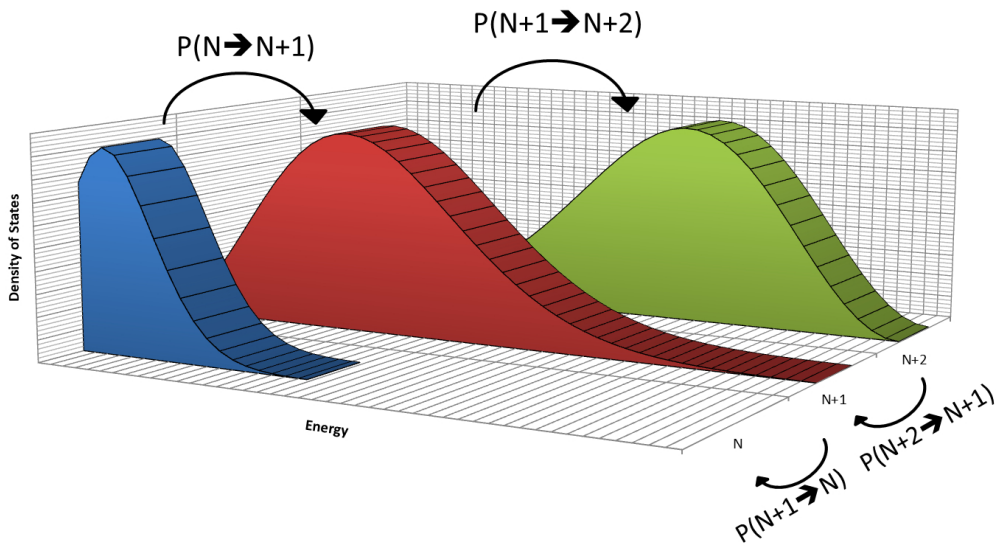

TM algorithm is found to behave quite well for LJ fluids. However, in presence of strong force-fields, which significantly spread the DOS, standard TM protocol seems not able to produce a flat histogram as the algorithm suggests. Although TM is not a flat histogram technique (*i.e.* does not strictly requires the histogram to be flat), strongly confined simulations produces weirdly peaked visited states distributions which raises serious doubt about complete and efficient sampling of all possible states. Increasing simulation steps doesn't seem to bring any benefit. In this chapter we present a new algorithm to improve the method in such cases. Recent studies also aimed to extend the efficiency of such method using multi-canonical approach[115, 58]

or other techniques[43].

6.1 Potential developments of the algorithm

Since the probability of each micro-state $a_i \in A$ (being A the macro-state corresponding to all micro-states with $N = N_a$) is

$$\pi_i = \frac{1}{\Xi} \frac{V^{N_a}}{\Lambda^{3N_a} N_a!} \exp\left(-\beta E_i\right) \exp\left(-\beta \mu N_a\right), \tag{6.1}$$

(where Ξ is the GC partition function, V is the volume os the system, Λ the De Broglie thermal wavelength, E_i the energy of the micro-state, β the inverse temperature $(1/T)$ and μ the chemical potential), the macro-state probability should be the sum of all micro-states:

$$\Pi(A) = \frac{1}{\Xi} \frac{V^{N_a}}{\Lambda^{3N_a} N_a!} \exp\left(-\beta \mu N_a\right) \sum_{i \in A} \exp\left(-\beta E_i\right). \tag{6.2}$$

We join all constant terms into K with the exception of the GC partition function $\Xi(\mu, V, T)$; the sum on the right is nothing more than the canonical partition function of the (N_a, V, T) system

$$\Pi(A) = \frac{1}{N_a!} K(\mu, V, T)^{N_a} \ \frac{Q(N_a, V, T)}{\Xi(\mu, V, T)}. \tag{6.3}$$

It should be pointed out that all the states involved in the calculation of Q must be also present in Ξ (*i.e.* they come from the same simulation) because we are trying to evaluate how often the GC simulation passes through a state with $N = N_a$. The purpose of equation (6.3) is to enlighten that calculating probabilities by means of histograms needs complete sampling of each canonical fraction $(Q(N, V, T))$ of the simulation. In practice the TMMC needs to estimate the relative weight of each canonical ensemble, but to do so, it computes an average of the transition probabilities, as their ratio should tend to such value.

In the TMMC scheme, the estimated average transition probability is collected as following:

$$\frac{\langle P(A \to B) \rangle}{\langle P(B \to A) \rangle} = \frac{\sum_{i \in A} \sum_{j \in B} P(a_i | A) P(a_i \to b_j)}{\sum_{n \in B} \sum_{m \in A} P(b_n | B) P(b_n \to a_m)}. \tag{6.4}$$

Therefore we do not need the sampling to be exhaustive. In fact equation (6.4) would become

$$\frac{P(B)}{P(A)} \ \frac{\sum_{i \in A} \sum_{j \in B} P(a_i) P(a_i \to b_j)}{\sum_{n \in B} \sum_{m \in A} P(b_n) P(b_n \to a_m)} \approx \frac{P(B)}{P(A)}, \tag{6.5}$$

so we only need that the second fraction on the left hand side of equation (6.5) tends towards 1.

The method basically involves two kinds of probabilities: the one regarding the particular micro-state with respect to the corresponding macro-state, $P(a_i|A)$ and the probability $P(a_i \rightarrow b_j)$ which is the accepting probability of a transition from a particular state $a_i \in A$ to a particular state $b_j \in B$. The first one is not actually collected, but it is the micro-states emergence frequency. It's worth to notice that, since $P(a_i|A)$ type probabilities are determined stochastically, they include both effects: state growth (which depends on the DOS) and acceptance rate. On the other hand, the collected values, which are actually acceptance probabilities, are sampled only according to their growth *i.e.* the probability of the state being generated. By combining these values, and the respective reverse-step, the algorithm extrapolates the relative probabilities of the system to be in one macro-state or in the other (see equation 6.5). The key point is, of course, the estimation of $P(a_i|A)$ and $P(b_j|B)$, which are made on the basis of statistical distribution obtained through Metropolis scheme[69]. This means that one or more steps, between two consecutive TMMC trials, have the purpose of moving to another micro-state, according to statistical distribution. All such steps, although essencial for the success of the method, do not store any data for the estimation of the above probabilities.

At high density the system tends to be homogeneous and does not present cavities or empty space where a new molecule could be easly hosted. Therefore, in this conditions, since transitions are attempted while keeping fixed all particle coordinates but one (the particle being either created or deleted), unlikely states are sampled more frequently than they should be. When this happens, lots of steps are then needed to recover the right estimation, because not only it is necessary to reach a significant state (displacement trials), but we also need to sample it many times to compensate (TMMC trials).

TMMC trials essentially scan the target distribution, while the canonical displacements make the starting points distribute properly. Hence the ratio between TMMC and canonical trial frequencies can show how wider we scan the target distribution than the base one. It would be therefore reasonable to keep this ratio close to 1, nevertheless, as the system needs to re-arrange after each accepted transition, more steps are needed between one transition and another. On the other hand, the target distribution could also be scanned using Configurationa Bias (CB) and gathering more samples with each trial. A reasonable conclusion would be setting up lots of re-arrangement steps between TMMC transitions and lots of CB samples. The main drawback of this approach is

that having multiple CB samples, in terms of computational time, is not much faster than increasing the number of steps, so the overall efficiency lowers anyway.

6.2 Testing the method

An empirical test that could enlighten the mechanism of how the GCMC simulation reaches the equilibrium density (or particle number) is to follow and compare the filling of the box and the average energy contribution of each molecule. In figure 6.1 it is represented an illustrative example: on the left is shown the negative energy contribution (the reference $E = 0$ is the empty box) and on the right the filling percentage.

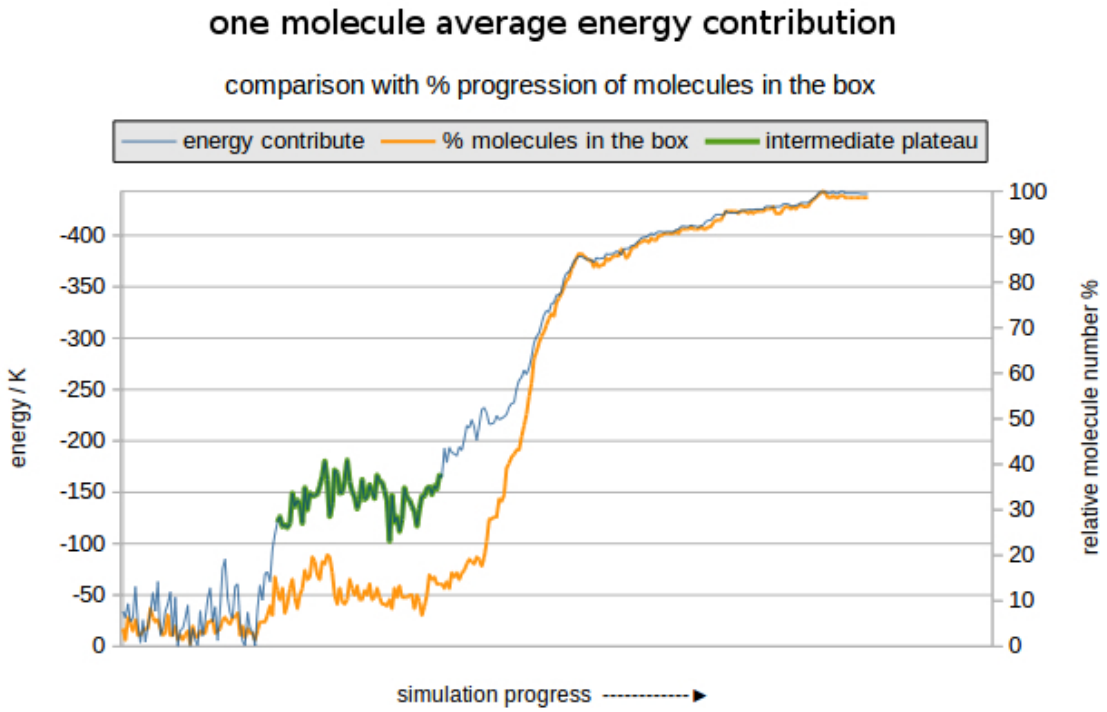

Figure 6.1: *Evolution of energy and particle number during a GCMC H_2 box filling simulation.*

If the insertion happened in a perfectly or ideally homogeneous way, energy should follow exactly the trend of the increasing particle number. On the contrary, after a first period, where the energy contribution fluctuates around small values, it abruptly rises to an intermediate plateau. In other words, at a certain point, the particles already

present encountered a favorable conformation, which therefore lowers the total energy, and only after that the particle number starts to rise again, this time with much less fluctuation. This data clearly shows the importance of rearrangement during the filling process, *i.e.* the $N \to N+1$ trials.

In order to gain a deeper knowledge of such behavior we investigated transitions between systems $N = 0$ and $N = 1$ whose DOS can be calculated analytically. We started by simply splitting the DOS into two equal peaks. This means dividing the simulation box into two equally-sized zones with different uniform potentials. Since any point of the box is equally probable, the height of the peak is proportional to the volume of the corresponding zone.

One can imagine to execute a series of single-N TMMC simulations, in which the system simply tries to increase or decrease the number of particles present but the trial is never accepted while the probability is sampled. Thus the bias would not be explicitly involved; the system however would be forced to a flat histogram, as long as all simulations run for the same number of steps. In this simple case ($0 \to 1$), of course, the calculation can be performed either analytically, or with stochastic simulations.

As an example of interaction potential, we divide the space into seven zones (instead of the two mentioned above) through a square well potential which resembles a LJ-pore. The entire potential is modulated using the well depth of the lowest energy zone, which occupies almost $\sim$ 15% of the space, another zone is repulsive ($\sim 5\times$ - $20\times$ well depth) and constitutes the $\sim$ 25% of the space; then two strong attractive zones ($\sim$ 30% of the space) respectively with 1/2 and 3/4 of the well depth and finally a baseline with about $\sim$ 5 - 10% of the lowest energy.

It is clear that in this case all probabilities of equations (6.4) and (6.5) are known or easy to calculate, but in order to see the weight of the rearrangement in this process, we observe the effect of $P(b_n)$ not being properly sampled. Two cases are considered in practice: a real one in which $P(b_n)$ is exactly calculated and another one where all $P(b_n)$ are considered equal: this would be the case with no rearrangement at all. The probability ratio $P(1)/P(0)$ is plotted as a function of the well depth parameter (divided by the temperature in order to present a general case), results of the calculations are shown in figure (6.2). What can be seen is how important the rearrangement is as much as the potential becomes strong.

Such conclusion can be extended, with some caution, to higher order insertions (*i.e.* $N \to N+1$) as one considers the N existing molecules as a fixed forcefield.

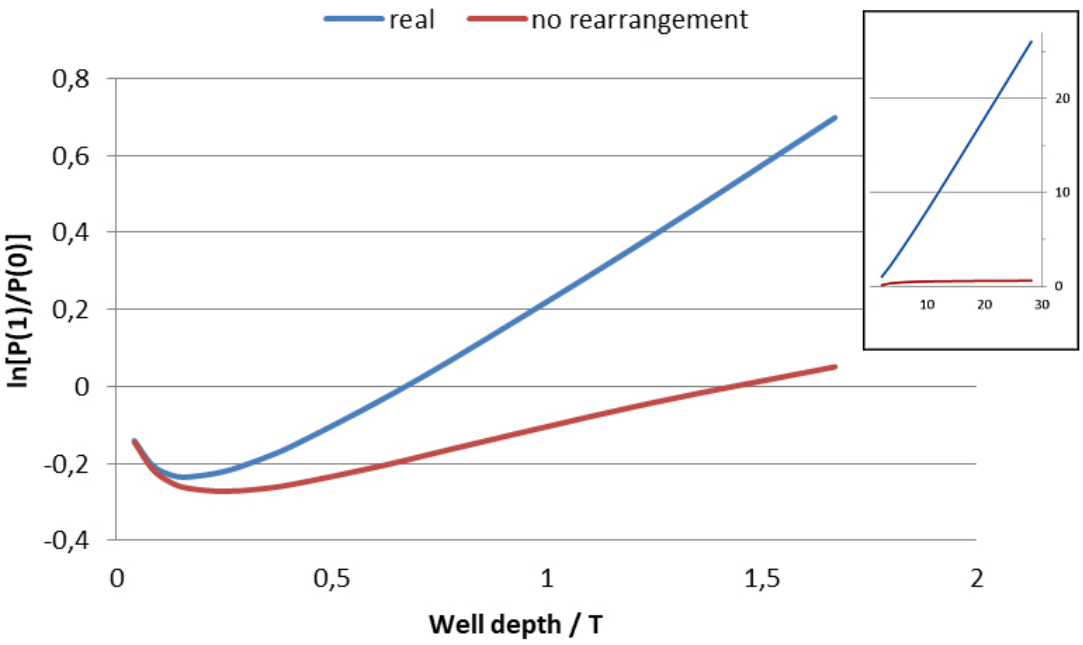

Figure 6.2: *Splitting between estimations of the relative probability, respectively with and without conformational rearrangement.*

6.3 Proposal of an improved algorithm

With the purpose of increasing the TMMC efficiency, we propose a new algorithm, which maintains the basics of the standard one, but includes some new features which eventually lower the necessity of rearrangement and consequently, improves the estimation of the insertion and deletion probabilities. A flowchart of the standard algorithm is presented in figure 6.3.

When estimating, with MC methods, an integral which is a combination of two distributions $u(X)$ and $g(X)$

$$\int u(X)g(X)dX,$$

if one of them is known, it is common to generate samples according to that one, because in most of the cases this means a sampling which is more similar to the integrated function and therefore the convergence is higher (see section 2.3.2). This is what happens in the TMMC algorithm: each transition probability (*i.e.* probability of increasing or decreasing the particle number by one unit) is the integral of the two involved distributions. The algorithm therefore samples according to one of them and calculates the relative value of the other. However, if the distributions are too different

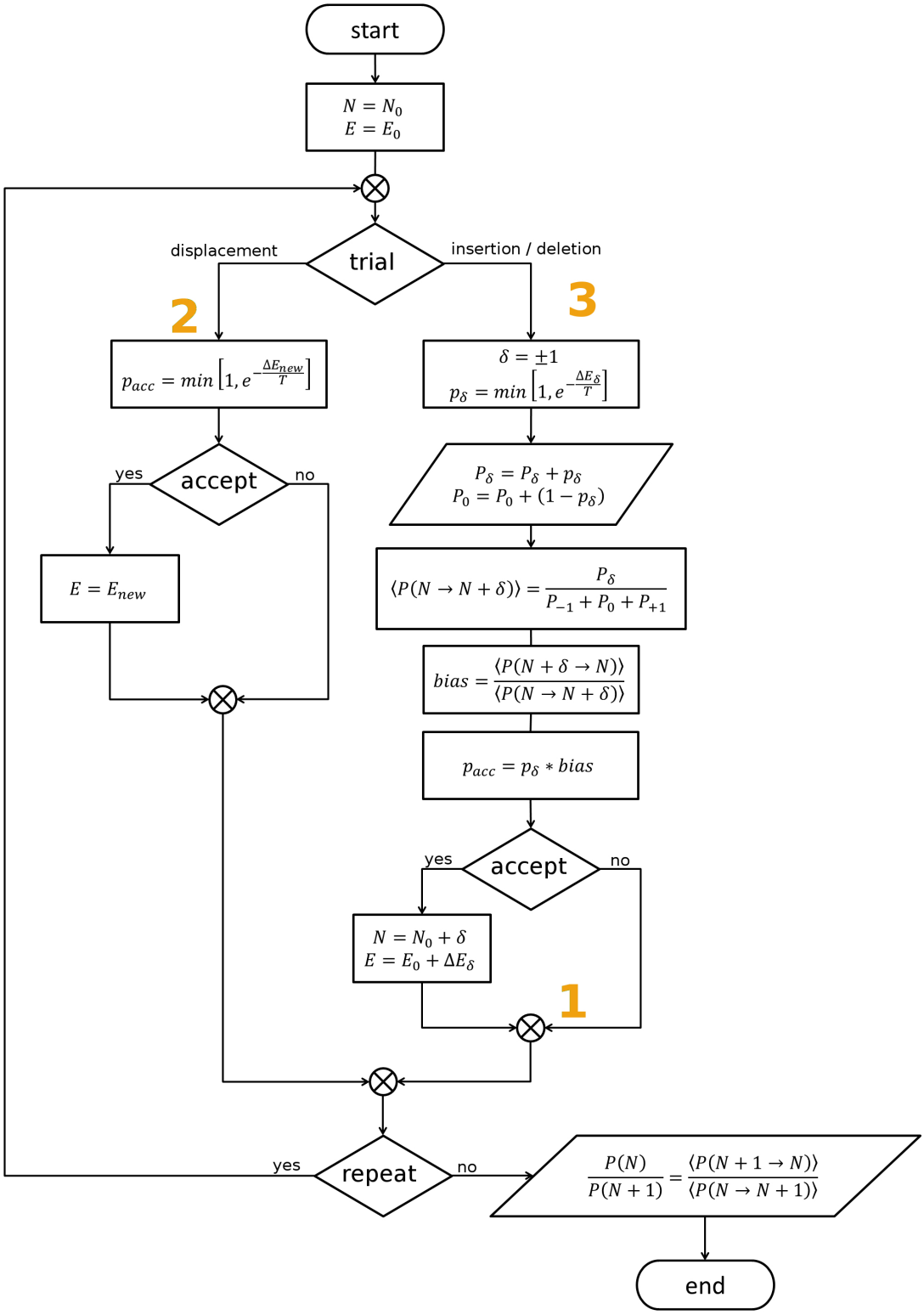

Figure 6.3: *Schematic representation of the TMMC algorithm, according to the implementation in* MCCCS towhee *software[66]. Orange markers are related to the implementation of the new features (see section 6.3.1).*

so that neither one is a good sampling function for the other, the convergence shall be poor. Besides, since we are dealing with lots of degrees of freedom ($X = \{x_i\},\ i = 1, 2, \ldots$), a plain sampling is out of the question.

The general idea is that we can bias the sampling of, for instance $u(X)$, towards the more significant states of $g(X)$. In this way the simulation is constantly between the two distributions, in the zone that should be the most crucial. Hopefully this approach would enhance the coverage of the integral under investigation.

Within the TMMC scheme, the two distributions involved are the ones relative to the systems having respectively N and $N + 1$ particles(or N and $N - 1$ in the reverse approach). In this context, one way to obtain information regarding the adjacent distribution is based on the fact that the two have all the independent variables (*i.e.* the ones needed to define a state) equal with the exception of one set of coordinates: the one of the particle being created or deleted. Hence, continuously measuring data about such particle, allows to have constantly information about the two distributions at once.

A completely new feature is capable of creating a dummy particle and gather information about the interaction energy of that specific particle with the reset of the system. The dummy has identity and coordinates like every other particle, but also a positive - negative switch. This is because the dummy particle can be used to bias the system towards $N + 1$ or $N - 1$. In the fist case it occupies a random non-overlapping place in the system (see figure 6.4) so that, at any time during the displacement trial, the algorithm has information about the insertion probability. The other case connects the dummy to an existing particle recording its interaction energy with opposite sign (negative switch).

With such information, besides knowing the energy difference between the old and the new state (as in the standard Metropolis algorithm), it is also possible to calculate the energy difference that the system would have if it had one more particle or one less, according to the dummy being in positive or negative mode. In this way, it is possible to bias the system with N particles towards states which more likely would accept an insertion trial. In practice, the bias tends to create a reasonable vacancy in the system in order to promote the insertion. The biasing factor is therefore applied and stored, so that we always know how unlikely is the state we moved.

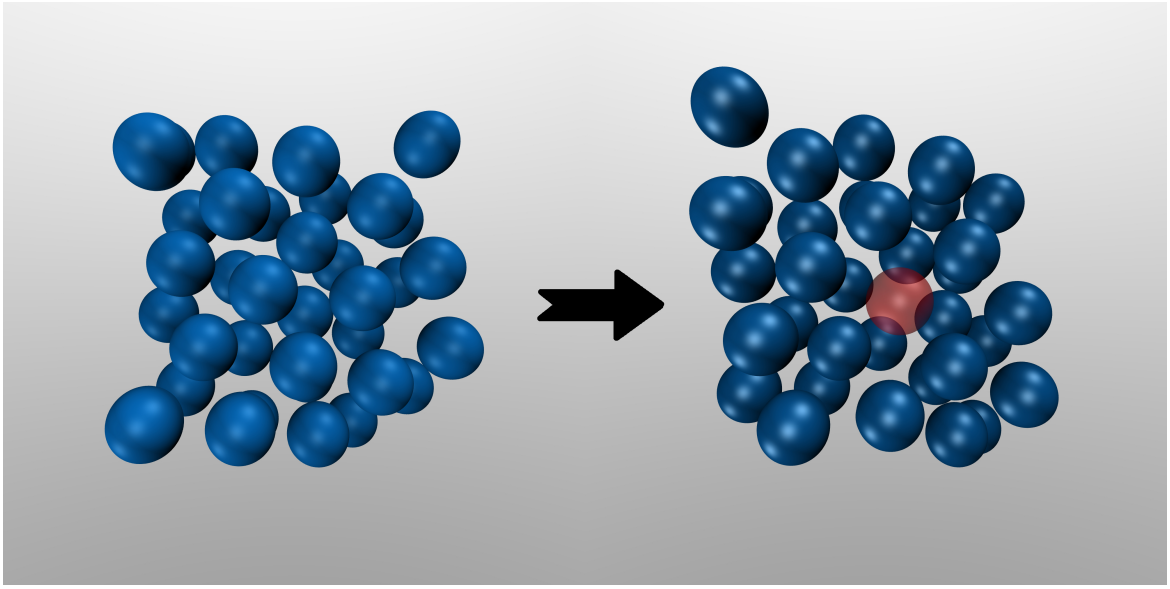

Figure 6.4: *The creation of a* positive *dummy makes the system behave as it had* $N+1$ *particles.*

6.3.1 Algorithm description

The new procedure adds some tasks to the already presented algorithm, which can be activated on purpose for TMMC simulations which involve high density states. Referring to the standard algorithm presented in figure 6.3, we shall call the two main cycles *displacement trial* and *insertion trial* (regardless to the fact that is actually an insertion or a deletion).

Table 6.1: *Variables fixed at dummy creation.*

name	description
index	the particle which the dummy is associated to
coordinates	the position occupied by the dummy
switch $+/-$	inserting or deleting

Variables that have been added to the algorithm are explained in table 6.1 and 6.2.

Before looking to detail of the mechanism, it is useful to enumerate some basic principles of the *dummy* feature. The creation of a dummy is related to a failed insertion trial, so the switch will be positive if it was actually an insertion or negative if it was a deletion attempt. Accepted insertion trials can be obviously considered as *dummies* which are accomplished in the first step (*i.e.* without the need to bias). Since its creation is indiscriminate, to ensure that the biasing still follows the energy

distribution, the *dummy* needs to be reversible, *i.e.* after a certain number of steps in which it tried to accomplish the insertion, the *dummy* has a probability to disappear. Finally, even if not a common case, it is possible that the new biased state has lower energy than the previous, even without bias. It is clear that, when this happens, the reference of the bias is reset and the algorithm continues as that was the first biased step.

In figure 6.3 are marked some numbers that we will refer as checkpoints, in order to make the following explanation more comprehensible.

Table 6.2: *Variables tracked during dummy existence.*

name	description
dummy energy	gives constant track of the transition probability
bias factor	how much the actual state is less probable than the best found
P move	sum of the probabilities of moving
P zero	sum of the probabilities of staying

From the point of view of a single N ensemble (*i.e.* considering only the trial performed when the system has N particles), the standard algorithm run this way: by means of random displacement trials, the system explores the possible micro-states (which follow the Boltzmann distribution) and occasionally, when an insertion trial happens, it gathers the acceptance probability in order to estimate its average value. According to a user defined frequency, such probabilities update the bias factor (whose purpose is to keep the histogram flat); in the end all probabilities are calculated.

As reported before, the *dummy* is created after a failed creation or deletion attempt (figure 6.3, checkpoint 1). When it happens, some of the features described above are suspended or modified until the *dummy* is either deleted or promoted (*i.e.* in its place a particle is successfully inserted). The probability data is stored apart and updated each step regardless its displacement or insertion trial. A bias factor B_f is stored for taking into account of how much the actual state is less probable than the best one found since the activation of the *dummy* . When the *dummy* ends the probability data that was kept apart is weighted by such factor and finally gather the rest of the data.

In the next step, assuming the chosen path is a displacement trial (the other case will be referred to afterwards), the attempt proceeds as usually and the algorithm calculates the energy difference. At the same time the *dummy* calculates also ΔE_d, namely the energy change among its interactions, used to keep track of the total

dummy energy. At this point (figure 6.3, checkpoint 2) the acceptance probability is calculated by summing all the energetic contributions

$$P_{acc} = \min\left[1, \exp\left(-\frac{\Delta E_{new} + \Delta E_d}{T}\right)\right]$$

where ΔE_{new} is the energy change of the displacement. In this way the system is analogous to one with $N+1$ particles (or $N-1$ if the *dummy* switch is negative). From the total dummy energy, it is possible to calculate transitions probabilities p_i and $(1-p_i)$ at each step; they are stored apart and only update the overall value at the end of the *dummy* existence.

$$P_{move} = \sum_{dummy} B_f(i)\ p_i; \qquad P_{zero} = \sum_{dummy} B_f(i)\ (1-p_i)$$

The bias factor B_f keeps summing the unbiased energetic terms each time the displacement is accepted

$$B_f = \exp\left(-\frac{E - E_{min}}{T}\right).$$

Since its reference is the most probable state E_{min} encountered during the *dummy* existence, its value is always ≤ 1; in fact, the opposite would mean being in a state more probable than all the previous visited: in this unlikely event its value is of course reset to 1 and the probabilities P_{move} and P_{zero} are easily corrected according to equation (6.6)

$$P = P \times \exp\left(-\frac{\Delta E_{min}}{T}\right) \tag{6.6}$$

where ΔE_{min} is the energy difference between the old minimum and the new one found.

In summary, the displacement trial plays two important roles: from one side it bias the system towards more favorable states for the transition to happen, but also keeps gathering information about the transition probability and the integral we want to estimate. So the efficiency of displacement steps is greatly increased.

In the event of a GC insertion / deletion trial (regardless of which one would be), a promotion attempt is performed instead (figure 6.3, checkpoint 3). A promotion is just like an insertion trial but the molecule which is going to enter is not chosen at random but is the one associated to the *dummy* (it works exactly the same with deletion trial and negative *dummy*). It can be accepted or not according to the standard probability, which can be now calculated easily from the stored value of the dummy energy E_d

$$P_\delta = \min\left[1, \exp\left(-\frac{E_d}{T}\right)\right].$$

If the trial is accepted the TMMC general averages P_δ and P_0 are updated with the data kept apart

$$P_\delta = P_\delta + P_{move}; \qquad P_0 = P_0 + P_{zero}$$

and the whole process then continues with a system of $N+1$ particles and no dummy. If the promotion is not accepted, the bias is switched off but, since the system still has N particles, the *dummy* can continue to gather information and average the data with the ones sampled with the bias.

However, to avoid oversampling under the *dummy* bias, we implement a criterion rather than a fixed probability to chose the path of the promotion or not. It consists on a swapping attempt between the dummy and a random chosen particle of the same type, guided by Metropolis criterion: if it succeeds the algorithm will proceed with the promotion. A small difference exists here with the negative *dummy* : in that case the energy is compared to a random insertion.

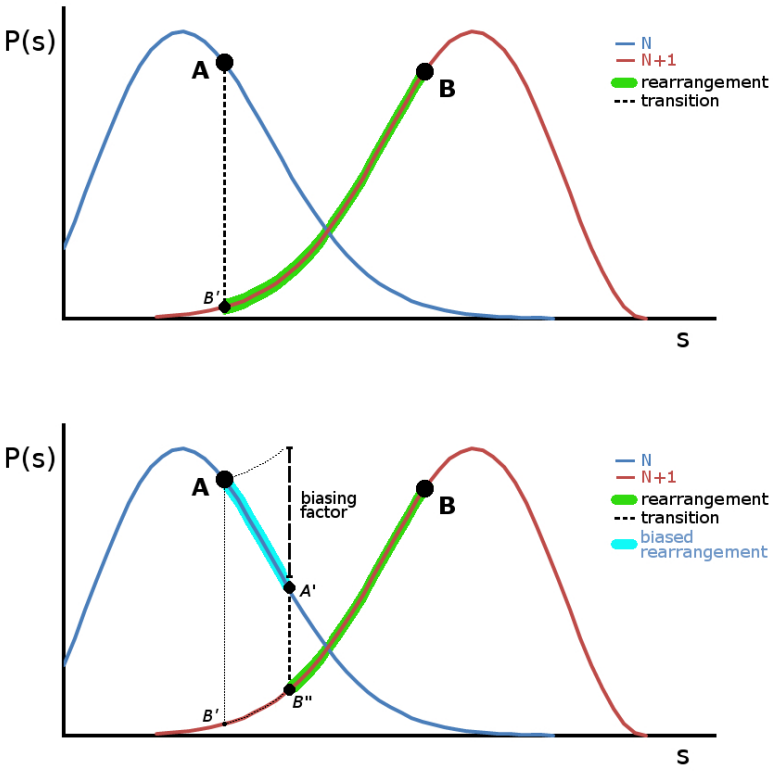

Figure 6.5: *Alternative route of the TMMC modified algorithm.*

As it can be seen in figure 6.5, the standard algorithm goes through a very improbable transition, from A to B', whereas, with the same amount of rearrangements, the modified algorithm encounters a much more probable transition, between A' and B'.

Besides, the presence of the dummy allows to sample the transition probability during the biased displacement trials as well, so that all area beneath the curve, between A and B', can be sampled at once.

Chapter 7

Final Remarks

In this work we managed to apply some of the most advanced MC techniques to nanotube systems. The analysis of the shapes of the potential energy surfaces has been enlightening about the characteristics of the different environments of real samples. Different sized pores, as well as topological defects or the various surfaces of the CNT bundles, they all contribute in a different way to the overall behaviour. Besides, we also find significant discrepancies in the parametrization of the interaction potential (the well depth in particular) in nanotube systems, according to the method applied, respectively mixing rules, fitting experiments (*e.g.* scattering) or *ab initio* calculations. We also show the range of such differences in terms of both PES and amount of adsorbed hydrogen. About hard radius indeed exists more consistency but we enlighten how this parameter as well has important effect on the simulated uptake capability of an inner CNT pore. All these concepts provide useful hints for future modelling of nanotube systems.

Diffusion studies provided precise mobility results, which permitted to correlate the effect with the geometric characteristics of the system. The potential was deliberately chosen weaker than usual, with the purpose of all pores exert the same potential and thus diffusion being affected only by topology. Despite of this, the code produced is already prepared for implementing new force-fields and improved parameters. Future works will focus on the development of an algorithm to study transport diffusion and in the improvement of the SWNT model, which can be achieved by doing an atomic model of the nanotube and also by including specific characteristics of these kind of materials like tortuosity and curvature.

It was also investigated how the geometry of the pores and their shape could affect or

promote phase transition within the hydrogen molecules adsorbed. Results indicate the presence of ordered conformation in some of the inner layers of CNTs, with consequent increase of storage capacity. During such investigation, we found out some drawbacks of the TMMC algorithm in some cases, in particular when dealing with confined spaces and strong potentials. This led to the construction and implementation of a new algorithm with the purpose of enhancing convergence and accuracy of the method.

All the code written was prepared for being interconnected and future works will aim to simulate all this effect simultaneously.

Bibliography

[1] R. S. Aga, C. L. Fu, M. Krcmar, and J. R. Morris. Theoretical investigation of the effect of graphite interlayer spacing on hydrogen absorption. *Physical Review B*, 76(16), 2007.

[2] G. S. Armatas. Determination of the effects of the pore size distribution and pore connectivity distribution on the pore tortuosity and diffusive transport in model porous networks. *Chemical Engineering Science*, 61(14):4662–4675, 2006.

[3] R. Bacsa, C. Laurent, R. Morishima, H. Suzuki, and M. Le Lay. Hydrogen storage in high surface area carbon nanotubes produced by catalytic chemical vapor deposition. *Journal of Physical Chemistry B*, 108(34):12718–12723, 2004.

[4] K. M. Bal and E. C. Neyts. On the time scale associated with Monte Carlo simulations. *Journal of Chemical Physics*, 141(20), 2014.

[5] C. C. Battaile. The kinetic monte carlo method: Foundation, implementation, and application. *Computer Methods in Applied Mechanics and Engineering*, 197(41-42):3386–3398, 2008.

[6] B. A. Berg and T. Neuhaus. Multicanonical ensemble: A new approach to simulate first-order phase transitions. *Physical Review Letters*, 68(1):9–12, 1992.

[7] S. Brunauer, P. H. Emmett, and E. Teller. Adsorption of gases in multimolecular layers. *Journal of the American Chemical Society*, 60(2):309–319, 1938.

[8] V. Buch. Path-integral simulation of mixed *para*-D_2 and *ortho*-D_2 cluster - the orientational effects. *Journal of Chemical Physics*, 100(10):7610–7629, 1994.

[9] D. Cao and J. Wu. Self-diffusion of methane in single-walled carbon nanotubes at sub and supercritical conditions. *Langmuir*, 20(9):3759–3765, 2004.

[10] C. Carbonell-Coronado and M. C. Gordillo. Phase diagram of D_2 adsorbed on graphene and graphite. *Physical Review B*, 85(15):6, 2012.

[11] S. R. Challa, D. S. Sholl, and J. K. Johnson. Adsorption and separation of hydrogen isotopes in carbon nanotubes: Multicomponent grand canonical Monte Carlo simulations. *The Journal of Chemical Physics*, 116(2):814, 2002.

[12] A. Chambers, C. Park, R. T. K. Baker, and N. M. Rodriguez. Hydrogen storage in graphite nanofibers. *Journal of Physical Chemistry B*, 102(22):4253–4256, 1998.

[13] B. Chen and J. I. Siepmann. A novel monte carlo algorithm for simulating strongly associating fluids: Applications to water, hydrogen fluoride, and acetic acid. *Journal of Physical Chemistry B*, 104(36):8725–8734, 2000.

[14] B. Chen and J. I. Siepmann. Improving the efficiency of the aggregation-volume-bias monte carlo algorithm. *Journal of Physical Chemistry B*, 105(45):11275–11282, 2001.

[15] H. Chen, J. K. Johnson, and D. S. Sholl. Transport diffusion of gases is rapid in flexible carbon nanotubes. *Journal of Physical Chemistry B*, 110(5):1971–1975, 2006.

[16] H. Cheng, A. C. Cooper, G. P. Pez, M. K. Kostov, P. Piotrowski, and S. J. Stuart. Molecular dynamics simulations on the effects of diameter and chirality on hydrogen adsorption in single walled carbon nanotubes. *Journal of Physical Chemistry B*, 109(9):3780–3786, 2013.

[17] R. F. Cracknell. Molecular simulation of hydrogen adsorption in graphitic nanofibres. *Physical Chemistry Chemical Physics*, 3(11):2091–2097, 2001.

[18] F. J. A. L. Cruz and E. A. Muller. Behavior of ethylene and ethane within single-walled carbon nanotubes, 2: Dynamical properties. *Adsorption*, 15(1):13–22, 2009.

[19] F. Darkrim and D. Levesque. High adsorptive property of opened carbon nanotubes at 77 k. *Journal of Physical Chemistry B*, 104(29):6773–6776, 2000.

[20] F. L. Darkrim, P. Malbrunot, and G. P. Tartaglia. Review of hydrogen storage by adsorption in carbon nanotubes. *International Journal of Hydrogen Energy*, 27(2):193–202, 2002.

[21] M. F. L. De Volder, S. H. Tawfick, R. H. Baughman, and J. Hart. Carbon nanotubes: present and future commercial applications. *Science*, 339(6119):535–539, 2013.

[22] A. C. Dillon, K. M. Jones, T. A. Bekkedahl, C. H. Kiang, D. S. Bethune, and M. J. Heben. Storage of hydrogen in single-walled carbon nanotubes. 386:377–379, 1997.

[23] D. Dubbeldam, S. Calero, T. J. H. Vlugt, R. Krishna, T. L. M. Maesen, E. Beerdsen, and B. Smit. Force field parametrization through fitting on inflection points in isotherms. *Physical Review Letters*, 93(8), 2004.

[24] T. W. Ebbesen. *Carbon Nanotubes: Preparation and Properties*. 1996.

[25] R. Eckhardt. Stan ulam, john von neumann and the monte carlo method. *Los Alamos science*, (15):131–137, 1987.

[26] A. Einstein. Über die von der molekularkinetischen theorie der wärme geforderte bewegung von in ruhenden flüssigkeiten suspendierten teilchen. *Ann. Phys.*, 322(8):549–560, 1905.

[27] J. R. Errington. Direct calculation of liquid-vapor phase equilibria from transition matrix monte carlo simulation. *Journal of Chemical Physics*, 118(22):9915–9925, 2003.

[28] A. Ferre-Vilaplana. Numerical treatment discussion and ab initio computational reinvestigation of physisorption of molecular hydrogen on graphene. *Journal of Chemical Physics*, 122(10):10, 2005.

[29] A. M. Ferrenberg and D. P. Landau. Critical behavior of the three-dimensional ising model: A high-resolution monte carlo study. *Physical Review B*, 44(10):5081–5091, 1991.

[30] A. M. Ferrenberg and R. H. Swendsen. New monte carlo technique for studying phase transitions. *Physical Review Letters*, 61(23):2635–2638, 1988.

[31] A. M. Ferrenberg and R. H. Swendsen. Optimized monte carlo data analysis. *Physical Review Letters*, 63(12):1195–1198, 1989.

[32] R. P. Feynman and A. R. Hibbs. *Quantum Mechanics and Path Integrals*. New York, 1965.

[33] M. Fitzgerald, R. R. Picard, and R. N. Silver. Canonical transition probabilities for adaptive metropolis stimulation. *Europhysics Letters*, 46(3):282–287, 1999.

[34] S. J. V. Frankland and D. W. Brenner. Hydrogen raman shifts in carbon nanotubes from molecular dynamics simulation. *Chemical Physics Letters*, 334(1-3):18–23, 2001.

[35] D. Frenkel, G. Mooij, and B. Smit. Novel scheme to study structural and thermal properties of continuously deformable molecules. *Journal of Physics-Condensed Matter*, 4(12):3053–3076, 1992.

[36] N. A. Frigerio and N. Clark. A random number set for monte carlo computations. *Transactions of the American Nuclear Society*, (22):283–284, 1975.

[37] G. E. Froudakis. Hydrogen storage in nanotubes & nanostructures. *Materials Today*, 14(7-8):324–328, 2011.

[38] G. Garberoglio and R. Vallauri. Space-dependent diffusion of hydrogen in carbon nanotubes. *Journal of Molecular Liquids*, 117(1-3):43–47, 2005.

[39] S. Ghosh and V. Padmanabhan. Adsorption of hydrogen on single-walled carbon nanotubes with defects. *Diamond and Related Materials*, 59:47–53, 2015.

[40] M. L. Greenfield and D. N. Theodorou. Coarse-grained molecular simulation of penetrant diffusion in a glassy polymer using reverse and kinetic Monte Carlo. *Macromolecules*, 34(24):8541–8553, 2001.

[41] N. Grobert. Carbon nanotubes - becoming clean. *Materials Today*, 10(1):28–35, 2007.

[42] R. B. Gupta. *Hydrogen Fuel: Production, Transport, and Storage*. 2008.

[43] R. Haber and K. H. Hoffmann. Extending the parq transition matrix method to grand canonical ensembles. *Physical Review E*, 93(6), 2016.

[44] J. P. Hansen and I. R. McDonald. *Theory of Simple Liquids*. 2006.

[45] J. K. Holt, H. G. Park, Y. M. Wang, M. Stadermann, A. B. Artyukhin, C. P. Grigoropoulos, A. Noy, and O. Bakajin. Fast mass transport through sub-2-nanometer carbon nanotubes. *Science*, 312(5776):1034–1037, 2006.

[46] K. S. Ibrahim. Carbon nanotubes-properties and applications: a review. *Carbon letters*, 14(3):131–144, 2013.

[47] S. Iijima. Helical microtubules of graphitic carbon. *Nature*, 354(6348):56–58, 1991.

[48] G. E. Ioannatos and X. E. Verykios. H_2 storage on single- and multi-walled carbon nanotubes. *International Journal of Hydrogen Energy*, 35(2):622–628, 2010.

[49] A. F. Ismail, P. S. Goh, S. M. Sanip, and M. Aziz. Transport and separation properties of carbon nanotube-mixed matrix membrane. *Separation and Purification Technology*, 70(1):12–26, 2009.

[50] N. Karatepe and N. Yuca. Hydrogen adsorption on carbon nanotubes purified by different methods. *International Journal of Hydrogen Energy*, 36(17):11467–11473, 2011.

[51] A. Konstantakou, T. A. Steriotis, G. K. Papadopoulos, M. Kainourgiakis, E. S. Kikkinides, and A. K. Stubos. Characterization of nanoporous carbons by combining CO_2 and H_2 sorption data with the monte carlo simulations. *Applied Surface Science*, 253(13):5715–5720, 2007.

[52] P. Kowalczyk, H. Tanaka, R. Holyst, K. Kaneko, T. Ohmori, and J. Miyamoto. Storage of hydrogen at 303 k in graphite slit-like pores from grand canonical monte carlo simulation. *Journal of Physical Chemistry B*, 109(36):17174–17183, 2005.

[53] B. Kuchta, L. Firlej, R. Cepel, P. Pfeifer, and C. Wexler. Structural and energetic factors in designing a nanoporous sorbent for hydrogen storage. *Colloids and Surfaces a-Physicochemical and Engineering Aspects*, 357(1-3):61–66, 2010.

[54] B. Kuchta, L. Firlej, P. Pfeifer, and C. Wexler. Numerical estimation of hydrogen storage limits in carbon-based nanospaces. *Carbon*, 48(1):223–231, 2010.

[55] S. Kumar, S. Srivastava, and Y. K. Vijay. Study of gas transport properties of multi-walled carbon nanotubes/polystyrene composite membranes. *International Journal of Hydrogen Energy*, 37(4):3914–3921, 2012.

[56] I. Langmuir. The adsorption of gases on plane surfaces of glass, mica and platinum. *Journal of the American Chemical Society*, 40(9):1361–1403, 1918.

[57] S. M. Lee and Y. H. Lee. Hydrogen storage in single-walled carbon nanotubes. *Applied Physics Letters*, 76(20):2877–2879, 2000.

[58] Y. H. Lee and D. Yevick. Renormalized multicanonical sampling in multiple dimensions. *Physical Review E*, 94(4), 2016.

[59] M. Lerario and A. L. Magalhães. A study of interaction potentials for H_2 adsorption in single walled nano tubes: a possible way to more realistic predictions. *Journal of Molecular Modeling*, 20(6), 2014.

[60] D. Levesque, A. Gicquel, F. L. Darkrim, and S. B. Kayiran. Monte carlo simulations of hydrogen storage in carbon nanotubes. *Journal of Physics-Condensed Matter*, 14(40):9285–9293, 2002.

[61] C. Liu and H. M. Cheng. Carbon nanotubes for clean energy applications. *Journal of Physics D-Applied Physics*, 38(14):R231–R252, 2005.

[62] C. Liu, Y. Y. Fan, M. Liu, H. T. Cong, H. M. Cheng, and M. S. Dresselhaus. Hydrogen storage in single-walled carbon nanotubes at room temperature. *Science*, 286(5442):1127–1129, 1999.

[63] A. P. Lyubartsev, A. A. Martsinovski, S. V. Shevkunov, and P. N. Vorontsov-Velyaminov. New approach to monte carlo calculation of the free energy: Method of expanded ensembles. *The Journal of Chemical Physics*, 96(3):1776–1783, 1992.

[64] Z. Mao and S. B. Sinnot. A computational study of molecular diffusion and dynamic flow through carbon nanotubes. *Journal of Physical Chemistry B*, 104(19):4618–4624, 2000.

[65] G. Marsaglia. Choosing a point from the surface of a sphere. *The Annals of Mathematical Statistics*, 43(2):645–646, 1972.

[66] M. G. Martin. MCCCS Towhee version 7.0.6. http://towhee.sourceforge.net, 2012.

[67] L. Mattera, F. Rosatelli, C. Salvo, F. Tommasini, U. Valbusa, and G. Vidali. Selective adsorption of $^1H_2$ and $^2H_2$ on the (0001) graphite surface. *Surface Science*, 93(2-3):515–525, 1980.

[68] N. Metropolis. The beginning of monte carlo method. *Los Alamos science*, (15):125–130, 1987.

[69] N. Metropolis, A. W. Rosenbluth, M. N. Rosenbluth, A. H. Teller, and E. Teller. Equation of state calculations by fast computing machines. *Journal of Chemical Physics*, 21(6):1087–1092, 1953.

[70] N. Metropolis and S. Ulam. The monte carlo method. *Journal of the American Statistical Association*, 44(247):335–341, 1949. PMID: 18139350.

[71] D. Minami, T. Ohkubo, Y. Kuroda, K. Sakai, H. Sakai, and M. Abe. Structural optimization of arranged carbon nanotubes for hydrogen storage by grand canonical monte carlo simulation. *International Journal of Hydrogen Energy*, 35(22):12398–12404, 2010.

[72] T. Mutat, J. Adler, and M. Sheintuch. Single species transport and self diffusion in wide single-walled carbon nanotubes. *Journal of Chemical Physics*, 136(23), 2012.

[73] D. G. Narehood, J. Pearce, and P. Eklund. Diffusion of H_2 adsorbed on single-walled carbon nanotubes. *Physical Review B*, 67(20):1–5, 2003.

[74] K. C. Ng, W. J. Meath, and A. R. Allnatt. Charge overlap effects and the validity of the multipole results for first-order molecule-molecule interaction energies. formalism and an application to H_2-H_2. *Molecular Physics*, 32(1):177–194, 1976.

[75] T. X. Nguyen, J. S. Bae, Y. Wang, and S. K. Bhatia. On the strength of the hydrogen-carbon interaction as deduced from physisorption. *Langmuir*, 25(8):4314–4319, 2009.

[76] T. X. Nguyen, N. Cohaut, J. S. Bae, and S. K. Bhatia. New method for atomistic modeling of the microstructure of activated carbons using hybrid reverse monte carlo simulation. *Langmuir*, 24(15):7912–7922, 2008.

[77] T. X. Nguyen, H. Jobic, and S. K. Bhatia. Microscopic observation of kinetic molecular sieving of hydrogen isotopes in a nanoporous material. *Physical Review Letters*, 105(8), 2010.

[78] G. E. Norman and V. S. Filinov. Investigations of phase transitions by a monte-carlo method. *High Temperature*, 7(2):216–222, 1969.

[79] A. S. Paluch, V. K. Shen, and J. R. Errington. Comparing the use of gibbs ensemble and grand-canonical transition-matrix monte carlo methods to determine phase equilibria. *Industrial and Engineering Chemistry Research*, 47(13):4533–4541, 2008.

[80] A. Z. Panagiotopoulos. Direct determination of phase coexistence properties of fluids by monte carlo simulation in a new ensemble. *Molecular Physics*, 61(4):813–826, 1987.

[81] A. Z. Panagiotopoulos, N. Quirke, M. Stapleton, and D. J. Tildesley. Phase equilibria by simulation in the gibbs ensemble alternative derivation, generalization and application to mixture and membrane equilibria. *Molecular Physics*, 63(4):527–545, 1988.

[82] E. Paquet and H. L. Viktor. Molecular dynamics, monte carlo simulations, and langevin dynamics: A computational review. *BioMed Research International*, 2015, 2015.

[83] S. Patchkovskii, J. S. Tse, S. N. Yurchenko, L. Zhechkov, T. Heine, and G. Seifert. Graphene nanostructures as tunable storage media for molecular hydrogen. *Proceedings of the National Academy of Sciences of the United States of America*, 102(30):10439–10444, 2005.

[84] J. J. Potoff and A. Z. Panagiotopoulos. Critical point and phase behavior of the pure fluid and a lennard-jones mixture. *Journal of Chemical Physics*, 109(24):10914–10920, 1998.

[85] A. Ramirez. A kinetic monte carlo approach to diffusion in disordered nanoporous carbons. *Chemical Engineering Science*, 66(22):5663–5671, 2011.

[86] A. Ramirez. Anisotropic diffusion of hydrogen in nanoporous carbons. *Journal of Material Science*, 49(20):7087–7089, 2014.

[87] A. K. Rappe, C. J. Casewit, K. S. Colwell, W. A. Goddard, and W. M. Skiff. UFF, a full periodic table force field for molecular mechanics and molecular dynamics simulations. *Journal of the American Chemical Society*, 114(25):10024–10035, 1992.

[88] M. N. Rosenbluth and A. W. Rosenbluth. Monte carlo calculation of the average extension of molecular chains. *Journal of Chemical Physics*, 23(2):356–359, 1955.

[89] G. Rossum. Python reference manual. Technical report, Amsterdam, The Netherlands, The Netherlands, 1995.

[90] T. Roussel, C. Bichara, K. E. Gubbins, and R. J. M. Pellenq. Hydrogen storage enhanced in *Li*-doped carbon replica of zeolites: A possible route to achieve fuel cell demand. *Journal of Chemical Physics*, 130(17), 2009.

[91] M. Rzepka, P. Lamp, and M. A. de la Casa-Lillo. Physisorption of hydrogen on microporous carbon and carbon nanotubes. *Journal of Physical Chemistry B*, 102(52):10894–10898, 1998.

[92] A. Sengupta and J. Adhikari. Fluid phase equilibria of triangle-well fluids confined inside slit pores: A transition matrix monte carlo simulation study. *Journal of Molecular Liquids*, 221:1184–1196, 2016.

[93] P. Serp, M. Corrias, and P. Kalck. Carbon nanotubes and nanofibers in catalysis. *Applied Catalysis A: General*, 253(2):337–358, 2003.

[94] M. Shiraishi, T. Takenobu, H. Kataura, and M. Ata. Hydrogen adsorption and desorption in carbon nanotube systems and its mechanisms. *Applied Physics a-Materials Science & Processing*, 78(7):947–953, 2004.

[95] D. W. Siderius and V. K. Shen. Use of the grand canonical transition-matrix monte carlo method to model gas adsorption in porous materials. *Journal of Physical Chemistry C*, 117(11):5861–5872, 2013.

[96] J. I. Siepmann. A method for the direct calculation of chemical-potentials for dense chain systems. *Molecular Physics*, 70(6):1145–1158, 1990.

[97] J. I. Siepmann and D. Frenkel. Configurational bias monte carlo - a new sampling scheme for flexible chains. *Molecular Physics*, 75(1):59–70, 1992.

[98] I. F. Silvera and V. V. Goldman. The isotropic intermolecular potential for H_2 and D_2 in the solid and gas phases. *Journal of Chemical Physics*, 69(9):4209–4213, 1978.

[99] A. K. Singh, J. Lu, R. S. Aga, and B. I. Yakobson. Hydrogen storage capacity of carbon-foams: Grand canonical monte carlo simulations. *Journal of Physical Chemistry C*, 115(5):2476–2482, 2011.

[100] A. I. Skoulidas, D. M. Ackerman, J. K. Johnson, and D. S. Sholl. Rapid transport of gases in carbon nanotubes. *Physical Review Letters*, 89(18), 2002.

[101] R. Q. Snurr, A. T. Bell, and D. N. Theodorou. Prediction of adsorption of aromatic hydrocarbons in silicalite from grand canonical monte carlo simulations with biased insertions. *Journal of Physical Chemistry*, 97(51):13742–13752, 1993.

[102] G. Stan and M. W. Cole. Hydrogen adsorption in nanotubes. *Journal of Low Temperature Physics*, 110(1-2):539–544, 1998.

[103] W. A. Steele. The physical interaction of gases with crystalline solids. i. gas-solid energies and properties of isolated adsorbed atoms. *Surface Science*, 36(1):317–352, 1973.

[104] W. A. Steele. *The Interaction of Gases with Solid Surfaces*. 1974.

[105] D. Y. Sun, J. W. Liu, X. G. Gong, and Z. F. Liu. Empirical potential for the interaction between molecular hydrogen and graphite. *Physical Review B*, 75(7):7, 2007.

[106] B. P. Tarasov, J. P. Maelen, M. V. Lototsky, V. E. Muradyan, and V. A. Yartys. Hydrogen sorption properties of arc generated single-wall carbon nanotubes. *Journal of Alloys and Compounds*, 356:510–514, 2003.

[107] S. Ulam, R. Richtmeyer, and J. von Neumann. Statistical methods in neutron diffusion: Technical report. *LAMS-551*, (April 9), 1947.

[108] P. W. van der Pas. The discovery of the brownian motion. *Scientiarum Historia*, 13:27–35, 1971.

[109] S. C. Wang, L. Senbetu, and C. W. Woo. Superlattice of parahydrogen physisorbed on graphite surface. *Journal of Low Temperature Physics*, 41(5-6):611–628, 1980.

[110] B. Widom. Some topics in the theory of fluids. *Journal of Chemical Physics*, 39(11):2808, 1963.

[111] K. A. Williams and P. C. Eklund. Monte carlo simulations of H_2 physisorption in finite-diameter carbon nanotube ropes. *Chemical Physics Letters*, 320(3-4):352–358, 2000.

[112] F. T. Willmore, X. Y. Wang, and I. C. Sanchez. Gas diffusion in glasses via a probabilistic molecular dynamics. *Journal of Chemical Physics*, 126(23), 2007.

[113] X. Yang and A. Hassanein. Kinetic monte carlo simulation of hydrogen diffusion on tungsten reconstructed (0 0 1) surface. *Fusion Engineering and Design*, 89(11):2545–2549, 2014.

[114] Y. Ye, C. C. Ahn, C. Witham, B. Fultz, J. Liu, A. G. Rinzler, D. Colbert, K. A. Smith, and R. E. Smalley. Hydrogen adsorption and cohesive energy of single-walled carbon nanotubes. *Applied Physics Letters*, 74(16):2307–2309, 1999.

[115] D. Yevick. Renormalized multicanonical sampling. *International Journal of Modern Physics C*, 27(3), 2016.

[116] L. Zhang, B. Zhao, X. Wang, Y. Liang, H. Qiu, G. Zheng, and J. Yang. Gas transport in vertically-aligned carbon nanotube/parylene composite membranes. *Carbon*, 66:11–17, 2014.